FaX-ToR

Fast X-ray Tomography & Radioscopy Beamline for ALBA

A proposal to the S.A.C.

October 2014

A Fast X-ray Tomography and Radioscopy for Alba

Peregrine falcon is one of the FASTEST animals in the planet with capacity of diving at 300km/h

We have decided to use this animal as a representative icon for the future FAST TOMOGRAPHY beamline

Working team:

Federico Sket
Eusebio Solórzano
Juan Gomez Barreiro
Jose Antonio Yagë-Fabra
Bart Bijnens
Vicente Gomez Ruiz de Argandona
Francisco García Moreno

Alba working team:

Eva pereiro
Salvador Ferrer
Josep Nicolas
Xabier Mikel Turrillas
Jordi Juanhuix
Josep Campmany Guillot
Miguel A. G. Aranda

TABLE OF CONTENTS

1. ABSTRACT 11

2. INTRODUCTION 12

2.1. Importance of X-ray imaging and tomography 12

2.2. Virtues of X-ray tomography 13

2.3. Development of SXCT in the last decades 14

2.3.1. 4D tomography 16

2.3.2. In-situ tomography 17

2.4. Scope of this proposal 18

3. THE SPANISH (AND EUROPEAN) USER COMMUNITY 19

3.1. Current panorama of SXCT in Europe 19

3.2. Potential users in Spain 20

4. RELEVANT SCIENTIFIC CASES 23

4.1. Multidisciplinary Fast tomography and radiography: in-situ studies 23

4.1.1. Bubble nucleation and growth characterized by ultrafast tomography 23

4.1.2. In-situ solidification of Al alloys 26

4.1.3. Understanding explosive volcanoes: risk evaluation through morphometric analysis of bubbles and crystals in lava 30

4.1.4. Food science: tasting the texture 33

4.1.5. Ultra-fast 2D Radioscopy on cell wall ruptures to study metal foam stability mechanisms 35

4.1.6. In-situ tomography of creep process of brass 38

4.1.7. In-situ tomography of damage development of carbon-fiber reinforced composites 40

4.2. Material science 42

4.2.1. Resin microflow by X-ray computed tomography 42

4.2.2. 3D multiphase networks providing high temperature strength to Al-Si piston alloys 44

4.2.3. Sub-micrometer holotomography of multiphase metals 47

4.3. Life sciences and biomedicine 50

4.3.1. High resolution Structural Imaging of static tissue: 51

4.3.2. High throughput Virtual Pathology 52

4.3.3. High speed dynamic imaging of functional organs 53

4.4. Historical building 54

4.4.1. In-situ tomography of the fluid movement inside rocks: application to historical building conservation 54
4.5. Biology 57
4.5.1. Investigating the continuous dental replacement of mammals through a new rodent model 57
4.6. Paleontology (foraminifera tomcat) 60
4.6.1. Morphological characterization of fossils 60
5. BEAMLINE CONCEPT, LAYOUT AND REQUIREMENTS 62
5.1. Technical requirements 62
5.2. Source 63
5.2.1. Source properties 63
5.3. Multilayer and Si(111) monochromators 65
5.4. Beamline layout 68
5.5. Experimental end-station and detection systems 69
5.5.1. Sample positioning system: 69
5.5.2. Imaging systems 72
5.6. Sample environment 75
5.6.1. Tensile, compression, fatigue test rigs 75
5.6.2. High temperature furnace 77
5.6.3. Cryogenic cell 79
5.6.4. High pressure cell 80
5.7. Computation and data storage 80
5.8. Estimated budget 82
5.9. Future development 83
6. REFERENCES 84
ANNEX 1. Letters of support from Spanish companies and relevant institutions 89

TABLE OF FIGURES

Figure 1. Tomographic methods spanning over 9 orders of magnitude [11]. 13

Figure 2. Scientific production considering synchrotron tomography over the last 20 years (a) Number of indexed publications (b) Cites per year, total number of cites and h-index for synchrotron tomography. (c) Scientific production considering synchrotron tomography and diffraction over the last 20 years. The number of papers is normalized to the maximum number of paper per year. (d) Relative number of paper for different specific tomographic techniques (normalized to the maximum number of paper per year). (e) Publication by subject for synchrotron microtomography. Source: Web of Science and Scopus. 15

Figure 3. Map of Europe including the list of European Synchrotrons with available tomographic techniques. 19

Figure 4. Geographic distribution of the supporting cluster in the Iberian territory. 22

Figure 5. Detail of the stirring head over the kapton mould containing the isocyanate and polyol blends before the mixing process. 24

Figure 6. Volume rendering at different instants for the two examined materials (TOP: pure PU; BOTTOM: PU with 3 %wt. nanosilica) at (a) 9.8s, (b) 21.7s, (c) 26.3s and (d) 32.6s). 25

Figure 7. Left: In-situ cell density evolution compared models. Right: In-situ cell diameter compared with the theoretical models. 26

Figure 8. Reconstructed tomographic slices obtained during in situ solidification of AlMg4.7Si8 at the temperatures at which consecutive solidification of the different phases is observed, [38]. 28

Figure 9. a) to d): rendered 3D images of the α-Al dendritic solidification at different temperatures during cooling of an AlMg4.8Si7 alloy obtained in situ by SXCT. e) to h): distribution of the mean and Gauss curvatures of the surface of the α -Al dendritic structure at the different stages of the solidification process. [38] 29

Figure 10: Bubble size, wall thickness and interconnection from basaltic foams [53] 30

Figure 11: Different pyroclastic microtextures from silicic melts. Bubbles appear segmented [56]. 31

Figure 12. (a) 3D design and (b) top photograph of the laser system mounted on TOMCAT beamline at SLS. T range is 400-1700ºC [58,59] 32

Figure 13. a-c 3D rendering of acid melt at different temperatures (bubbles); d) bubble size distributions at different temperatures; e) bubble anisotropy and fraction versus temperature [59]. 33

Figure 14. Evolution bubbles in bread during proofing: (a) 2D images of horizontal sections (diameter 9 mm) extracted from reconstructed volumes (628x628x256 voxels) (b) and (c) Void volume fraction and average cell-wall thickness for three different doughs [68]. 34

Figure 15. (upper left) Synchrotron radiation tomography: phase contrast slices of the fruit cortex of apple (left) and pear (right); cell walls are indicated by arrows. (lower left) Modeled (a) against measured (b) 3-D geometry of apple cortex cells. (Right) The oxygen concentration profile inside cells using finite element simulations. Driven force was partial pressure across the boundaries of the tissue. The partial pressure and concentration inside the tissue was related by the universal ideal gas law [65]. 35

Figure 16. Evolution of time resolution for in-situ synchrotron X-ray radioscopy applied to visualize metal foaming. 36

Figure 17. Series of radiographs of an AlSi10 + 0.5wt.% TiH2 foam at 640°C extracted from an in-situ fast synchrotron X-ray radioscopic analysis. The coalescence of two bubbles measured with 9.5µs frame interval (105kfps) can be observed. Dashed lines indicate the contours of the bubbles and arrows indicate the corresponding ruptured cell wall. 37

Figure 18. Tomographic volumes revealing the cavities at different times during the creep test. (a) initial condition, (b) middle of the test, (c) close to fracture. 38

Figure 19. Shape evolution of the three largest cavities exhibiting coalescence. The different stages correspond to the largest pore before coalescence..... 39

Figure 20. Evolution of the spatial orientation of cavities..... 40

Figure 21. Damage propagation in ±45º plies. Different crack colours indicate their connectivity (adapted from [17]). 42

Figure 22. Experimental set up to study in situ the infiltration process at the P05 beamline of DESY Synchrotron. 43

Figure 23. (a) Cross section of the scanned fiber tow specimen in the vacuum bag. Wet glass fibers are surrounded by the lighter grey color. (a) 3D reconstruction of the infiltrated tow. 44

Figure 24. 3D structures of aluminides and Si after 4h of solution treatment: a) Si in AlSi12, b) Si and aluminides in AlSi12Ni, c) aluminides in AlSi10Cu5Ni1, d) aluminides in AlSi12Cu5Ni2, e) Si in AlSi10Cu5Ni1 and f) Si in AlSi10Cu5Ni2. 46

Figure 25. Proof stress $\sigma_{0.2}$ at 300ºC for the investigated alloys as a function of the solution treatment time. 47

Figure 26. Top: scanning electron micrographs of the investigated materials Bottom: portions of slices of holotomography reconstructions of the investigated materials. From left to right: AlMg7Si4 alloy, Ti1023 alloy and Ti64/TiB/5w. 49

Figure 27. Rendered volumes of the investigated materials: a) interconnected Si-Mg_2Si structure (green) in AlMg7Si4; b) larger α particles remaining from pre-forging (blue) and individual secondary α grains (semi-transparent green) in Ti1023; c) TiB needles (green) and irregularly shaped β grains in Ti64/TiB/5w (other colours). 50

Figure 28. Phase-contrast imaging of whole (rodent) hearts. Beside the anatomical detail at organ level, the detailed fibre structure in which myocytes are organised can easily be assessed. Additionally, vessels can be observed and extracted using computational tools [89]. 51

Figure 29. Image of a preterm rabbit pup thorax, focusing on the air/lung tissue interface [90]. 51

Figure 30. Spatial resolution of histology, X-ray phase tomography, and MRI microscopy demonstrating that resolution decreases from histology via PC-mCT to mMRI [91]. 52

Figure 31. A false positive MRI post mortem, suggesting lung changes while histology was normal.... 52

Figure 32. Breathing activity and the increase in end-expiratory lung gas volumes from birth in a spontaneously breathing newborn rabbit pup. Phase contrast X-ray images were acquired at the times indicated by the arrows demonstrate the increase in lung aeration [94]. 53

Figure 33. a) Uniform distribution of the minerals except in iron oxides layers (at the bottom). b) (1) void spaces; (2) fine-grained carbonates; (3) large-grained carbonates and (4) clays and iron minerals. 54

Figure 34. a) CT images showing the variation in water penetration. b) 3D images of the open porosity. 55

Figure 35. CT images at different times during the absorption test. The positions of nine ROI´s used to quantify the water penetration rate are indicated. 56

Figure 36. Evolution of the mean CT number of the internal ROI´s. 57

Figure 37. a) Foreside of a captive silvery mole-rat, b) 3D reconstruction and c) Virtual cross-section of the upper dentition of an adult silvery mole-rat. 58

Figure 38. a) 3D reconstruction in lateral view of a lower tooth row and b) model of dental replacement of the silvery mole-rat. c) 3D reconstruction in lateral view of a lower tooth row and d) model of dental replacement of the pygmy rock-wallaby (green arrows: molar progression; red arrow: tooth loss). 59

Figure 39. Right chelal fingers of a Pseudogarypus synchrotron [103] fossil trapped in amber 61

Figure 40. Horizontal phase space distribution of the WS400 source 64

Figure 41. Horizontal spatial flux distribution of the source for 4 photon energies, for low energies a parasitic side-lobe appears. 64

Figure 42. Photon source distribution for (vertical and horizontal) for three photon energies. 65

Figure 43. Flux emitted within a horizontal acceptance of 1 mrad, for the proposed source compared to a bending magnet. 65

Figure 44. Bragg angle for a 4 nm multilayer monochromator, and for a Si(111) crystal pair. 66

Figure 45. Vertical size of the illuminated area (Double Multilayer Monochromator = DMLM). 67

Figure 46. Sample illumination area for two different values of the energy. The stripes are caused by the slope error of the multilayer (ML) mirrors. 67

Figure 47. Schematic optical layout of the imaging beamline 68

Figure 48. Layout of the Imaging beamline at the ALBA Experimental Hall. 69

Figure 49. Zoomed photography of a system similar to the one intended to install at Alba (Courtesy of PIMicos Iberia). 71

Figure 50. Schematic description of the two microscopes considered to be mounted at FaX-ToR beamline. 72

Figure 51. Left: 3D rendering of the white-beam microscope mounting a PCO. Dimax camera on top. Right: photography of a PCO. Dimax HS camera 73

Figure 52. Left: 3D rendering of the monochromatic beam microscope mounting a PCO. Edge 4.2 camera on top. Right: photography of a PCO. Edge 4.2 75

Figure 53. 3D CAD rendering of a tensile/compressive test rig compatible with microtomography experiments. 77

Figure 54. Cross section of the radiation furnace (right) and 3D rendering of the system (left). Different parts such as rotary feedtrough, parabolic reflectors and ports can be observed. 79

Figure 55. Conceptual design of the high-pressure set-up including the main components and the support 80

1. ABSTRACT

The FaX-ToR initiative has been initiated from the interest and support of a cluster of Spanish scientists covering a wide range of disciplines from fundamental to applied research. One of the key issues that motivate these researchers is accessing to the internal microstructure of their problem-substances and investigating about the dynamic processes occurring in them. Synchrotron X-ray imaging is, nowadays one of the most used techniques for this purpose. On the one hand, fast X-ray radioscopy allow understanding dynamic processes taking place in short times (mili- and submilisecond range) combining the fast imaging acquisition with the penetrating power of X-rays, although with the limitation of a 2D image sequence. On the other hand, synchrotron tomography provides a way for visualising and analyzing the three-dimensional interior structure of real objects non-destructively and with a high spatial resolution. In recent years different beamlines in Europe have focused their developments towards 3D+t or 4D techniques (combined with in situ approaches) with the objective of achieving a new technique, “real time tomography”, which combines 3D spatial resolutions of few microns and temporal resolutions bellow the second.

This proposal is oriented to the creation of future fast imaging beamline at Alba synchrotron which may cover the demands, not only of the Spanish scientific community but also the European ones. The instrument is conceived as a multi-purpose system that may allow the realization of diverse imaging techniques that will be explained and developed in this proposal. In the proposal we also consider the future development of the instrument aiming at extending the number of available techniques in the incoming years.

We believe that the creation of an imaging beamline with possibilities of developing 3D, in-situ, and real time studies constitutes a strong opportunity for Alba synchrotron for offering an alternative to a highly-demanded technique for european users.

2. INTRODUCTION

2.1. Importance of X-ray imaging and tomography

Several fields have experienced important progress over the last decades with the development of three-dimensional (3D) characterization techniques. The understanding of materials, animals, fossils, objects, etc. has gradually increased aided by the development of methods that provide as complete and unbiased description of microstructure as possible. From the 3D microstructure, quantitative information in three dimensions can be retrieved using methodologies based on image analysis techniques. 3D data provides access to some very important geometric and topological quantities such us size, shape, orientation distribution of individual features and that of their local neighbourhoods, connectivity between features and network, composition, etc. Some of these quantities cannot be determined a priori from classical stereological methods that use only 2D images or at the best only semi-quantitatively estimations are reached. Besides, the possibility to conduct in situ 3D characterization of dynamic experiments is expanding our view on fluid flow in porous systems, metal micromechanics or the architecture of food texture, to name a few.

Experimental methods that enable 3D characterization have undergone dramatic improvements in the past decade due, in large part, to advances in both computing power and visualization and analysis software that have been enabling factors for both the acquisition and interpretation of these massive data sets. Several 3D characterization techniques are available for scientists that span from the atom to the macroscopic engineering or natural components. Some examples are Atom Probe Tomography (APT) [1], electron tomography [2,3], neutron tomography [4,8], 3D X-ray diffraction (3DXRD) [5,8], serial sectioning (OM, FIB-SEM, 3D-EBSD) [6,7], X-ray tomography (XCT) [8-12], among others. The variety of 3D imaging methods is large, and they differ by the probing rays they use, by the physical quantity they measure and by the mathematical reconstruction technique they are based on. Figure 1 shows some of the commonly used characterization methods which cover a range of different resolutions and sample sizes (beginning and end of the bar respectively) over nine orders of magnitude [11].

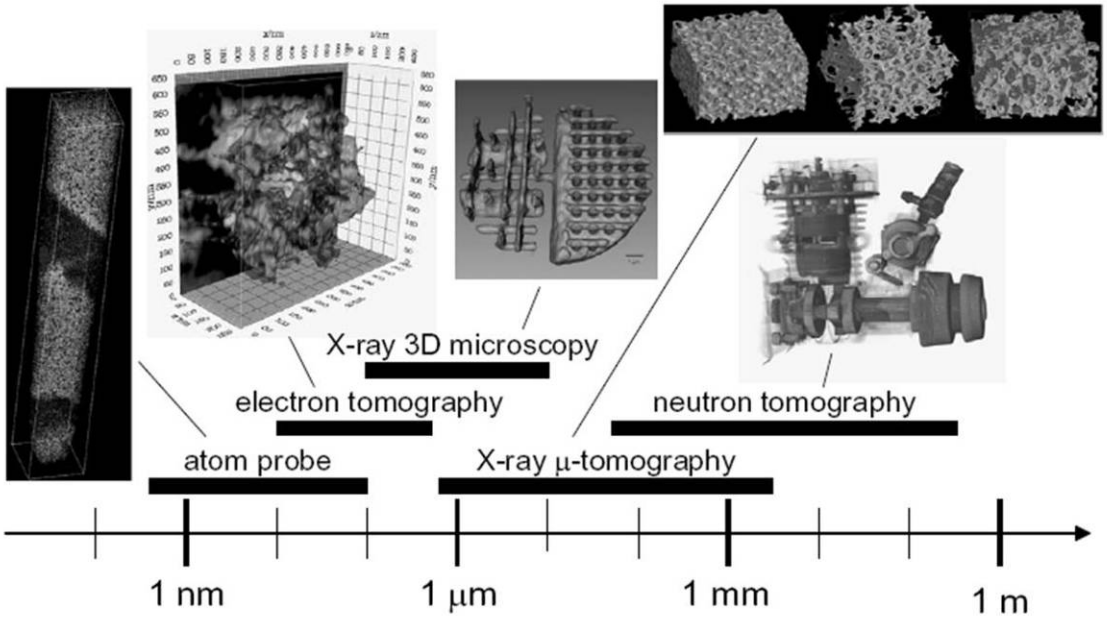

Figure 1. Tomographic methods spanning over 9 orders of magnitude [11].

2.2. Virtues of X-ray tomography

Absorption contrast X-ray computed tomography (XCT) is probably the most well-known 3D x-ray imaging method. In this mode it is possible to detect differences between x-ray absorption coefficients of different phases, provided they are different enough. This technique can be carried out with lower energy beams available on desktop instruments (for relative low density specimens). Indeed, commercial XCT instruments with resolution in the order of micrometers, have proliferated rapidly in recent years. Synchrotron radiation, on the other hand, provides the largest number of experimental options for tomography based on imaging (absorption tomography, phase-contrast tomography, holotomography, laminography, nanotomography, aborption edge tomography) as well as using diffraction (3D X-ray diffraction microscopy -3DXRD-, diffraction contrast tomography –DCT-), among others. One reason is the extraordinary brilliance of third-generation synchrotrons, many orders of magnitude higher than that of conventional X-ray tubes. This characteristic allows the possibility of selecting a narrow energy band (using monochromators) and still having a significant flux or use pink or white beams if higher fluxes are required, depending on the application. Also, the high coherence of synchrotron X-ray beam allows us to exploit the phase

interaction with objects of this radiation. SXCT also provides a range of resolution (Figure 1) that can be used to study the 3D microstructure and features of a wide variety of materials and have been a subject of study in different publications [9,13-22]. Other virtues are deep penetration, non-destructiveness (which provides temporal evaluation possibility), simple sample preparation and the possibility to provide chemical information.

2.3. Development of SXCT in the last decades

Synchrotron X-ray computed tomography (SXCT) has experienced a rapid development over the last 15 years achieving considerable improvements in spatial and temporal resolution, volume reconstruction speed and 3D methods of analysis that allows quantitative analysis of the tomographic data. As a consequence XCT and SXCT are progressively becoming an accepted tool for scientists and industry as a reliable and precise 3D characterization technique. This statement can be confirmed if we observe the scientific production directly related to synchrotron microtomography during the last decades (Figure 2). The consolidation of the technique is both in terms of indexed publication per year and visibility (Figure 2a-b), contributing directly to high impact scientific results (Figure 2b). In parallel, the particular interest of the scientific community in using SXCT for different purposes has lead to a beamtime overwhelming demand in most SXCT beamlines across the world reaching an overload factor of nearly 3 (higher in particular beamlines) in a short time. Interestingly the comparison with the use of diffraction techniques at synchrotron facilities reveals that relative productivity has become similar, as scientific interest on tomography has grown with years (Figure 2c).

Regarding the scientific production of specific techniques, nano-tomography (or zoom-tomography) and in-situ 4D tomography are probably the most interesting developments and, as a consequence, two of the most used tomographic techniques for the scientific community, highly increasing the demand of these techniques at the synchrotrons (Figure 2d).

Another important strength of SXCT is the versatility of the technique depicted in the multidisciplinary origin of the scientific production (Fig. 2e). This feature strongly

contributes to the expansion of instrumental development and experimental environments available at SXCT beamlines.

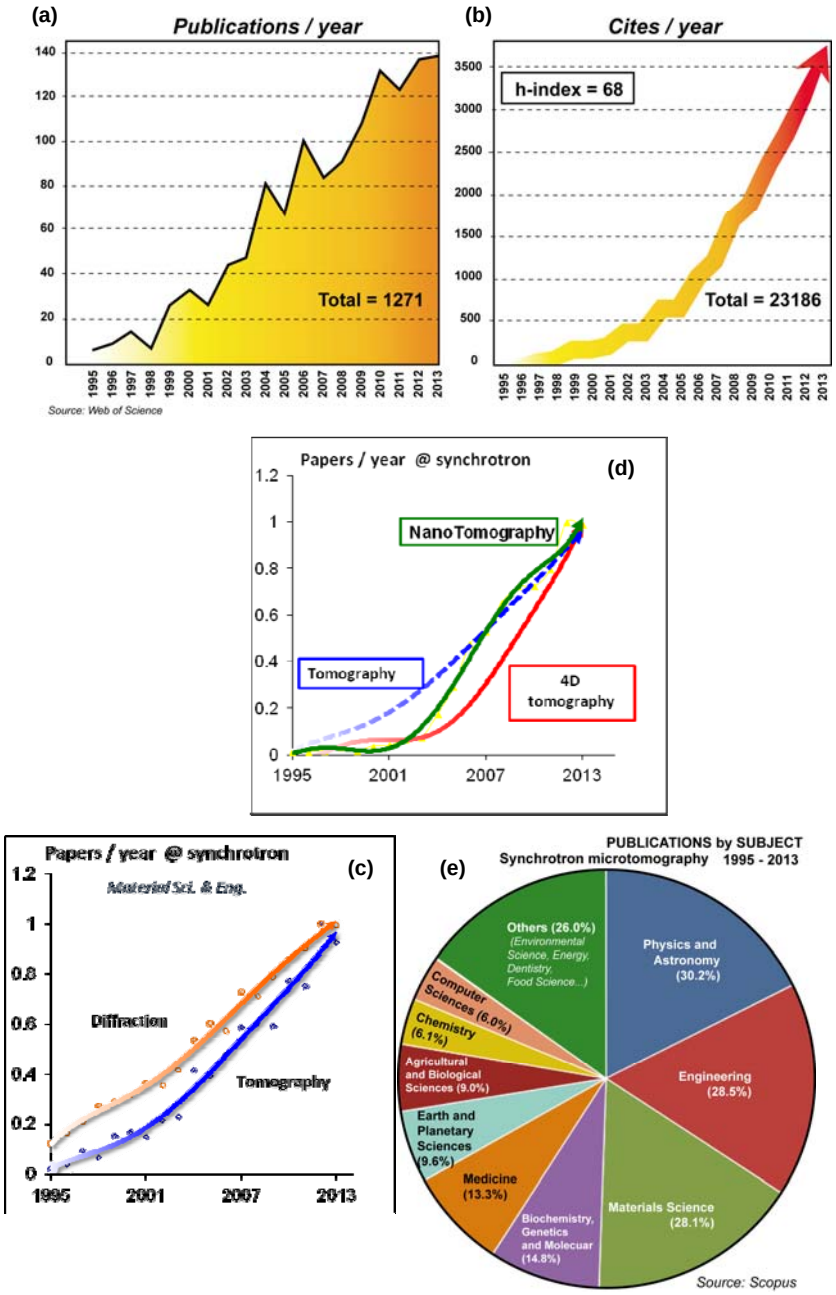

Figure 2. Scientific production considering synchrotron tomography over the last 20 years (a) Number of indexed publications (b) Cites per year, total number of cites and h-index for synchrotron tomography. (c) Scientific production considering synchrotron tomography and diffraction over the last 20 years. The number of papers is normalized to the maximum number of paper per year. (d) Relative number of paper for different specific tomographic techniques (normalized to the maximum number of paper per year). (e) Publication by subject for synchrotron microtomography. Source: Web of Science and Scopus.

2.3.1. 4D tomography

4D tomography refers to the possibility to perform a repeated series of 3D topographies at sequential time lapses, providing information about the microstructure evolution. This is one of the most attractive features of SXCT. As an example in material science and experimental mechanics, the evolution of structure can be very important during manufacturing [9], service life and in understanding failure mechanisms [17], as well as in understanding the process of breadmaking [28], and is proven to be a valuable method in other areas, too. One very important characteristic of 4D tomography is the temporal resolution that can be achieved in the measurement of one tomogram. In many cases, fast acquisition time are necessary, normally at expenses of spatial resolution; while in others, when the microstructure is quasi-static, longer measurement times with better spatial resolution are affordable.

4D tomograms can be carried out in several ways depending on its application. Ex-situ approaches can be used for long term treatment applied to the same samples provided they don't need to be cut for tomographic measurements. Some examples of that are corrosion studies, exposure to moisture and certain heat treatments that cannot be carried out in-situ. In some cases when the samples are larger than the field of view (FOV) of the detector the evolution of features are evaluated on different samples at different conditions (because specimens have be cut) and the extracted data are treated in a statistical way as function of time. An example of that is long-term creep studies, manufacturing defects or microstructural changes, etc. Per se, 4D tomography provides the evolution of a specific feature as a function of time, which in some specific cases can be linked to another variable (temperature, pressure, strain, etc.). The combination of 4D tomography with in-situ devices opens up other new possibilities and fields of research (see section 2.3.2).

Surface observation can be a useful approach, but in many cases structural changes occur in the bulk material at hidden view. 4D tomography allows following the structure evolution non-destructively in 3D manner. A significant amount of information can be obtained only from visualization of the events that occur in 3D over a time lapse, but in most of these cases quantitative information is also

required. Increasingly, the new trend is to obtain quantitative information from 3D and 4D tomography. This allows to understand the heterogeneities of the microstructure in 3D and 4D, and to evaluate the predictive capability of analytical or numerical models to describe behaviour and predict the kinetics of a certain mechanism. To that end, several approaches for quantitative analysis are been developed, such as digital volume correlation (DVC) [9,23,24], 3D particle tracking (3DPT) [9,25,26], however their application is still scarce. It seems natural that with the increase in applications these methods or new ones will become more efficient and with improved accuracy. Recently commercial codes have become available which will surely accelerate the dissemination of the technique even to the industry.

2.3.2. In-situ tomography

Another approach is to carry out in-situ studies in devices that are specially developed for that purpose. Initially, they were developed by the users and brought to the beamline for the experiment, but this also creates compatibility problems and lead to important time losses during the beamtime so nowadays it is common to find some of these devices (miniaturized furnaces, heating or cooling stages, tensile and compression rigs, etc.) at the synchrotron beamlines available for the users. We believe that an important asset for any tomography beamline is the possibility to carry out in-situ experiments of different kind using special devices that, at the same time, must be flexible in their configuration according to the high variance of applications. In our opinion, the proposed beamline should provide the users some of these devices for in-situ testing, namely tensile and compression testing rig with temperature regulation, ovens and/or heating stages. Some other less common but emerging devices are pressure anvils, high-temperature dilatometers, infusion rigs, fatigue testing rigs, corrosion cells, etc. Of course some of them could even be combined to provide an even broader spectrum of testing.

Tomographic temporal resolution is an issue still addressed by only a few European synchrotrons, while in others the acquisition time is still in the order of hours. The increase in temporal resolution is opening up a set of possibilities for tomographic imaging applications that cannot be studied easily by other means. Considerable

improvements have been made in recent years by combining the very intense white (or pink) beams at synchrotron sources with a new generation of high-speed cameras and new types of scintillators. Timescales for one tomography is nowadays in the order of tens of milisecons [27], allowing studies in many different fields such as food (bread making or beer foam) [28,29] or in material science for coarsening, melting, solidification of semi-solid metals, as well as damage assessment.

2.4. Scope of this proposal

This proposal mobilizes the expertise from specialists from different fields (material science and engineering –from polymers to nickel superalloys–, bioscience, food science, earth science, palaeontology, volcanology, metrology, etc.) to propose the design of an X-ray imaging beamline that provides a high resolution tomography instruments that will permit to carry out different modalities (absorption, absorption-edge, phase contrast and holo- tomography) with optimum temporal resolution with expected times per tomography below 1 second. Except for absorption mode (without considering the exceptional expected speed at the beamline) the other 3 last-mentioned tomographic techniques are not available in conventional laboratory sources. Of course, it could be also possible to carry out fast radiography experiments, over 500 images per second, in those cases where 3D resolving power is not required. The beamline concept is completed by proposing different in-situ devices that will be available for users. In this field, it is becoming clear that, allowing the observation of the interior of a sample without requiring a specific (and possibly biasing) preparation procedure, X-ray tomography is the best way to obtain reliable information on the microstructure and its evolution, also under different loadings (e.g. mechanical or thermal).

Considering the versatility of the instrument, the combination of different tomographic techniques and the availability of in-situ devices make this future beamline attractive for a large number of potential users from many different fields, which makes SXCT an essential technique in a synchrotron. Such tomographic beamline will provide a valuable asset to the scientific community that will attract researchers from many different areas not only from Spain but from the rest of Europe.

3. THE SPANISH (AND EUROPEAN) USER COMMUNITY

3.1. Current panorama of SXCT in Europe

In Europe we can find 8 different synchrotrons with beamlines oriented to X-ray tomography (soft X-ray microscopy, nanotomography and non-imaging tomography –difraction, fluorencence, etc.– have not been included in this selection). Figure 3 show their location in Europe (3 in Germany, 2 in France, 1 in UK, Italy and Switzerland). According to this list, other synchrotrons in Europe have not been considered (e.g. Alba) since they do not have any beamline dedicated to X-ray tomography in the terms previously mentioned.

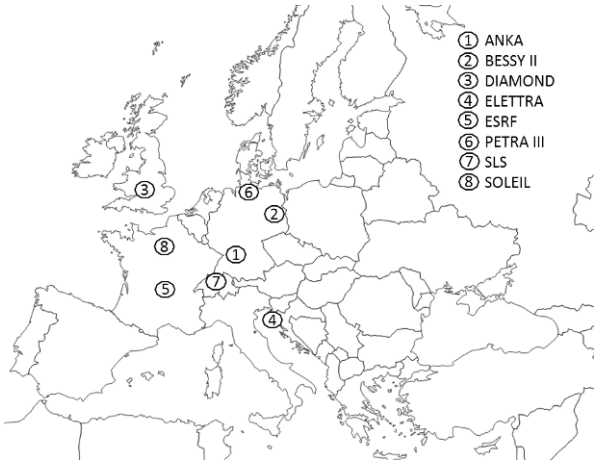

Figure 3. Map of Europe including the list of European Synchrotrons with available tomographic techniques.

Complementarily, Table 1 lists the name of these beamlines, together with the available tomographic techniques and the energy range. From these results we can state that a total of 12 beamlines in Europe are currently dedicated to X-ray tomography and have developed different tomographic techniques. Nevertheless, they are not many if we compare them with diffraction, XANES, or XAS beamlines present in Europe in the different synchrotrons. Actually the overload factor of these beamlines is, by far, higher than others types of techniques and therefore it would be interesting to complete the current European offer of SXCT with a new tomographic beamline at Alba. It is also important to mention that only two beamlines have oriented their developments to fast tomography. In this sense

TOMCAT (SLS) [27] and ID19 (ESRF) [30] are currently the leaders in this aspect reaching up to 20 tomograms per second. The FaX-ToR proposal aims at offering a new beamline for the realization of Fast X-ray Tomography and Radioscopy with special emphasis for in-situ studies and, thus, completing the current offer for SXCT in Europe.

Table 1. X-ray tomography –imaging– beamlines available in Europe

Beamline	Synchrotron	Tomography techniques	ENERGY (keV)
IMAGE	ANKA	2D: microscopy, radiography, topography, and microdiffraction imaging 3D: tomography and laminography with monochromatic, pink or white beam (high contrast to ultrafast) – Not available for users yet	7 - 65
TOPO-TOMO	ANKA	White beam X-ray tomography (submicrometer) Phase contrast imaging with grating interferometer.	6 - 40
BAMline	BESSY II	Monochromatic Tomography (Si 111 and multilayer), White beam Tomography.	5 - 90
I12-JEEP	DIAMOND	White beam X-ray Tomography Phase contrast imaging.	50 - 150
Diamond Manchester Imaging Branchline	DIAMOND	Pink Tomography and Monochromatic Tomography.	8-30
SYRMEP	ELETTRA	Monochromatic Tomography (Si 111) White beam Tomography.	8-35
ID-16A Nano-Imaging Beamline	ESRF	Nano-Tomography	17.0 - 33.6
ID19 Microtomography beamline	ESRF	Micro-Tomography, phase contrast, holotomography (res.: 0.3 -30µm). Fast tomography (few sec.). Diffraction Topography	6.0 - 100.0
IBL (PE05)	PETRA III	Nano-Tomography Micro-Tomography (Absorption & Phase Contrast Tomography)	5 - 50
HEMS (P07)	PETRA III	XRD, SAXS, 3D-XRD, Tomography with 1 µm focus (based on absorption and phase contrast)	30 - 200
TOMCAT	SLS	Absorption based Tomographic Microscopy; Propagation phase Contrast Tomographic Microscopy Differential Phase Contrast (DPC) Tomographic microscopy Absorption and phase contrast nano-tomography Ultrafast tomographic microscopy.	8-45
PSICHÉ	SOLEIL	Monochromatic high energy resolution Tomography Monochromatic high flux Tomography.	15-100 keV white beam (low energy filtered) 15-50 keV monochromatic

3.2. Potential users in Spain

In the preparation of this proposal we scanned the interest of the Spanish scientific community in this technique by carrying out a mailing survey. As a result of this poll, more than 25 Spanish research groups were interested in this technique and decided to support this proposal. Table 2 lists the groups, the institution and the research interest obtained from the mentioned survey. One of the main characteristics of this

supporting cluster is their multidisciplinarity considering the high variety of research interests they represent, which actually provide an added-value to this proposal. Figure 4 shows the distribution within the Iberian territory of the groups listed in Table 2.

One of the main conclusions of the survey is that we believe there is a significant critical mass of groups that will be demanding this technique at Alba when the beamline is ready. Additionally we are pretty sure that many other research groups and companies will become users when they could see the results obtained by other groups/colleagues. Finally we have to consider that it is expected that this beamline will be also requested by European users as it will be analyzed in next section.

Table 2. Spanish research groups supporting the FaX-ToR proposal

Leader	Group/Institution	Interest
J. Gómez Barreiro	U. Salamanca	High pressure and temperature of geological materials
R. Campos Egea	CIEMAT	Geological materials
J. Costa Balanzat	U. Girona	Composite Materials
J. C. Gálvez	U Politécnica de Madrid	Fracture of Steels and Cement based material
L. E. Hernández	U. Autónoma de Madrid	Vegetal materials
J. Sánchez	(IETcc-CSIC)	Structures, concrete
M. Lanzón	U. Polytechnical Cartagena	Building materials, stone, patrimonial buildings
D. A. Cendón Franco	U. Polytechnical Madrid	Metallic materials
F. San Jose Martinez	U. Polytechnical Madrid	Soil structure
F. A. Lasagni	CATEC	Composite materials and metal alloys
V. Gomez Ruiz	U. Oviedo	Geomaterials
G. Garcés Plaza	CENIM	Multiphase metallic materials
J. A. Yagüe	U. Zaragoza	Metrology, Image treatment
L. Franco Ferreira	Aimen	NDT, dimensional metrology, material characterization
A.Mendikute	IDEKO	Image treatment, non-destructive testing
J. van Duijn	U. Castilla La Mancha	Solid Oxides bateries
V. Amigó	U. Politécnica de Valencia	Titanium alloys characterization
C. Capdevila	CENIM-CSIC	Fe-based alloys, steels
L. Galdos	U. Mondragon	Super Plastic Forming of Aluminium Sheets.
P. Bravo	U. Burgos	HPDC of Mg alloys, polymers
J. C. Suárez Bermejo	U. Polytechnical Madrid	Structural hybrid materials, adhesivos, damaging
M.A. Rodriguez-Pérez	U. Valladolid	Cellular materials, X-ray technique development
D. Val	GRUPO ANTOLIN-IRAUSA, S.A.	Magnesium and aluminium alloys
R. Arenas Martín	U. Complutense de Madrid	High pressure metamorphic rocks
F.J. Sierro Sánchez	University of Salamanca	– Micropaleontology
Sören Jensen	University of Extremadura	Paleontology Group
I. Rosales	Spanish National Geological Survey	Geology
G. Garcés Plaza	CENIM	Multiphase metallic materials
A. Álvarez Valero	University of Salamanca	Volcanology

J.R. Martínez Catalán	University of Salamanca	Tectonics y geophysics
A. Rodríguez Barbero	University of Salamanca	Renal and cardiovascular physiopathology
P. Ayarza	University of Salamanca	Geophysics: Seismic y Magnetisms
J.M Benítez Pérez	University of Salamanca	microstructure characterization
E. González Clavijo	Spanish Institute of Geologicy and Mines	Tectonics and natural resources
M. Suárez Bárrios	University of Salamanca	Crystallography and Mineralogy
C. González	IMDEA Materials	Fibre reinforced polymers
T. Perez Prado	IMDEA Materials	Light metal alloys
J. Molina	IMDEA Materials	Micro- and Nano- mechanics metallic
F. Sket	IMDEA Materials	FRP; light metal alloys; steels

Figure 4. Geographic distribution of the supporting cluster in the Iberian territory.

4. RELEVANT SCIENTIFIC CASES

X-ray radiography and tomography can be applied to several scientific and industrial fields, therefore it is no easy to organize the research areas in which tomography was or could be applied. We have subjectively selected some research categories which in some cases the scientific cases will overlap other categories.

4.1. Multidisciplinary Fast tomography and radiography: in-situ studies

In many research areas, evolution of the structure is of prime importance. As a non-destructive technique, X-ray CT can provide a very detailed picture of the evolution of the structure/damage through a certain processes applied to a material. Furthermore the opportunity to host environmental stages means that structure/damage can be followed in situ under a range of demanding conditions representative of those experienced in reality. Consequently SXCT enables the quantification of a very wide range of structural changes and damage mechanisms. Some examples are presented below.

4.1.1. Bubble nucleation and growth characterized by ultrafast tomography

The use of X-ray tomography brings the possibility of performing detailed characterizations of the cellular structure of foam specimens in three dimensions (3D) although in general tomographies are acquired in static conditions. In evolving systems it would be expected that the high number of projections and the relatively long exposure time needed may output blurred tomographies. Thanks to the last developments at synchrotron beam-lines nowadays it is possible to carry out time-resolved X-ray tomography studies reaching time resolutions unimaginable a few years ago [29].

This study uses synchrotron time-resolved X-ray tomography to understand the effect of nanoparticles on the bubble generation –nucleation- and its later evolution –growth- of a reactive polyurethane foam formulation. The time resolution of the performed experiments was 156 ms per tomographic scan (near to 10Hz micro-

tomography) and a total number of 90 tomographies during the foaming process where acquired.

A commercial bi-component polyurethane (PU) formulation from BASF was selected for this investigation. The turbulent mixing of two liquids (polyol and isocyanate) promotes a simultaneous blowing and gelling reaction that results into a solid foam. The density of the foam in a free foaming process is 52 kg/m^3. The nucleating nanoparticle selected for this investigation was hydrophobic fumed silica and to this end 3 %wt. of silica nanoparticles were initially dispersed for 120 s in the isocyanate compound.

A specific set-up (Figure 5) was developed to mix the isocyanate (neat formulation or the blend containing the particles) with the polyol in the same rotating table in which the sequences of tomographies were taken. This allows obtaining information from the initial stages of the process. The polyol and isocyanate components were placed in a dedicated miniature cylindrical mold (h=40mm, Ø=12mm, thickness=75 μm Kapton walls), attached to the tomography rotating table. A motorized miniature stirrer at the top was automatically immersed in the liquids and stirred the mixture for 15 seconds at 1500 rpm promoting the blowing and polymerization reactions. The tomography scans started 10 seconds after the end of the mixing process.

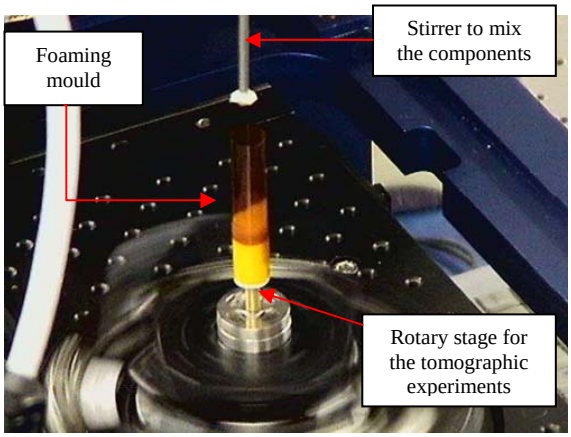

Figure 5. Detail of the stirring head over the kapton mould containing the isocyanate and polyol blends before the mixing process.

X-ray tomographic experiments were performed at the TOMCAT beamline of the Swiss Light Source at the Paul Scherrer Institute (Villigen, Switzerland). The ultrafast end-station incorporates a PCO.Dimax camera, which acquires and transfers data orders of magnitude faster than CCD cameras. The optics were coupled to a LuAG:Ce

100 µm thick scintillator screen. Magnification of x4 in the optical microscope lenses was selected for this experiment. This corresponds to a pixel size of 3.2×3.2 μm^2 and a field of view of 6.44×6.44 mm^2. Monochromatic X-rays (20KeV, no filter) were used; generating 300 projections captured over 180° of rotation with a total scan time of 156 ms. Span time of 2.5 s was used in between scans. Reconstructions were performed by using the GRIDREC algorithm [31,32] coupled with Parzen filtering of the sinograms.

Reconstruction of the tomographic scans allows visualizing, in 3D, the cells nucleation and growth processes from the early stages in both studied materials. Figure 6 shows the corresponding 3D renderings for four selected instants (9.8s, 21.7s, 26.3s and 32.6s.) during the foaming process. It is possible to appreciate the higher cell size in the neat PU formulation and the smaller size together with a much higher density of cells in the foamed nanocomposite containing hydrophobic silica.

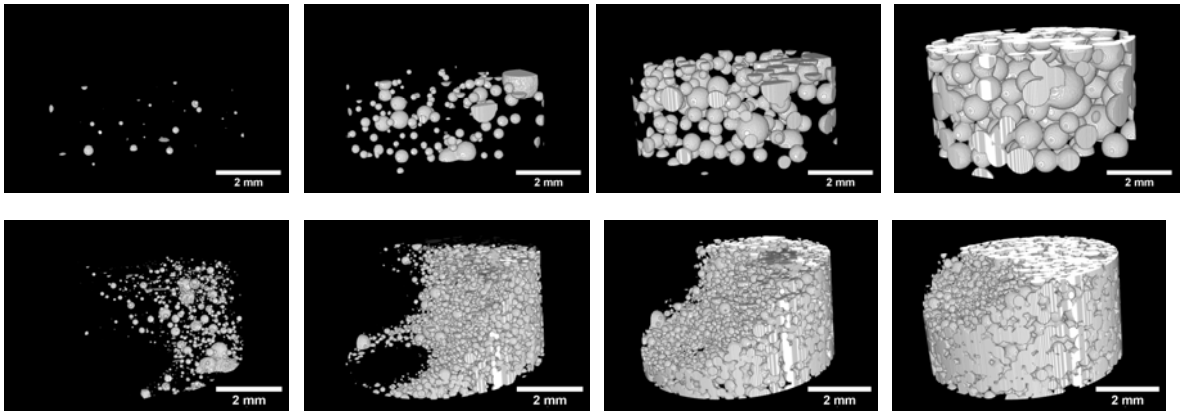

Figure 6. Volume rendering at different instants for the two examined materials
(TOP: pure PU; BOTTOM: PU with 3 %wt. nanosilica) at (a) 9.8s, (b) 21.7s, (c) 26.3s and (d) 32.6s).

The analysis of the tomographic sequences allows determining the number of cells per cubic centimetre and the average cell size evolution. Figure 7, left, shows the cell density evolution <*N*> during the foaming process. The results show that the cell density increases linearly during the first 10-15 seconds and subsequently slows down with time. It is also clearly observed that the nucleation density is higher for the composition with 3% wt. of silica nanoparticles since these fillers could facilitate bubbles formation at solid/liquid interfaces due to a free energy barrier reduction [33]. On the other hand, the experimental results for the cell size evolution with time

by several authors for the initial bubble radius evolution [34,35]. Bubble growth stabilization is not observed and the modelling done is then valid in our study since the results presented here only focus on the first 50s of the expansion. It is also possible to observe that average cell diameter keeps constant in the very early instants (t<10s), while nucleation is taking place. As soon as nucleation has been accomplished, the gas dissolved in the polymeric matrix starts to fill the cells at a constant rate causing the growing process.

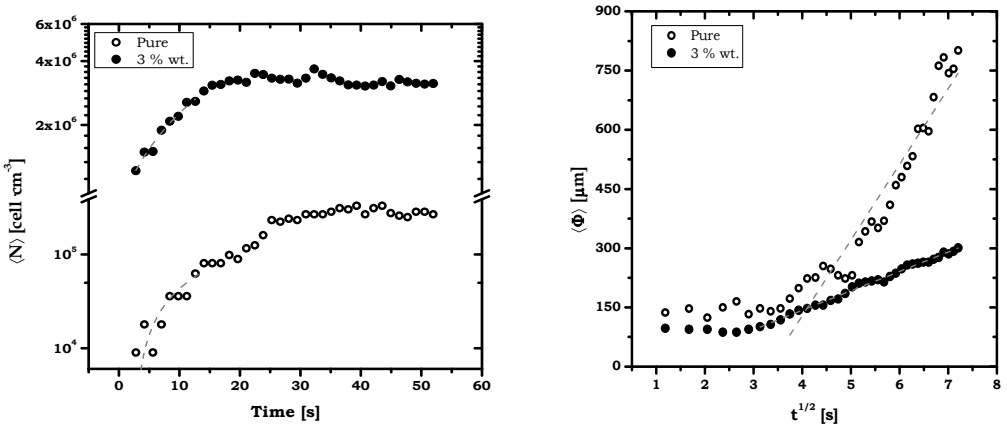

Figure 7. Left: In-situ cell density evolution compared models. Right: In-situ cell diameter compared with the theoretical models.

4.1.2. In-situ solidification of Al alloys

The pressure to reduce weight in structural parts used for transport has increased the interest in the most important engineering light metals, namely Mg, Al and Ti. It is in this field where X-ray tomography is giving some of its most important contributions. Some recent milestones include:

a) The possibility to follow in situ the solidification process of Al-alloys. In castings, the architecture of the alloy is largely determined by the solidification parameters that drive the solidification kinetics (e.g. cooling rate and temperature gradient in the melt), [36-38].

b) The application of in situ studies of damage evolution during room temperature and high temperature tensile deformation and fatigue [39-41] of Mg- and Al-alloys.

The investigations mentioned in a) and b) have been made possible thanks to the development of fast and ultra-fast X-ray tomography at some synchrotron beamlines

allowing acquisition times of a complete tomogram in less than one second with voxel sizes down to ~1 μm^3 [42].

c) The applicability of phase contrast tomography to determine the internal architecture of light alloys formed by phases with very similar attenuation such as α-β Ti alloys, AlSi and AlMgSi alloys [43-45].

d) The exploitation of K-edge subtraction technique to identify concentration variations of different aluminides in Al cast-alloys during thermal treatments [46,47].

e) The achievability of sub-µm resolution to reconstruct the architecture of multiphase Al and Ti alloys [44,47,48].

Cast AlMgSi alloys are potential candidates to be used in the automotive and aerospace industries [49]. The investigation of the kinetics of solidification is necessary to understand how casting parameters, such as cooling rate and temperature gradient in the melt, affect the development of the internal architecture of alloys and consequently determine their resulting mechanical properties. The formation and the evolution of the microstructure of an AlMg4.7Si8 alloy were investigated by in situ synchrotron tomography (SXCT) during solidification [38]. The experiment was carried out at the ID15A beamline of the ESRF using a pink beam and a total scanning time of about 15s for each tomogram. SXCT was performed every minute, while a molten sample was solidifying at a cooling rate of 5 K/min.

Figure 8 shows reconstructed tomographic slices extracted from the in situ solidification experiment of the AlMg4.7Si8 alloy. The experiment allowed determining the sequence and temperature of formation of the different phases, as well as their location and distribution during solidification.

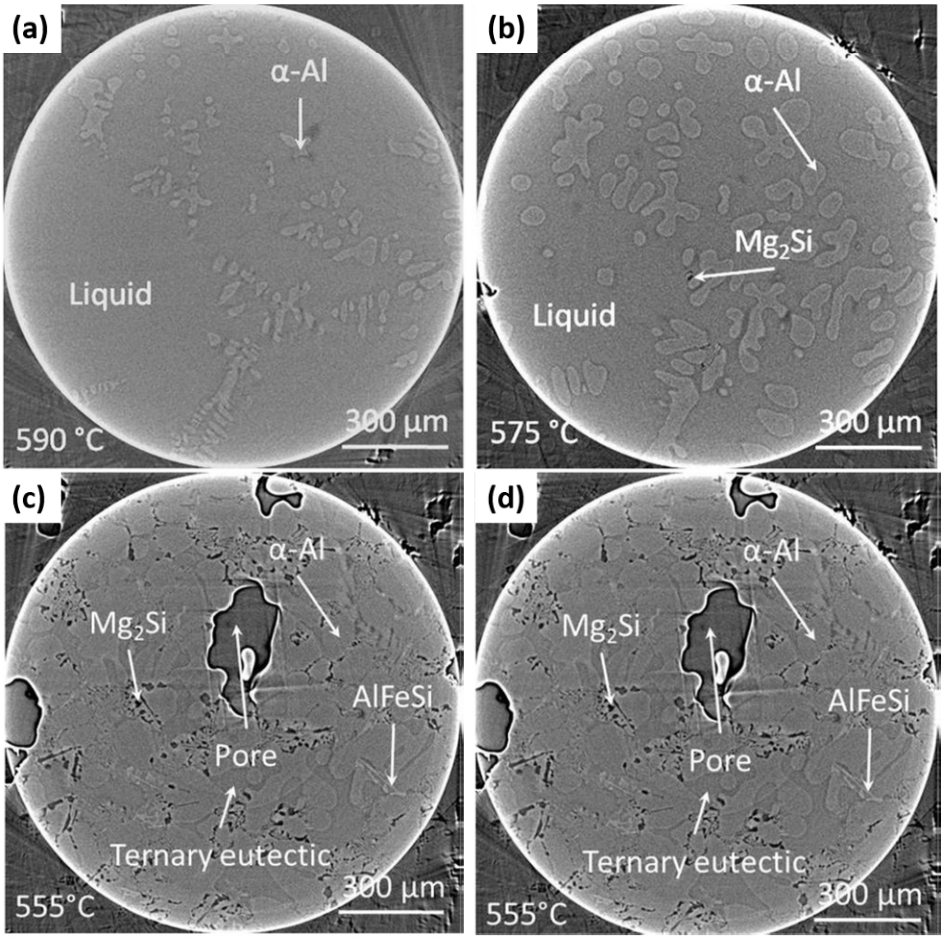

Figure 8. Reconstructed tomographic slices obtained during in situ solidification of AlMg4.7Si8 at the temperatures at which consecutive solidification of the different phases is observed, [38].

Rendered 3D images of the α-Al dendrites solidified at different temperatures during cooling are shown in Figure 9a) to d). The colours represent the Gauss curvature between -0.005 µm^2 and 0.005 µm^2, while the grey parts are out of this range. Figure 9e) to h) show the distribution of the mean and Gauss curvatures of the surface of the α-Al dendritic structure at the different stages (temperatures) of the solidification process. The characteristic morphologies for the axes and for each quadrant are indicated schematically Figure 6e). It can be seen that two maxima emerge during solidification: one closer to the origin representing slightly saddle-like shapes, which are related to the bases and sides of the secondary dendritic arms, and another in the positive-positive quadrant representing spheroid-like regions owing to the secondary dendrite tips. This indicates that the morphology of the dendrites during cooling is characterised by coarsening, which is a simultaneous process of growth and coalescence of the secondary dendrite arms, similarly to the

case of isothermal coarsening [50]. As the solidification advances, the growth of the secondary dendritic arms becomes asymmetric, the tips grow with a higher rate than the bases, resulting in a droplet-like shape, where the tips of neighbouring arms can coalesce [50,51].

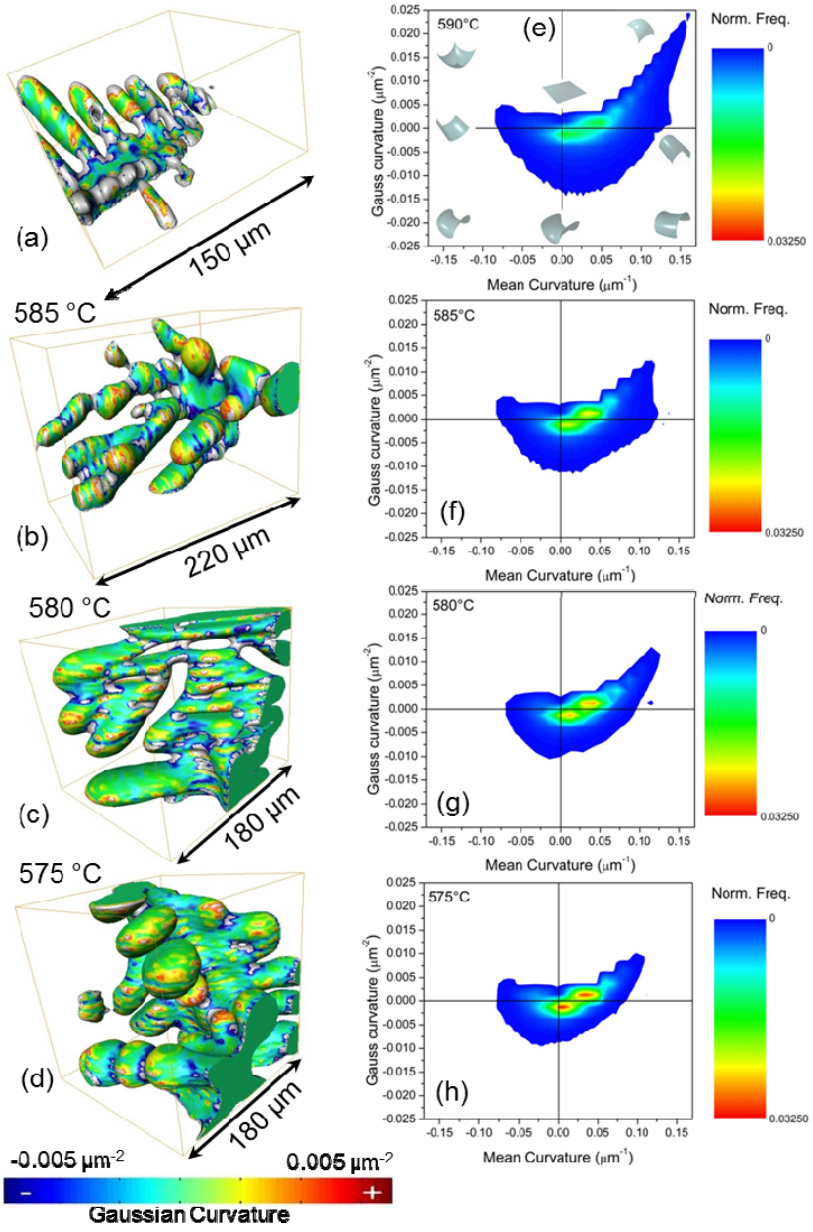

Figure 9. a) to d): rendered 3D images of the α-Al dendritic solidification at different temperatures during cooling of an AlMg4.8Si7 alloy obtained in situ by SXCT. e) to h): distribution of the mean and Gauss curvatures of the surface of the α -Al dendritic structure at the different stages of the solidification process. [38]

4.1.3. Understanding explosive volcanoes: risk evaluation through morphometric analysis of bubbles and crystals in lava

About 500 million people are living near active volcanoes and therefore a reliable evaluation of the natural risk in those areas is of primary importance. The potential of explosive eruption has to be determined on the basis of quantitative evaluation of the physical processes occurring at certain depth in the volcanic system. Access to those levels is restricted to erupted fragments and indirect measurement from outside. In this line, quantitative microtexture analysis of both erupted clasts and in-situ melting experiments has recently becoming the focus of attention of geologist and geophysicist since explosive potential of a volcanic system appears to be very related to the degassing path of melt all through the ascending conduit [53,54]. Through the detailed analysis of bubble shapes and interconnection, parameters like bubble coalescence and textural relaxation are connected with the physical response of melts [55]. The so-called vesiculation processes in magmas determine whether the eruption become effusive of explosive, so both in-situ experiments and analysis of selected natural samples are needed to advance in our knowledge on vesicle nucleation, growth and coalescence, and their connection with permeability evolution of melts [54]. A dependence of the microtexture with magma composition has been known at macroscopic level, but not completely understanding at the microscopic detail. While basaltic composition seems to evolve towards non-explosive eruption as porosity increases (Figure 10, [53]), silicic counterparts are less known, and hence more unpredictable [56].

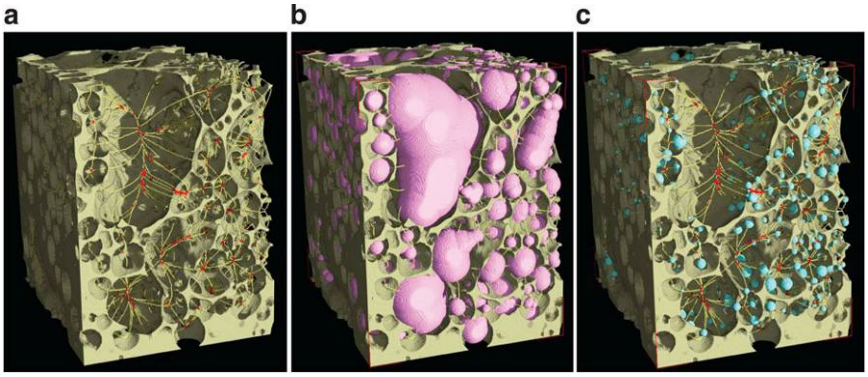

Figure 10: Bubble size, wall thickness and interconnection from basaltic foams [53]

Particularly striking is the case of silicic eruptions which seems to alternate between violent eruptions and gentle ones. It has been demonstrated that the way in which volatiles escape from the shallow part of the volcano conduit, determine such a behavior [54]. One critical issue is to understand how bubbles nucleate and grow in response to decreasing pressure as magma rises toward the surface. Synchrotron microtomography analysis on Kilauea's pyroclast has showed the complexity of bubble generation at different pressures during 2008 eruption [56]. Pyroclasts were imaging at ALS synchrotron facility at 20keV, 200ms exposure time and 1400 rotation steps between angles of 0° and 180°. Three main pyroclastic types were found, which depicted large bubbles (mm) surrounded by micrometric-thick haloes that contains an elevated number of small isolated round bubbles (radius= 2.5µm - 35µm, Figure 11 A)-D) [56]).

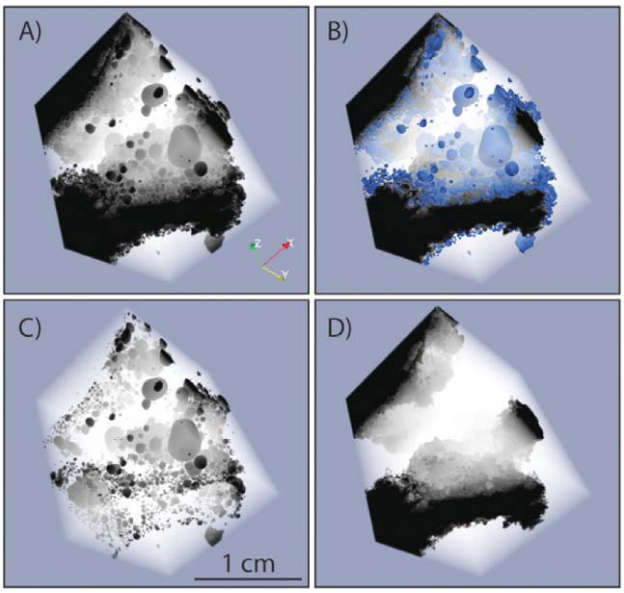

Figure 11: Different pyroclastic microtextures from silicic melts. Bubbles appear segmented [56].

The microtexture found in those pyroclasts reveals a high density of small bubbles within the haloes, pointing to nucleation rates relatively high, but with little time for coalescence. This important fact support the ideas that water concentrations are only high enough in the close range of large vapor bubbles prior to eruption [56,57]. The existence of a thin region around bubbles where melt with dissolved water occurs. It is an intimate result of pre-eruption and it is interpreted as a water

reabsorption back into magma prior to eruption. Those textures could also be used to track convective behavior at a macroscale within the volcano.

Recent developments include in situ investigation of magma vesiculation at high temperature. Heating systems combined with ultrafast acquisition, like those implemented in TOMCAT beamline (Figure 12 a-b; [27,58]) are of the most interest for melt foams research [59] but also in similar materials on e.g. management of nuclear waste [60].

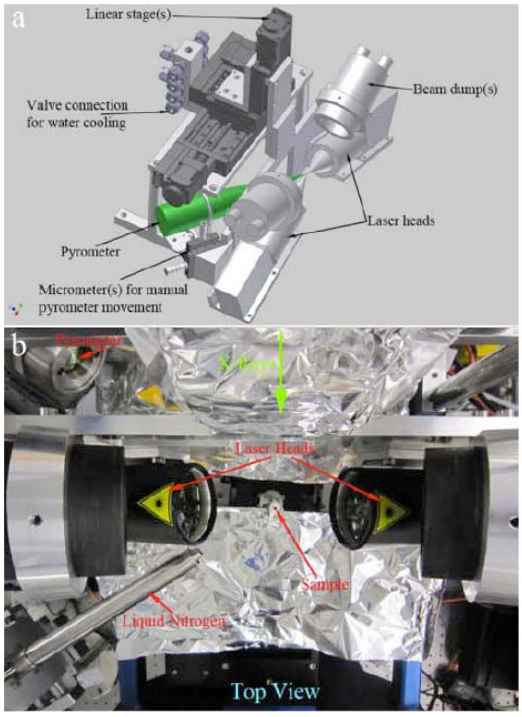

Figure 12. (a) 3D design and (b) top photograph of the laser system mounted on TOMCAT beamline at SLS. T range is 400-1700ºC [58,59]

The application of this experimental system to the investigation of vesicles development in acid melts at different temperatures is showed in Figure 13, [59]. Interestingly, shape and volume analysis reveals a connection of rigid and soft behavior of bubbles with magma rheology [61], providing crucial parameters for understanding how the viscosity of melts and gas overpressure during degassing processes control magma ascent along volcanic conduits. This is crucial to predict explosive eruptions in those systems [59].

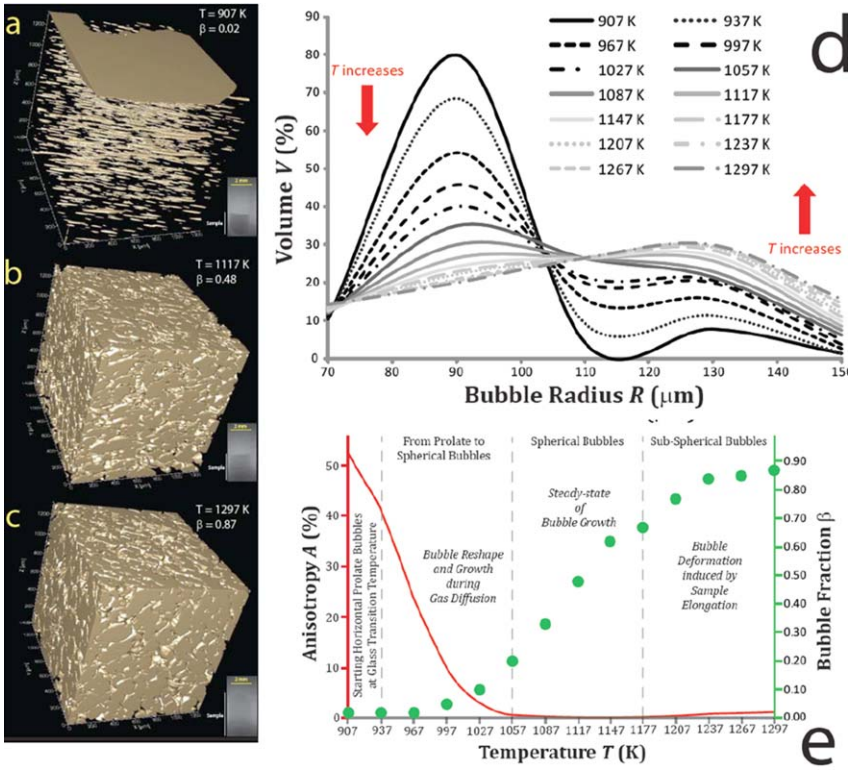

Figure 13. a-c 3D rendering of acid melt at different temperatures (bubbles); d) bubble size distributions at different temperatures; e) bubble anisotropy and fraction versus temperature [59].

4.1.4. Food science: tasting the texture

The physiochemical, functional and in some cases nutritional properties of food are intimately controlled by its microstructure. The quantitative analysis of food microstructure has become critical in order to understand the physical and rheological behavior as well as sensory attributes of foods. Food processing are now changing toward to the microstructure level design and testing, and x-ray microtomography is the technique of choice for visualizing those systems. Microstructural elements such as air bubbles or cells, starch granules, protein assemblies and food biopolymer matrices contribute greatly to the identity and quality of foods [62,63].

The microstructure of food has a strong influence over the attributes of a product as evaluated by consumers. Many of those macroscopic properties are poorly understood because of their complex nature, deriving from multiple interactions of processes and food micro-components [63].

Example of that interconnection between microstructure and complex physicochemical processes, and the profound impact of texture on the taste and flavor quality is found many products like fruit [64,65], bread [28,66,67] and coffee [68] to name a few with a very high social and economic impact. Both fruit and baked products share the strong dependence on their cellular structure that could be optimized through appropriated design during growth and production and will determine transport/distribution strategies and mid-long term durability of the product. In the case of bread, 3D imaging through x-ray microtomography combined with fast acquisition has proven to be very efficient way to understand cell structure evolution during proofing time (Figure 14, [67,68]). These results can be used to improve the design and production of not only bread but other biopolymeric foams.

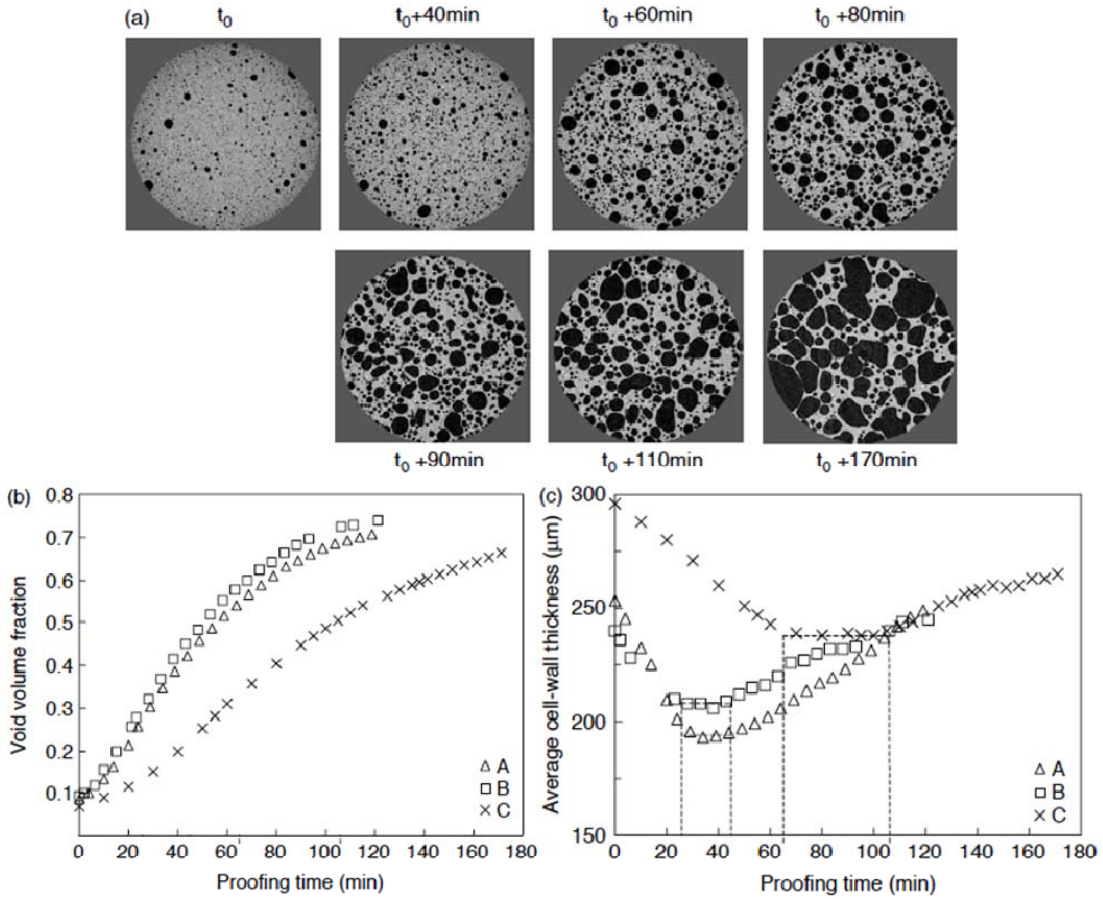

Figure 14. Evolution bubbles in bread during proofing: (a) 2D images of horizontal sections (diameter 9 mm) extracted from reconstructed volumes (628x628x256 voxels) (b) and (c) Void volume fraction and average cell-wall thickness for three different doughs [68].

In the case of fruits, the microstructure determines mechanical and transport properties of tissues. Therefore, a quantitative description of fruit tissue components in 3D are critical, both to understand the properties and to develop structure reliable numerical models on them. Figure 15 shows an analysis of SXCT data on fruit tissue from where important parameters were obtained: cell wall, pore network and cell size. These components were then used to design a numerical model to run multiscale mechanics and mass transfer, thus providing a solid framework for virtual tissue generation, including cell growth modeling. This strategy provide a unique tool for moving from geometric description to physical model of fruit tissue [65].

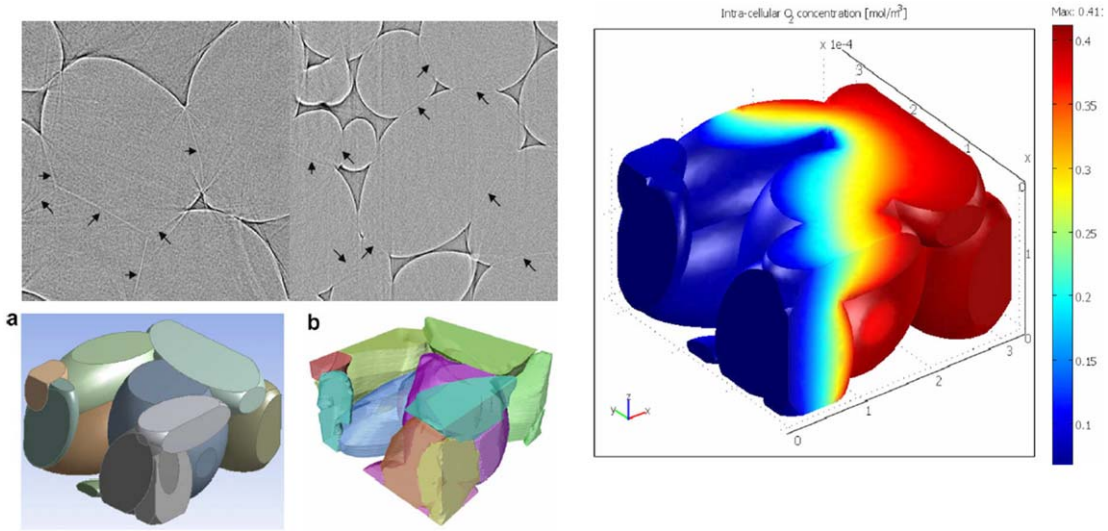

Figure 15. (upper left) Synchrotron radiation tomography: phase contrast slices of the fruit cortex of apple (left) and pear (right); cell walls are indicated by arrows. (lower left) Modeled (a) against measured (b) 3-D geometry of apple cortex cells. (Right) The oxygen concentration profile inside cells using finite element simulations. Driven force was partial pressure across the boundaries of the tissue. The partial pressure and concentration inside the tissue was related by the universal ideal gas law [65].

4.1.5. Ultra-fast 2D Radioscopy on cell wall ruptures to study metal foam stability mechanisms

Third-generation synchrotron light sources deliver a polychromatic X-ray photon flux density high enough to perform radiography with micro-resolution in both space and time [69-72]. The rapid development of imaging hardware, especially in the field of CMOS sensors, and their continuously improving sensitivity now allows for extraordinarily high recording speeds, with exposition times down to 1µs for a

considerable (at least 10×20 mm^2) field of view. The optimized use of so-called X-ray inline phase contrast (due to the coherence properties of an X-ray synchrotron beam) allows for the best possible contrast for our cellular material. Additionally, radiation hard but highly sensitive and efficient single crystal scintillators such as LuAG:Ce or YAG:Ce crystals are employed. This permits us to follow the overall process and resolve in-situ not only slow processes (>1ms exposure time) such as pore nucleation and growth, foam expansion or drainage, or simply observe the overall foaming process, but also very fast ones (≤1ms exposition time) such as cell wall rupture, bubble coalescence, rapid bubble motions or oscillations. Figure 16 shows the improvement of time resolution for X-ray synchrotron radioscopy on metallic foams achieved in the past years as reported in the literature [71-76].

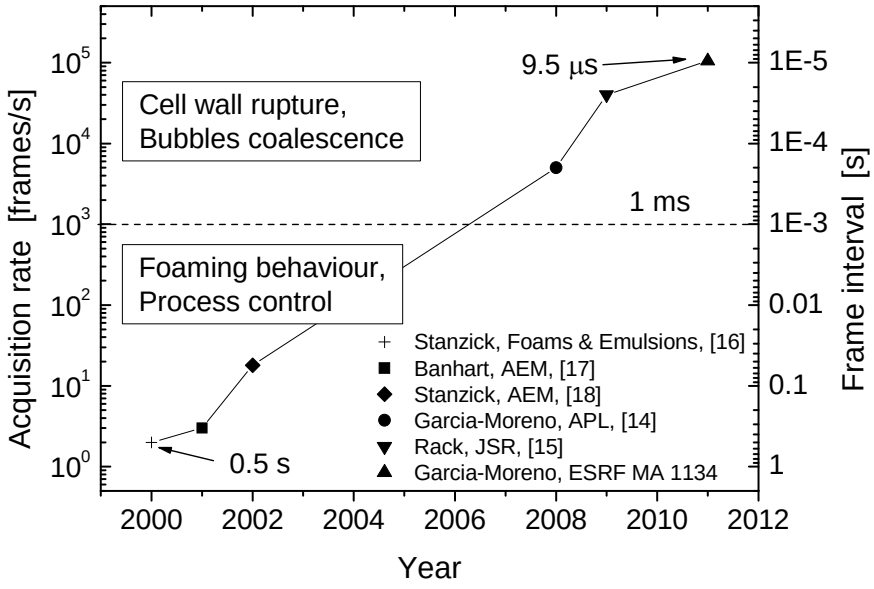

Figure 16. Evolution of time resolution for in-situ synchrotron X-ray radioscopy applied to visualize metal foaming.

The stabilization of metal films —or cell walls— in liquid foams is a key issue in metal foam science but still not fully understood. To investigate the nature of rupture, experiments have been performed in which there was a simultaneous demand for both high spatial and high time resolution. It was possible to observe the coalescence of two adjacent bubbles with a recording speed of 105,000fps with a frame interval of 9.5µs and effective pixel size of 20µm. Although the contrast of

such images is low due to the short exposure time and consequent limited dynamics of the images, it is clearly visible in Figure 17 that the coalescence of two bubbles is completed in ~475µs and that the rupture of a film lasts for ~380µs, if we consider the end of the rupture as the point where the contour of the new bubble becomes straight before it ends as convex.

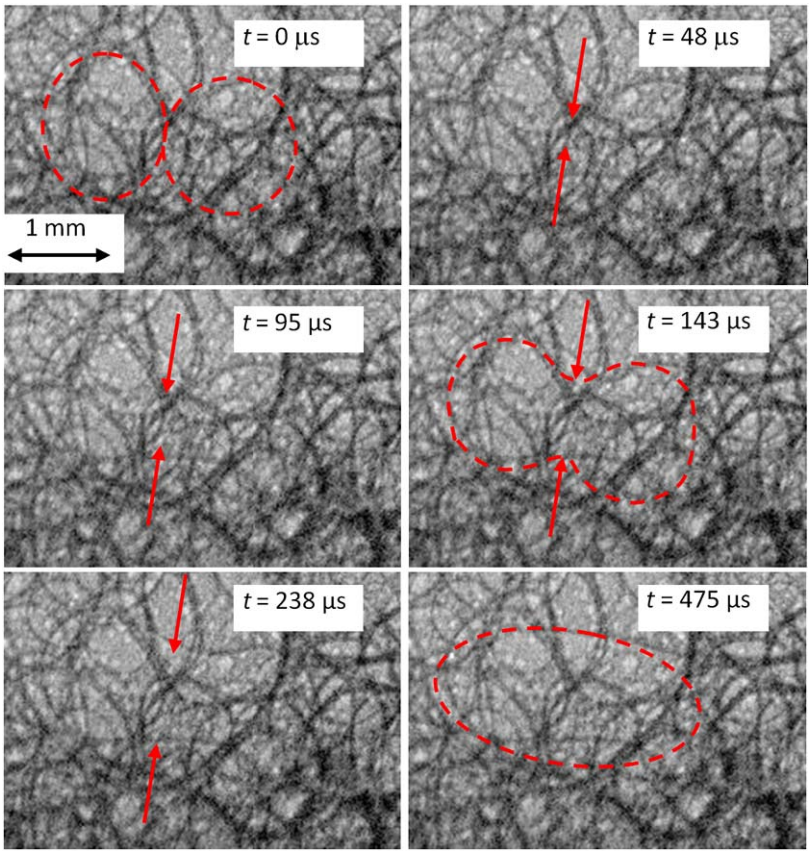

Figure 17. Series of radiographs of an AlSi10 + 0.5wt.% TiH2 foam at 640°C extracted from an in-situ fast synchrotron X-ray radioscopic analysis. The coalescence of two bubbles measured with 9.5µs frame interval (105kfps) can be observed. Dashed lines indicate the contours of the bubbles and arrows indicate the corresponding ruptured cell wall.

In this experiments it was possible to demonstrate that the rupture time of a film is dominated by the inertia of the fluid and not by its viscosity as rupture occurred so fast [71]. Therefore, it could be demonstrated that stabilization by an effective viscosity only, which would be as high as η=0.4Pa·s (as calculated by Gergely et al. [77]) does not apply to metal foams of the type investigated here. Other factors such as bubble size and alloy composition may influence the rupture time and will be studied in future.

4.1.6. In-situ tomography of creep process of brass

The efficiency of electricity-generating plants in general and gas turbines in particular increases with increasing service temperature, therefore requiring components with sufficient high-temperature strength. The lifetime of such components is usually restricted by creep-induced cavity growth leading to unacceptable strains and finally to fracture [52].

Synchrotron radiation microtomography provides new possibilities for a non-destructive determination of creep damage evolution in the bulk of samples, comprising statistical analysis of cavity volume, shape, and orientation evolution during in-situ creep experiments. The results of the experiments enable a quantitative description of the time dependence of cavity morphology and size distributions.

Fast-tomography measurements during creep were performed at ID15A beamline of the ESRF using a high-energy beam (~80 keV) with a large bandwidth (~50%). The acquisition time of a complete tomographic scan was 3 min [78]. The absorption radiographs were recorded with a fast charge-coupled device (CCD) with an effective pixel size of 1.6µm. The tensile creep test was performed in a miniaturized creep machine at constant load developed for in-situ testing [78].

The cavities developed during the creep test were quantified in 3D by fitting an equivalent ellipsoid to each cavity. Figure 18 shows the 3D reconstructions of the sectioned volume revealing creep damage evolution in the sample.

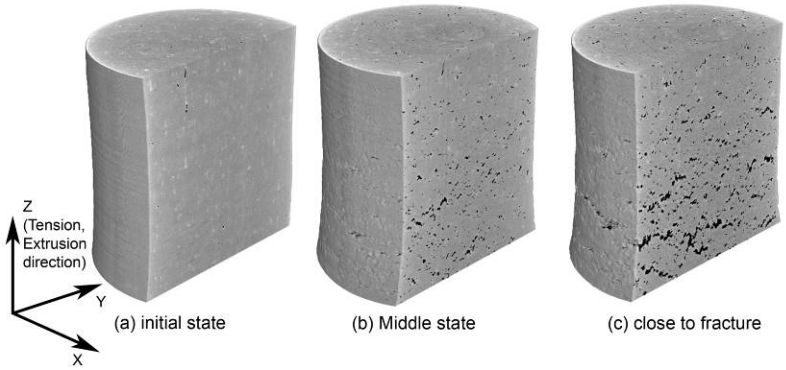

Figure 18. Tomographic volumes revealing the cavities at different times during the creep test. (a) initial condition, (b) middle of the test, (c) close to fracture.

Figure 19 shows the shape evolution of the three largest cavities between the reference state and the final state shortly before fracture. The evolutions are representative for the largest voids, which usually control the final specimen fracture. Void evolutions indicate that creep cavities are relatively small and have nearly ellipsoidal shape in earlier stages of creep. As the material deforms they grow and interactions among neighbors lead to coalescence. These interactions were quite significant for the studied brass alloy. A void can experience several coalescence events during the creep test. The first coalescence was surprisingly detected already in the secondary steady state regime. Not only pair wise coalescences were detected, but also the junctions of triplets and quadruplets.

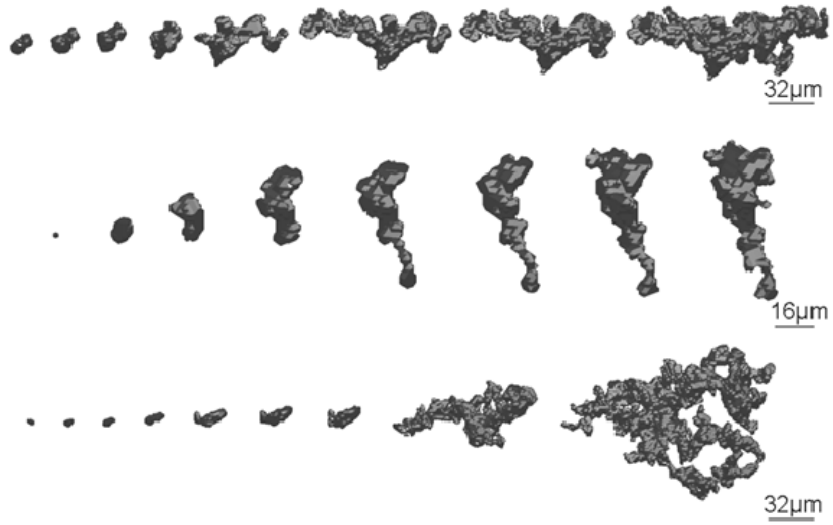

Figure 19. Shape evolution of the three largest cavities exhibiting coalescence.
The different stages correspond to the largest pore before coalescence.

The spatial orientation of a cavity in the present work is characterized by the angle between the major semi-axis of the equivalent ellipsoid and the z-axis (i.e. loading direction). Figure 20 displays a 3D graph of the polar angle of cavities during the creep test for all cavities, revealing a smooth change of the cavity orientation distribution. Such a change in general cavity orientation would indicate the onset of enhanced cavity growth and link-up perpendicular to the stress direction which is essential for damaging during tertiary creep.

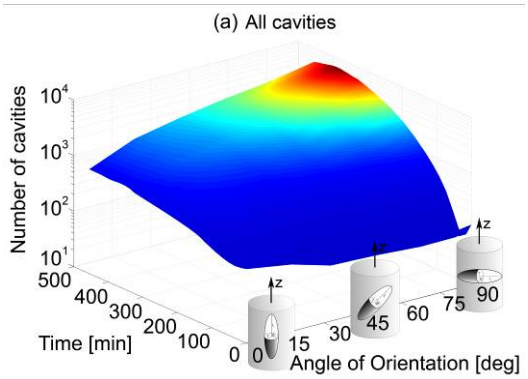

Figure 20. Evolution of the spatial orientation of cavities.

The quantitative analyses performed revealed that the distribution of creep cavities with respect to size, shape, and orientation depends on the time the sample has been exposed to high temperature creep. The largest cavities were formed by coalescence of two or more voids resulting in a complex shape. The cavity population tended to be elongated perpendicularly to the loading direction. The quantitative data obtained can provide a basis for a validation of the description of creep damage by numerical methods.

4.1.7. In-situ tomography of damage development of carbon-fiber reinforced composites

There are many variants of fiber reinforced polymers such as carbon or glass fiber reinforced; straight, woven or 3D braided fiber reinforced; with fibers and particles as reinforce; with hollow fibers or microcapsules for self-healing materials; hybrid carbon and glass, and the list goes on. The amount of variables that might be changed in one material is huge. An example is the ply stacking sequence which determines the failure mechanisms that will be activated upon loading. In particular, carbon fiber reinforced polymers (CFRPs) are widely used in structural components owing to their high specific mechanical properties. However, CFRPs present several failure mechanisms that co-exist in the same laminate and, therefore, improved understanding of damage evolution and eventual failure is still needed.

In-situ SXCT was performed on $[+45/-45/+45]_s$ CFRP subjected to tensile loading. The experiments were performed at the ID15A beamline of the European Synchrotron Radiation Facility. A 14 bit FReLoN (fast readout low noise) CCD camera with a field

of view of 1.2x1.1 mm and an effective pixel size of $(1.4\ mm)^2$ was used. The spatial resolution was about 2 mm (the full width at half maximum of the point spread function). A pink beam with maximum intensity at ~30 keV was used. Six hundred radiographies were recorded between 0º and 180º resulting in a total scan time of 2min per tomogram. Ten scans were recorded at increasingly applied load. A combination of absorption and phase contrast was obtained by placing the sample at ~40 mm from the detector.

The evolution of matrix cracking is shown qualitatively in Figure 21 for different deformation steps. Each individual crack is shown in a different color. The initial cracks grew with the applied load, extending over the whole section of the plies before fracture. Almost all the cracks became interconnected at high loads, so that the majority of the damage displays a single color. None of the pre-existing cracks interacted during deformation with the pores observed in Figure 21 d). The crack fronts and the shape of individual cracks were generally uneven.

The interlaminar crack growth shows a combination of cusp formation and matrix/fibre debonding in front of the crack tip. The cracks are subjected to a mode-II shear loading and cusps develop perpendicular to the principal stress, coincident with the loading direction. As deformation progresses, cusps coalesce and contribute to the propagation of the crack.

The major damage mechanisms and the sequence of occurrences were identified and quantified. The extracted information can be used to validate and enhance damage prediction models.

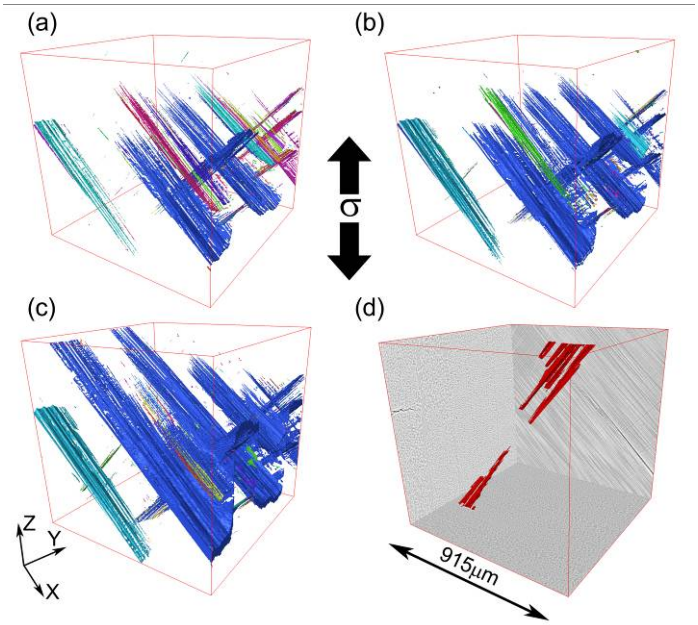

Figure 21. Damage propagation in ±45º plies.

Different crack colours indicate their connectivity (adapted from [17]).

4.2. Material science

4.2.1. Resin microflow by X-ray computed tomography

High performance composites have to be manufactured in autoclave to ensure that they are pore free but this leads to high processing costs and there is a large interest in the optimization of out-of-autoclave processing techniques. Vacuum Assisted Resin Transfer Molding (VARTM) is a very appealing process due to its relative low cost and the possibility to process large panels. In this process, the liquid resin is infiltrated into a plastic bag containing the fiber preform that lay on a rigid mould. The infiltration is assisted by the application of vacuum. However, the resin flow through the fiber fabric is very complex and the key parameters that control the nucleation, growth and coalescence of pores during infusion are not well understood. In addition, the resin flow in the fabric takes place at two different length scales: macroscopic resin flow between the fiber tows progresses rapidly while microflow within the fiber tows occurs at lower speed. The interaction between macroflow and microflow is known to be a critical factor controlling the development of porosity but it is very difficult to analyze experimentally.

To provide the experimental evidence necessary to understand resin flow during VARTM, a miniaturized device that reproduces the conditions of VARTM process was developed and, at the same time, allows to study the infiltration at both scales by means of SXCT. To this end, high resolution SXCT was performed at the fiber scale to analyze in-situ the macro- and micro-flow behavior and the defect formation during the infusion process. The experiments were performed at the P05 beamline of the DESY Synchrotron. A 14 bit CCD camera with a field of view of 3.8x1.9 mm and an effective pixel size of $(1.25\ mm)^2$ was used. The spatial resolution was about 2 mm. A monochromatic beam with 25 keV was used. Nine hundred radiographies were recorded between 0º and 180º resulting in a total scan time of ~2 hs per tomogram. Due to the large measurement time the liquid flow has to be stopped during the measurement. This could be avoided with a fast tomography set-up and would provide real time information about infiltration mechanisms.

Figure 22 shows the experimental set up at the P05 beamline at DESY Synchrotron. The liquid is infiltrated from the top (inlet) and the vacuum is applied at the bottom (outlet). The fiber tow specimen, placed in a vacuum bag inside the PMMA tube was scanned by X-rays during infiltration.

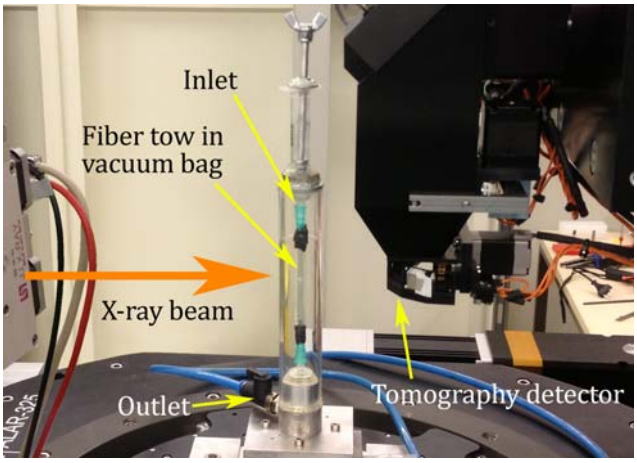

Figure 22. Experimental set up to study in situ the infiltration process at the P05 beamline of DESY Synchrotron.

Figure 23 shows a reconstructed volume and a cross-section obtained by SXCT showing the flow front (macroflow) around the tow and the microflow inside the tow. This unique experimental set up provides the information to analyze the resin

flow in 3-dimensions during infiltration at both the microscale and the macroscale, as well as to assess the differences in permeability between both regimes, being the former several orders of magnitude lower than the latter. Moreover, the experiments shows the conditions that give rise to regions that might remain partially infiltrated due to trapped air bubbles or to differences between capillarity and resin pressure, leading to low quality panels. Based on these data, it is possible to design optimized VARTM strategies to improve the quality and reduce the processing cost of advanced structural composites.

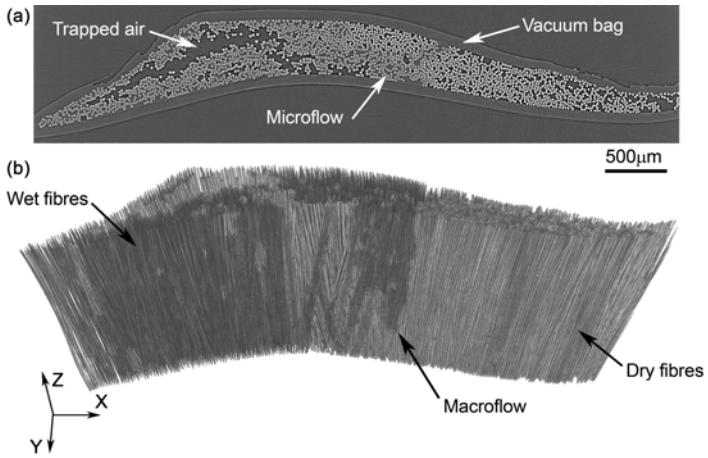

Figure 23. (a) Cross section of the scanned fiber tow specimen in the vacuum bag. Wet glass fibers are surrounded by the lighter grey color. (a) 3D reconstruction of the infiltrated tow.

4.2.2. 3D multiphase networks providing high temperature strength to Al-Si piston alloys

Cast Al-Si alloys are widely used in automotive components such as cylinder heads and pistons. The temperature rise in the combustion chamber of a diesel engine can reach up to ~300-400°C and, therefore, high temperature strength is an important requirement for piston alloys. The high temperature strength of cast Al-Si alloys is provided by a transfer of load from the ductile α-Al matrix to rigid and usually highly interconnected 3D networks of eutectic Si. However, if cast Al-Si alloys are solution treated above 500°C, the eutectic Si rapidly disintegrates and spheroidizes reducing the strength of the alloy [79]. The loss in strength can be reduced by the addition of transition elements such as Ni and Cu that form thermally stable rigid aluminides [80,81]. The reasons for the improvement of mechanical properties of Al-Si alloys by

additions of Ni and Cu are still matter of scientific investigations with important technological implications. The effect of different additions of Ni, Cu and Fe on the high temperature strength of cast Al-Si piston alloys is investigated with respect to the microstructural architecture formed by the aluminides and the eutectic Si. Therefore, absorption and phase contrast synchrotron microtomography was applied to samples of the alloys AlSi12, ASi12Ni, AlSi12Cu5Ni1 and AlSi12Cu5Ni2 in as-cast condition and after solution treatment using the ID19 beamline.

Figure 24 shows the largest particles of the eutectic Si and of the aluminides within the considered volumes for the studied alloys after 4h solution treatment at 490ºC. The tomographic results show that the interconnectivity of the eutectic Si is highly conserved after the solution treatment for the aluminide-containing alloys (Figure 24b, e and f).

Figure 25 shows the evolution of the proof stress, $\sigma_{0.2}$, at 300ºC as a function of the solution treatment time at 490ºC. The solution treatment causes a decrease in the high temperature strength of the investigated alloys within the first 4h.

The aluminide-containing alloys exhibit higher strengths than the AlSi12 alloy due to the larger volume fraction of rigid phases, amounting to 18-24%, the high interconnectivity of the aluminides and their high contiguity with the eutectic Si. The alloys AlSi12Ni1 and AlSi10Cu5Ni1 contain ~8vol.% of aluminides. However, the aluminides in the AlSi10Cu5Ni1 alloy present a higher degree of interconnectivity (~94% in as-cast condition and ~75% after stabilization) than the AlSi12Ni1 alloy (~60% in as-cast condition and ~50% after stabilization). X-ray diffraction analysis revealed that the addition of Cu produces various aluminides increasing the contiguity: Al7Cu4Ni, Al2Cu, Al4Cu2Mg8Si7 and AlSiFeNiCu. ~90% of all the aluminides and all the eutectic Si are forming a highly interconnected rigid 3D structure in AlSi10Cu5Ni1 which increases the high temperature strength by ~100% with respect to the Cu-free alloy AlSi12Ni (Figure 25).

The piston alloys AlSi10Cu5Ni1 and AlSi10Cu5Ni2 show similar strength in the as-cast condition. AlSi10Cu5Ni2 contains more aluminides (~13vol.%) and it retains a ~15% higher strength level than AlSi10Cu5Ni1 after the solution treatment. Furthermore, the 3D network of the rigid phases is practically full preserved (~97%) during solution treatment of the AlSi10Cu5Ni2 (Figure 24d, f), owing to the larger degree of

contiguity between the aluminides and eutectic Si. This results in an extra increase of load transfer from the Al matrix to the reinforcing 3D network of aluminides and Si which is more important at high temperatures where the matrix becomes relatively softer.

The results indicate that the design of cast Al-Si alloys for high temperature applications requires a deep understanding of their 3D architecture and the mechanisms governing its evolution with temperature and time. Synchrotron microtomography is a powerful tool to achieve these tasks mainly due its non-destructive nature, suitable sample-size-to-resolution ratio and the possibility to use phase contrast to reveal the eutectic Si embedded in the Al matrix.

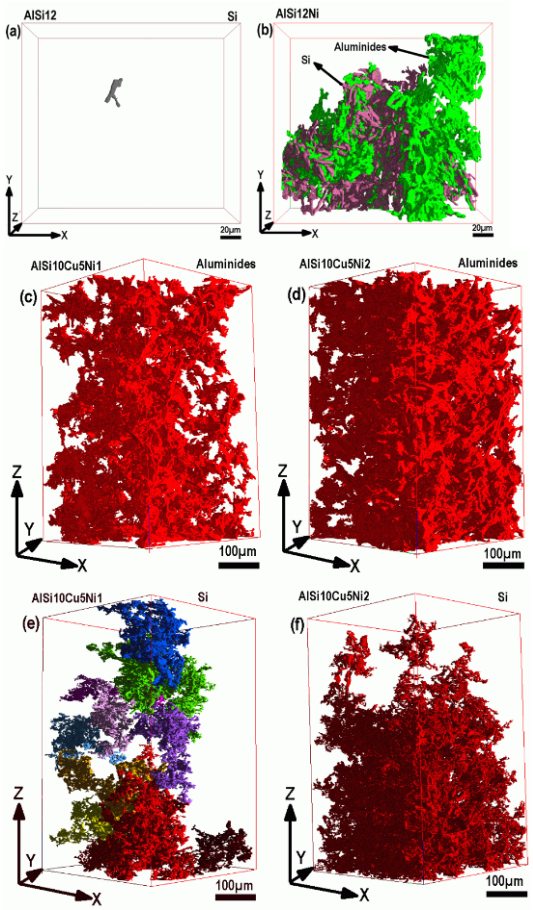

Figure 24. 3D structures of aluminides and Si after 4h of solution treatment: a) Si in AlSi12, b) Si and aluminides in AlSi12Ni, c) aluminides in AlSi10Cu5Ni1, d) aluminides in AlSi12Cu5Ni2, e) Si in AlSi10Cu5Ni1 and f) Si in AlSi10Cu5Ni2.

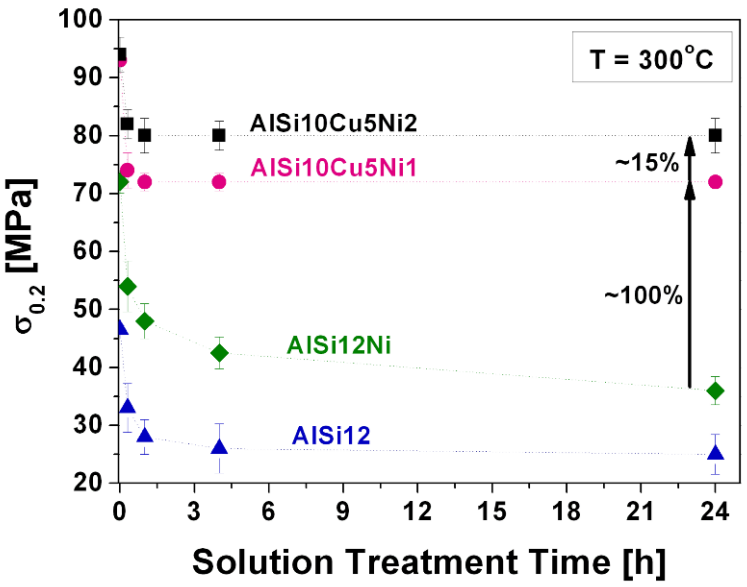

Figure 25. Proof stress $\sigma_{0.2}$ at 300ºC for the investigated alloys as a function of the solution treatment time.

4.2.3. Sub-micrometer holotomography of multiphase metals

The microstructural characterization of multiphase materials by conventional 2D metallography can be insufficient if, for instance, connectivity between phases exists, or the orientation of constituents varies throughout the volume. For this, 3D characterisation tools are needed. Synchrotron microtomography has shown to be a powerful technique to reveal the architecture of materials. Furthermore, the coherence of the beam can be exploited applying quantitative phase contrast tomography or holotomography [82] to image components with similar attenuation. The spatial resolution achievable by parallel beam synchrotron microtomography is about 1 µm. This can be improved using magnifying optics [83]. This has so far been achieved for samples with diameters <100µm using relatively low energies. 3D imaging of engineering alloys requires high energies and representative sample sizes to correlate the properties with the microstructure achieved by the processing method.

Magnified synchrotron holotomography using a Kirkpatrick-Baez (KB) optics system [84] was carried out at the nano-imaging end-station ID22NI for Al- and Ti-alloy samples of 0.4mm diameter. The focal point with a size of 80nm (H) by 130nm (V) and medium monochromaticity (ΔE/E=2x10-2) is produced by a set of multilayer coated crossed bent mirrors. Energies of 17.5keV and 29keV as well as effective pixel

sizes of 60nm and 51nm were used for the Al-alloy and Ti-alloys, respectively. Phase retrieval for holotomography was achieved from recordings at four focal-point-to-sample distances.

Examples of three light alloys are presented. Their microstructures are shown in the scanning electron micrographs (SEM) at the top of Figure 26:

- AlMg7Si4 alloy: the microstructure exhibits a fine ternary eutectic formed by Al, Si and Mg2Si with lamellar structures >150nm. Fe-rich intermetallics (IM) appear within the primary α-Al.
- Ti-10V-2Fe-3Al alloy (Ti1023): the alloy contains ~30% of hcp α phase distributed within bcc β grains not observable by absorption contrast.
- Ti-6Al-4V (Ti64) alloy reinforced with 5vol% TiB needles (Ti64/TiB/5w): the Ti64 alloy matrix consists of α grains separated by narrow β zones and TiB needles.

Holotomography is well adapted to these materials as there is low absorption contrast between the present phases.

Portions of the reconstructed holotomography slices are shown at the bottom of Figure 26. The grey level scales linearly with the electron density of the constituents revealing all the phases observed in the SEM micrographs. Volume views of the minority phases are shown in Figure 27.

- AlMg7Si4: the ternary eutectic with interconnected Si-Mg2Si structures as thin as ~180 nm (green) are identified. The IM particles and α-Al are made transparent in Figure 27a).
- Ti1023: α grains >200nm are identified. In Figure 27b), an interconnected structure of α particles remained from an incomplete break-up of the lamellar structure during pre-forging (blue), while secondary α grains (green) are embedded in the β phase.
- Ti64/TiB/5w: the α and β phases in the Ti64 matrix are identified down to 200nm. In Figure 27c), TiB needles (green) are connected to irregularly shaped β grains (other colours), forming an interpenetrating structure within the α phase.

Magnified synchrotron holotomography using KB optics was used to characterize the 3D-architecture of Al- and Ti-alloy samples of ~0.4mm diameter with energies of 17.5 and 29keV, respectively. Using the nano-focusing KB-system for such a high energy (29keV) is reported for the first time. This experimental setup combining

synchrotron radiation, KB optics and holotomography opens a new level of resolution (≥180nm) for non-destructive 3D imaging of representative samples of multiphase metals.

Although magnified synchrotron holotomography is not planned in the proposed beamline, the holotomography methodology can be used to characterize multiphase materials as long as the size of the phase are above the resolution of the technique. However, the magnifying optics set up could be included in a further update of the beamline.

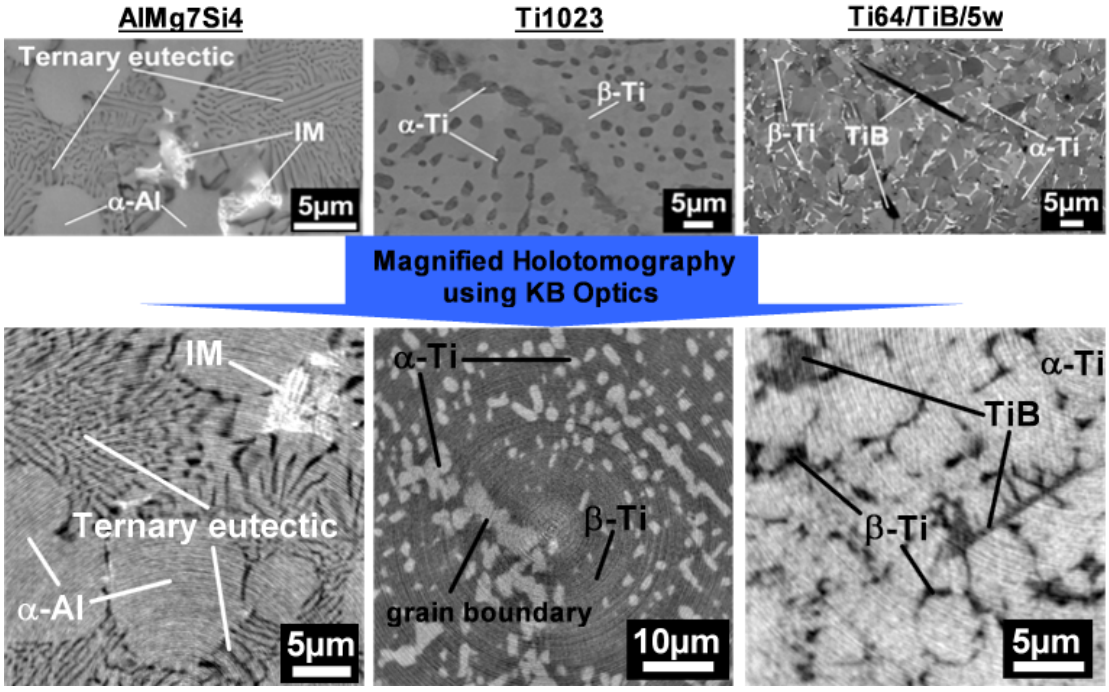

Figure 26. Top: scanning electron micrographs of the investigated materials Bottom: portions of slices of holotomography reconstructions of the investigated materials. From left to right: AlMg7Si4 alloy, Ti1023 alloy and Ti64/TiB/5w.

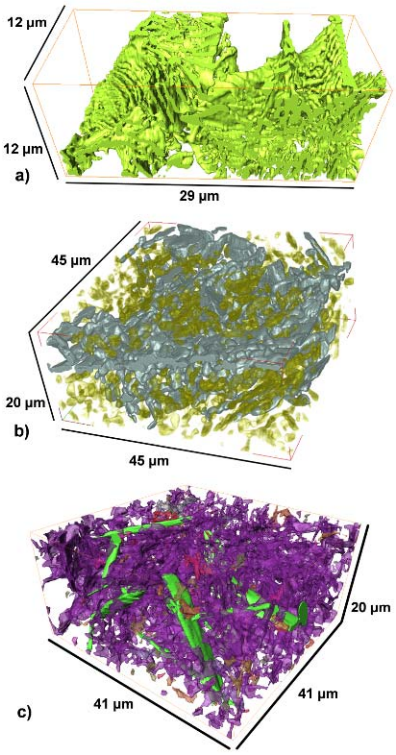

Figure 27. Rendered volumes of the investigated materials: a) interconnected Si-Mg_2Si structure (green) in AlMg7Si4; b) larger α particles remaining from pre-forging (blue) and individual secondary α grains (semi-transparent green) in Ti1023; c) TiB needles (green) and irregularly shaped β grains in Ti64/TiB/5w (other colours).

4.3. Life sciences and biomedicine

In contemporary biomedical, as well as clinical research, structural imaging has a central role. Current approaches are focused in a multiscale methodology. Synchrotron X-ray based imaging provide the possibility to integrate several of the required length scale, providing high-resolution (sub-micrometre) detail in large samples (tens of centimetres) [85]. SXCT with phase-contrast offers exciting possibilities to support Systems Medicine research. Substructures of organs, or even whole (small) organisms, can be investigated, segmented and quantified from a single 3D dataset. This also enables to obtain the structural data that is required for e.g. performing computational modelling of functional organ [86], such as it is done in the context of the Virtual Physiological Human [87].

Potential applications for a hard X-ray tomography beamline at ALBA:

4.3.1. High resolution Structural Imaging of static tissue:

Multi-resolution imaging at the (sub-) micrometre scale is essential in evaluating structural properties and induced changes in a lot of biomedical domains. The ability to image large volumes of tissue at this scale offers novel insights towards assessing pathological remodeling as well as towards providing data for e.g. computational modeling. Examples of this are provided in Figure 28, Figure 29, Figure 30.

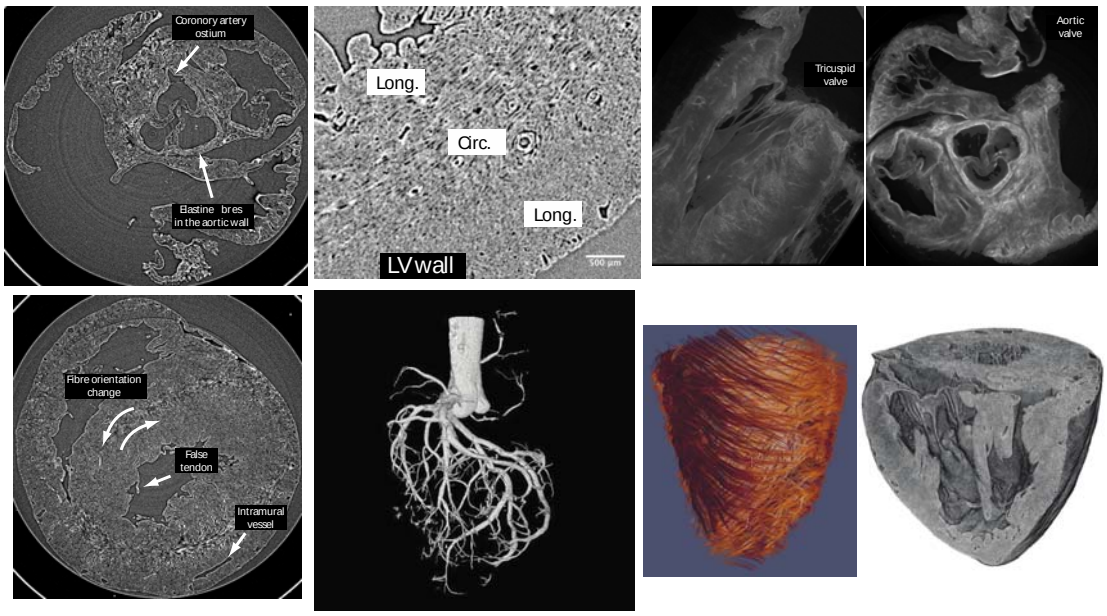

Figure 28. Phase-contrast imaging of whole (rodent) hearts. Beside the anatomical detail at organ level, the detailed fibre structure in which myocytes are organised can easily be assessed. Additionally, vessels can be observed and extracted using computational tools [89].

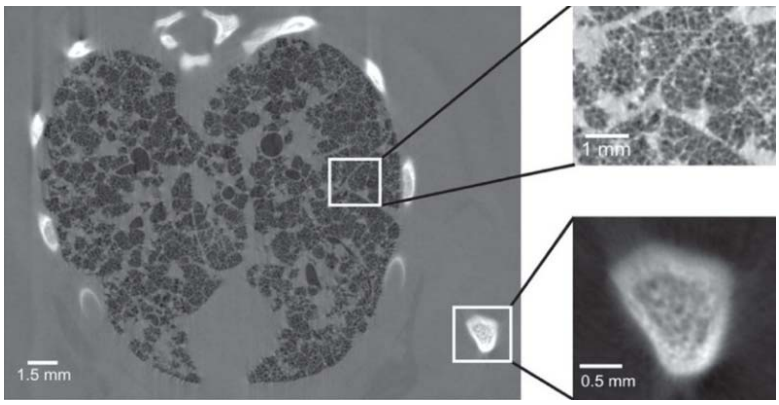

Figure 29. Image of a preterm rabbit pup thorax, focusing on the air/lung tissue interface [90].

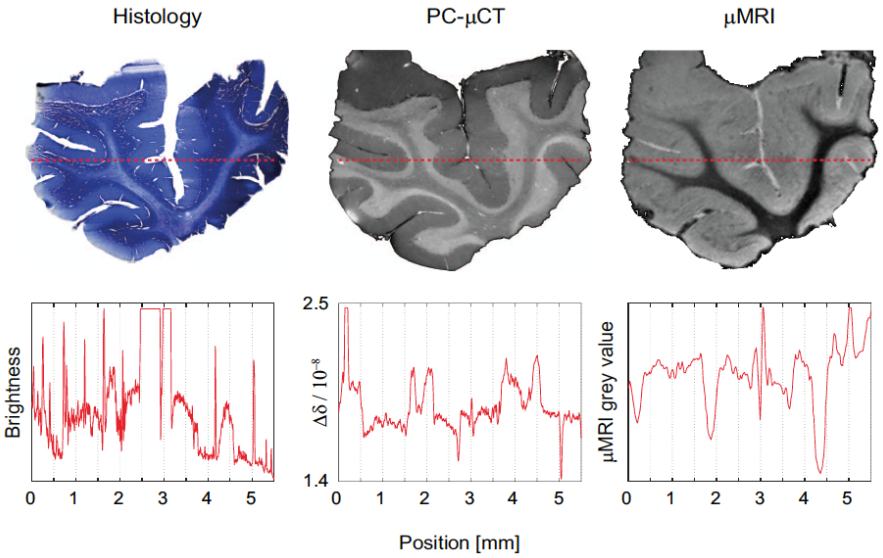

Figure 30. Spatial resolution of histology, X-ray phase tomography, and MRI microscopy demonstrating that resolution decreases from histology via PC-mCT to mMRI [91].

4.3.2. High throughput Virtual Pathology

Whole organism assessment, as e.g. in human autopsies or phenotyping of genetically modified model organisms, is still an essential source of information, both in basic research as well as in clinical understanding of diseases. Traditional autopsies would describe and, in some cases image, the whole organism and additional detailed information would be provided from destructive (microscopy) investigation of specific organs or tissue samples. However, this leads to different (sparse) information at the different spatial resolutions and an integration of organ and cell-aggregate level is extremely challenging, very time consuming and expensive. This means that whole organisms are only investigated in rare cases, such as for specific research projects or e.g. in human fetuses when the cause of perinatal death is unknown. Other methods like MRI are very time consuming and with limited resolution, Figure 31. SXCT in phase

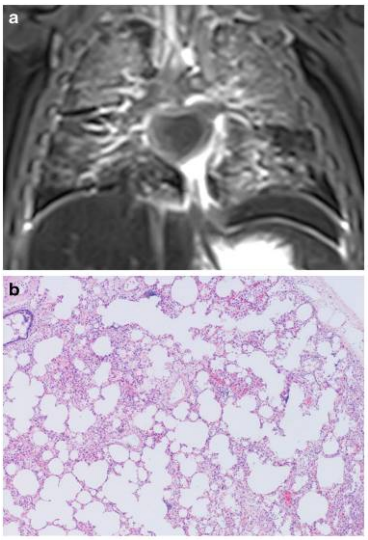

Figure 31. A false positive MRI post mortem, suggesting lung changes while histology was normal.

contrast mode, together with a high throughput for sample handling, could provide a way for fast (<1h) and high resolution (<1 micrometre) imaging of both model organisms and human fetuses samples. Additionally, the high resolution integrated datasets would provide a novel opportunity to collect a series of pathological specimen and make them digitally available to the research and clinical community, both for supporting innovative research as well as for teaching purposes.

4.3.3. High speed dynamic imaging of functional organs

While structural imaging is of great importance to understand disease processes, the functional and thus dynamic component is crucial for an integrated Systems Medicine approach. While techniques such as fluorescence imaging can provide molecular dynamics, structural changes during time (either temporal evolution/development or temporal dynamics during functional cycles), especially at multi-scale resolution, are very challenging. Phase-contrast micro-tomography and radiography with a possibility for high speed and continuous imaging offers novel potential for e.g. imaging the changes/realignment in cardiac fibers during the contractile cycle, or the maturation of the lungs in the first seconds/minutes after birth (Figure 32).

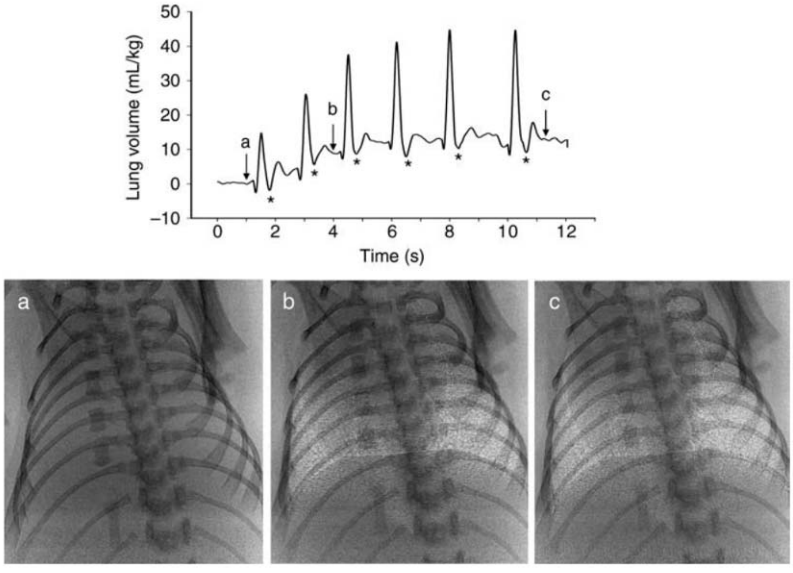

Figure 32. Breathing activity and the increase in end-expiratory lung gas volumes from birth in a spontaneously breathing newborn rabbit pup. Phase contrast X-ray images were acquired at the times indicated by the arrows demonstrate the increase in lung aeration [94].

4.4. Historical building

4.4.1. In-situ tomography of the fluid movement inside rocks: application to historical building conservation

Water plays a fundamental role in rock weathering processes. Its penetration and movement inside rocks greatly influences the nature and intensity of the damage. X-ray Computed Tomography (X-ray CT) being a Non Destructive Technique (NDT), is very useful in mapping water penetration. A General Electric HiVelocity QX/i helicoidal scanner was used for the studies in the following parameters: voltage 140kV; current 150mA; exposure time 2s; resolution 0.203 mm x 0.203 mm, and slice width 0.625 mm. Series of 80 virtual sections were imaged in parallel at specified time intervals. The obtained images were 512 x 512pixels in size. Image length: 50mm.

X-ray CT provides good images of the internal structure of the samples: the sedimentary layering due to differences in composition and porosity is clearly seen as well as other mineralogical/textural characteristics (Figure 33).

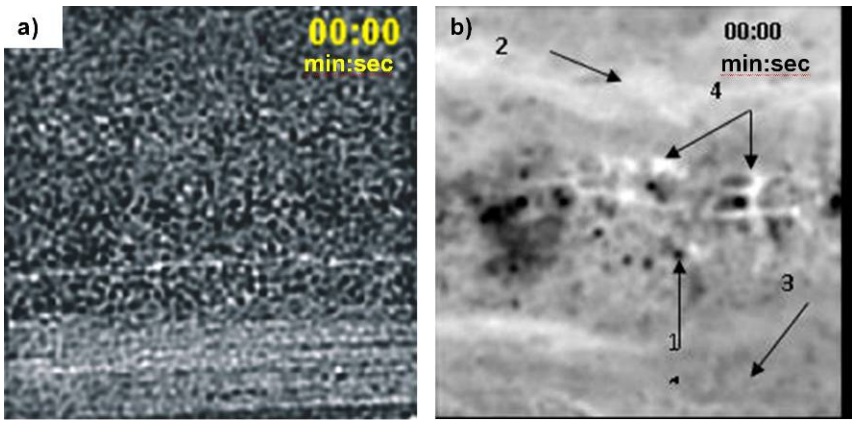

Figure 33. a) Uniform distribution of the minerals except in iron oxides layers (at the bottom). b) (1) void spaces; (2) fine-grained carbonates; (3) large-grained carbonates and (4) clays and iron minerals.

The movement and penetration rate of water has been monitored by X-ray CT during free water absorption tests (UNE-EN 13755 (2002). Figure 34a) shows the difference between dry and wet zones in the interior of the sample while Figure 34b) shows a 3D rendering of the volume illustrating how the dry open space decreases during the absorption test.

The comparison of 80 CT scans periodically taken during the water absorption test allows the observation of the water front movement in 3D. The water movement is related to the petrographic characteristics of the rock, mainly to the sedimentary layering that controls the direction of water penetration. Water absorption depends on the rock texture and porosity. Large pores are generally not connected. Water penetrates through the layers with smaller but interconnected pores.

Hounsfield Unit numbers provide a quantitative approach for the identification of different compositions and porosities, and the penetration rate of water. Mean CT values in Hounsfield units (HU), in ROI´s (Region Of Interest) are measured at different intervals of time during the water absorption test (ROI volume 2x2x0,625mm), see Figure 35.

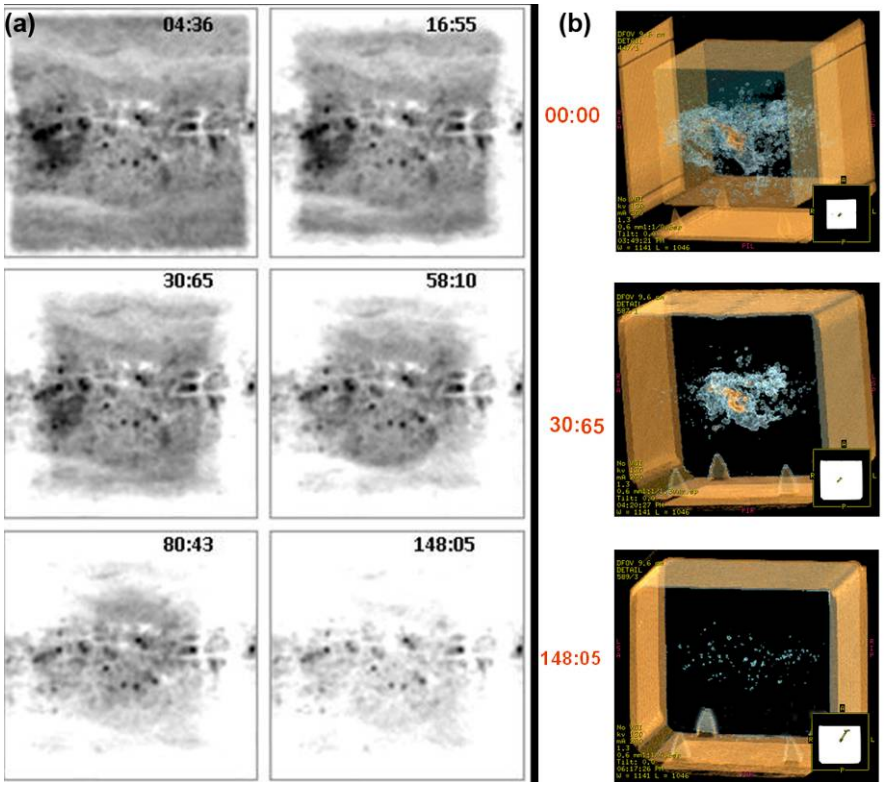

Figure 34. a) CT images showing the variation in water penetration. b) 3D images of the open porosity.

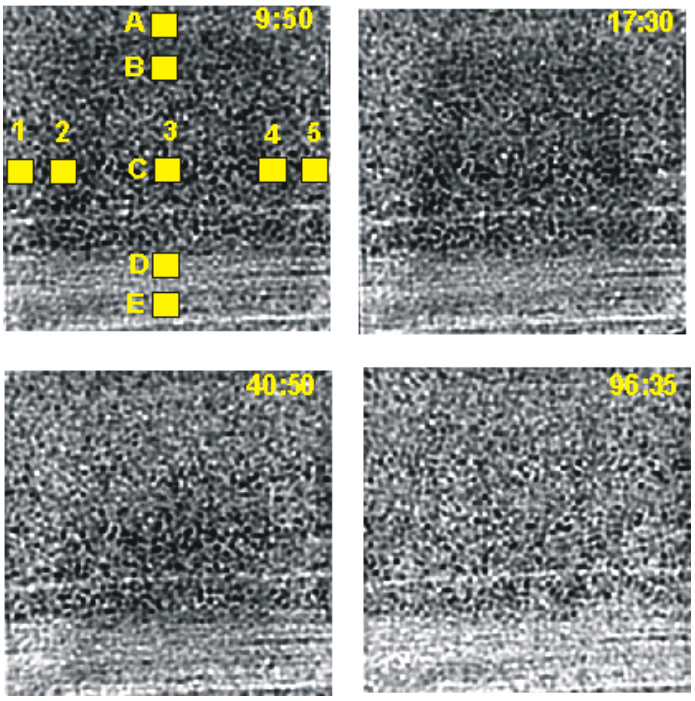

Figure 35. CT images at different times during the absorption test.

The positions of nine ROI´s used to quantify the water penetration rate are indicated.

Water penetrates from all the external faces of the sample. After approximately 10 minutes from the beginning of the test, the wet zone is not very thick. Even after 17min the water penetrates only about 1cm inside the sample and after 40min the water reaches the inner part of the sample. The sample is saturated only after 96min.

The textural characteristics influence the water penetration. The rate is higher in the direction parallel to the lamination as can be seen in the image taken after 17min. The penetration rate through the lateral faces is not uniform and the wet lateral zones are thicker in the zone more distant from the opaque minerals layer. The water penetration in certain ROIs can be estimated using the evolution of the ROI mean CT number. Figure 36 shows the periods of water absorption, water saturation and water arrival.

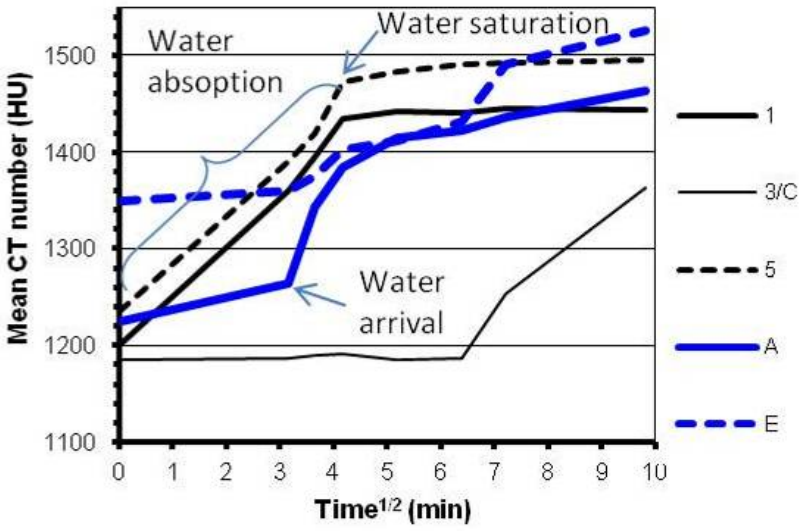

Figure 36. Evolution of the mean CT number of the internal ROI´s.

Although this study was been carried out with laboratory CT, the use of the synchrotron radiation would provide a substantial improvement in the image quality and spatial resolution. Synchrotron XCT is a very appealing technique for studies in fine- and very fine-grained rocks where the relationship between porosity characteristics (pore size, connectivity, tortuosity of the pore channels, etc), the penetration of consolidant and water-repellent products, and the movement of water inside the rock materials is important. Also, the possibility to obtain a better spatial resolution would opens up new opportunities to study the fluid dynamics in the rocks.

4.5. Biology

4.5.1. Investigating the continuous dental replacement of mammals through a new rodent model

Continuous dental replacement is an exceptional mechanism in mammals because they usually have only two generations of teeth, contrary to their reptilian ancestors. In continuous dental replacement there is constant addition of teeth at the rear of the jaw. Up to now, this characteristic has been only found in the pygmy rock-wallaby and in manatees, and it remains barely documented. However, it was recently discovered an African mole-rat displaying unusual dentition, which reopens

the debate concerning tooth replacement and the origin of supernumerary teeth in mammals.

The silvery mole-rat (Heliophobius argenteocinereus) is a solitary African rodent that spends most of its lifetime digging burrows in order to find food (Figure 37a). Occurrence of only a few supernumerary teeth has already been mentioned for this rodent, but continuous dental replacement had never been proposed, nor investigated. By means of the X-ray synchrotron microtomography, using beamlines ID19 and BM05 (at 25 keV, cubic voxel of 5.06 µm), the dental characteristics of this African mole-rat were accurately imaged to highlight the various properties of its dental replacement mechanism. Among 55 investigated skulls of H. argenteocinereus, one juvenile and one adult were chosen to be scanned. Comparisons have also been drawn with the dentitions of manatees and the pygmy rock-wallaby. The dental characteristics of the wallaby have also been investigated using beamline ID19 (at 60 keV, cubic voxel of 7.46 µm).

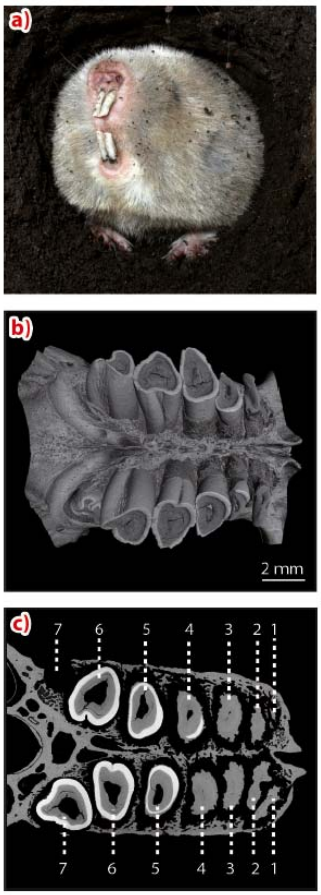

Figure 37. a) Foreside of a captive silvery mole-rat, b) 3D reconstruction and c) Virtual cross-section of the upper dentition of an adult silvery mole-rat.

While the molar number never exceeds three in placental mammals, the silvery mole-rat can bear up to seven molars (Figure 37b-c). Indeed, the molars of this rodent are continuously replaced, since new teeth regularly erupt at the rear of the jaw, pushing the anterior teeth, which become extremely worn, and finally resorbed inside the bone (Figure 37c). The very high quality and precision of synchrotron reconstructions permitted us to visualise the resorption of both root and crown (Figure 38a), which is led by the compressive action of erupting molars on anterior molars. The originality of this dentition also relies on its high-crowned teeth. As a result, the occurrence of continuous dental replacement coupled to high-crowned teeth constitutes an excellent “escalator-like” dental mechanism (Figure 38b),

necessary to withstand the effects of severe wear on teeth. This solitary rodent actively digs with its incisors irrespective of the hardness of the soil, therefore, we hypothesised that high wear of the molars could be linked to severe dental friction occurring during both digging and feeding.

What do the comparisons with other mammals having continuous dental replacement reveal? Manatees and the small wallaby display low-crowned teeth contrary to this mole-rat. Moreover, their dental resorption is only efficient for the roots of their teeth. Synchrotron reconstruction of the wallaby's dentition also allowed us to clearly show that the anterior molars are not totally resorbed (Figure 38c), but rather they are shed when they reach the front of the jaw. Even if the mechanism is convergent with the rodent's dental system, it still reminds one of a "treadmill" (Figure 38d), and is clearly optimised for gnawing abrasive plants. Apart from these differences, we found that the three mammals and some of their extinct and extant relatives shared some biological traits essential for continuous dental replacement. They comprise a forward movement of new teeth from the rear to the front of the jaw (mesial drift), the continued eruption of teeth after the age of sexual maturity (delayed eruption), and the growth of extra teeth (supernumerary teeth).

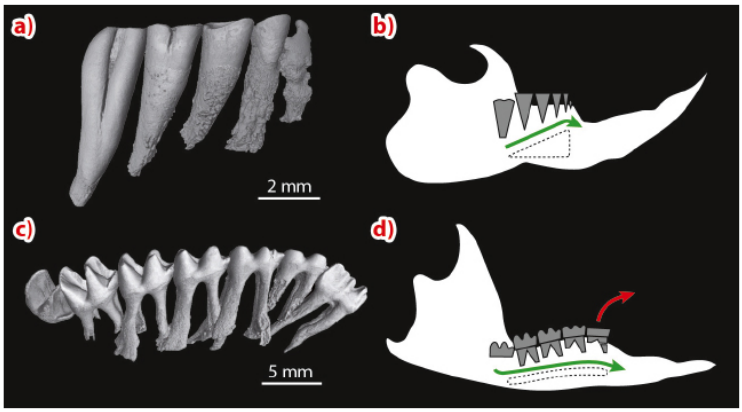

Figure 38. a) 3D reconstruction in lateral view of a lower tooth row and b) model of dental replacement of the silvery mole-rat. c) 3D reconstruction in lateral view of a lower tooth row and d) model of dental replacement of the pygmy rock-wallaby (green arrows: molar progression; red arrow: tooth loss).

What is the main biological interest of this rodent? Manatees and the pygmy rock wallaby are not suitable for an accurate study of continuous dental replacement, because of their size and their endangered status.

Mice, the usual biological model, do not have any of the dental characteristics previously detailed. Consequently, this mole-rat could be the better biological model for an extensive study of the continuous dental replacement's underlying mechanism, which could represent a basis to understand the developmental and molecular processes leading to additional molars. Further research on this topic will be of high interest, notably regarding the knowledge of dental stem cells in relation to the origin of extra teeth in mammals, and thus leading to the eventual goal of the regeneration of dental tissue in humans [95].

4.6. Paleontology (foraminifera tomcat)

4.6.1. Morphological characterization of fossils

Due to the non-destructive-nature of X-ray micro-CT, rare and valuable artifacts can be examined in 3D. A wide range of fossils are covered in the literature [96], some examples are fossilized embryos [97], jawless fish [98], animals that have been preserved in amber (spiders, beetles, pseudoscorpions, earwigs) [99-103]. As an example, Figure 39 shows a high resolution detail (reconstructed voxel size 0.6673 μm^3) of the right chelal fingers of a Pseudogarypus synchrotron [103] fossil trapped in amber imaged using propagation-based phase contrast synchrotron micro-CT.

Figure 39. Right chelal fingers of a Pseudogarypus synchrotron [103] fossil trapped in amber

SXCT allows the three-dimensional imaging and bio-metric quantification of fossils at sub-micron resolutions, like foraminiferal interiors. This technique opens a new era in fundamental biometric-evolutionary research. It can provide a means of morphologic evaluation of phylogenies based on molecular data [104]. Eventually, the accuracy of palaeoceanographic and palaeoclimatic reconstructions could also benefit from the possibility of morphological differentiation between cryptic planktonic species [105].

5. BEAMLINE CONCEPT, LAYOUT AND REQUIREMENTS

5.1. Technical requirements

In congruence with the scope of this proposal the technical requirements for the beamline are summarized in Table 3. These requirements will be fulfilled thanks to the careful selection of the components described in the next sections (insertion device and optics, end-station and detection systems, sample environment, etc). Although not included in the current project proposal we have also considered the natural evolution of the instrument and therefore everything has been sketched in such a manner that it would be possible to install additional components and develop new tomographic techniques.

Table 3. Technical requirements for the proposed beamline

Technical requirement	Expected value
Energy range	10-55keV
Min Flux	$7x10^{12}$ photon/s/mm at 50keV and 0.1%BW
Max Flux	10^{18} photon/s/mm in white beam
Beam type	White beam Monochromatic beam (2-3% bandwidth) Monochromatic beam (0.1% bandwidth)*
Max spatial resolution	Better than 1 micron
Max. FOV	30x12mm
Max temporal resolution	Better than 1ms/image
Available techniques	Absorption Tomography Phase contrast tomography Holotomography Absorption-edge Tomography Fast tomography & radioscopy Nanotomography*

*Projected in future development of the instrument

5.2. Source

The imaging beamline requires a small source to target 1-0.5μm spatial resolution and quite large divergence, with high flux in the range between 30 and 50 keV. This energy range is 4 to 6 times larger than the critical energy of the Alba bending magnets. Thus, in order to provide optimal flux at that energy range, alternative sources have been explored.

The immediate alternative would be replacing one of the Alba bending magnets by a super-bending magnet, with higher dipolar field. However, this would have considerable impact on the performance of the accelerator. Alternatively, we propose using a wavelength shifter. This is an insertion device, which produces a single bump in the trajectory of the electrons. The peak magnetic field of the wavelength shifter is much larger than the dipole, and allows reaching higher photon energies.

As an additional improvement, the lattice of the storage ring of ALBA would be modified to create a mini-beta section at the straight section corresponding to the imaging beamline. With this section it is possible to achieve smaller source size as it required to reach the desired spatial resolution. The Initial proposal for wavelength shifter is a hybrid in-vacuum design, with permanent magnets made of NdFeB. The minimum gap considered for this design is 8 mm, and the maximum peak field 2.75 T in the center. The magnetic length of the insertion device is 400 mm, and the occupied space in the straight section taking into account the tapers for the vacuum chamber will be ca. 800 mm.

5.2.1. Source properties

In the case of a wavelength shifter, it is needed to compute the phase space distribution in order to determine the size and divergence of the photon source. It is shown in Figure 40 for photon energy of 20 keV. One can see that the radiation fan fills up to 6 mrad, although at the extremes, it gets wider in the spatial dimension. This means that the actual source size and shape, seen by the beamline, depends on the horizontal acceptance of the front-end, giving as a result a larger source for larger acceptances.

In order to fill 30 mm (horizontal) at the sample position, assuming that it can be as far as 30 m from the source, it is necessary to collect 1 mrad of the horizontal emission fan. It would be possible to collect a wider horizontal angle of the radiation which would allow for a larger horizontal illumination field at the sample position although it would decrease the resolution, as the apparent source size would be larger.

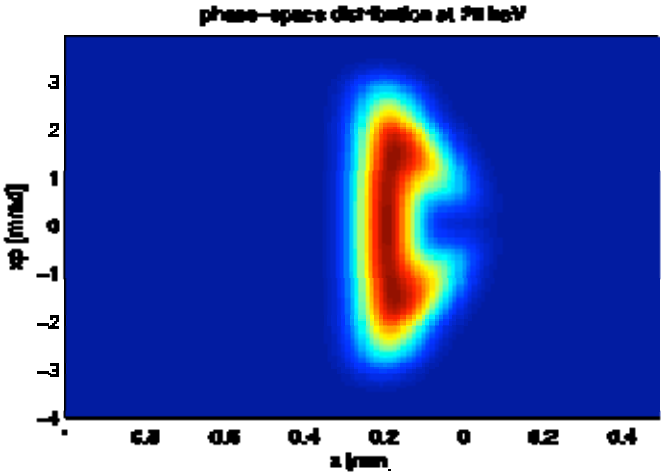

Figure 40. Horizontal phase space distribution of the WS400 source.

The source size corresponding to 1 mrad horizontal acceptance is given in Figure 41 and Figure 42. One can see that for low energies it presents a parasitic side lobe, resulting from the structure of the wavelength shifter. Such side lobe disappears for higher energies which is convenient as the BL working energies would be in the range of 20-50 keV.

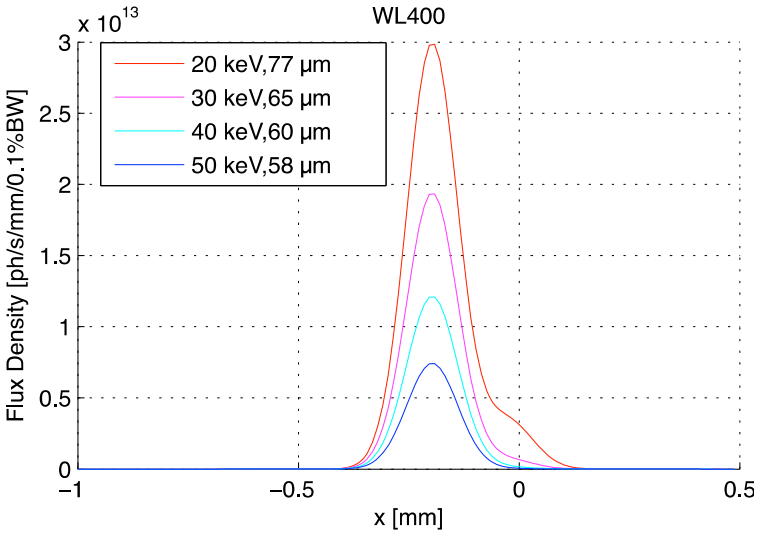

Figure 41. Horizontal spatial flux distribution of the source for 4 photon energies, for low energies a parasitic side-lobe appears.

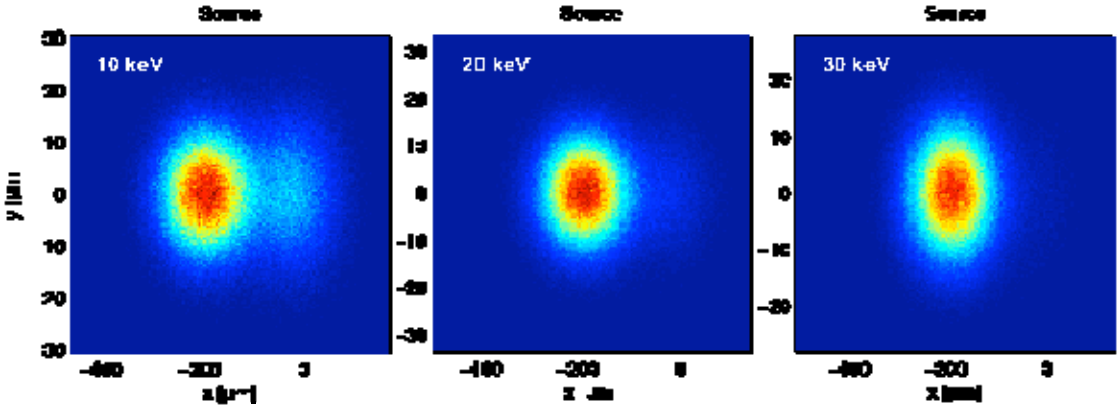

Figure 42. Photon source distribution for (vertical and horizontal) for three photon energies.

The flux integrated in 1 mrad is given in Figure 43, compared to the source of a bending magnet. One can see that much higher flux, up to much higher photon energies can be reached.

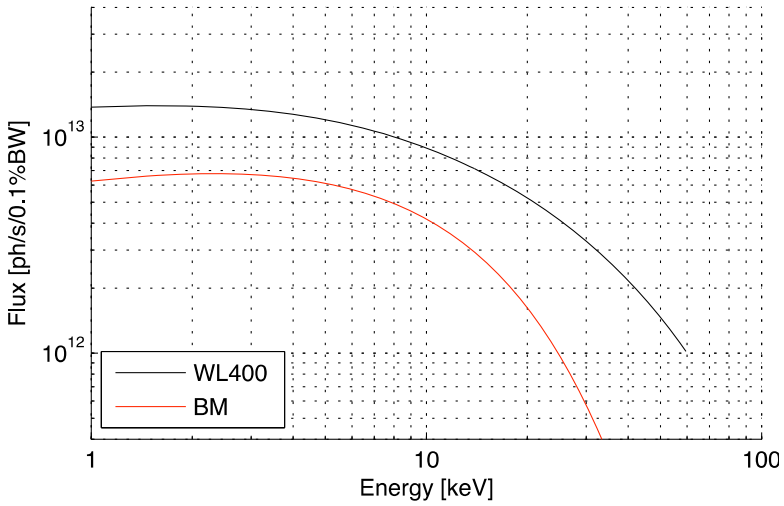

Figure 43. Flux emitted within a horizontal acceptance of 1 mrad, for the proposed source compared to a bending magnet.

5.3. Multilayer and Si(111) monochromators

A combined monochromator has also been considered for the beamline. It will have a pair of Si (111) crystals, which will provide high spectral resolution, as well as a pair of multilayer mirrors, which will provide the required high flux. The double multilayer mirror is considered to have a higher user demand than the Si (111).

In order to provide large acceptance with reasonable size optics, the first and second mirrors are mounted on independent Bragg rotation stages. The second one can be

also displaced along the beam. The corresponding Bragg angles are given in Figure 44. There, we consider a bilayer thickness of 4 nm.

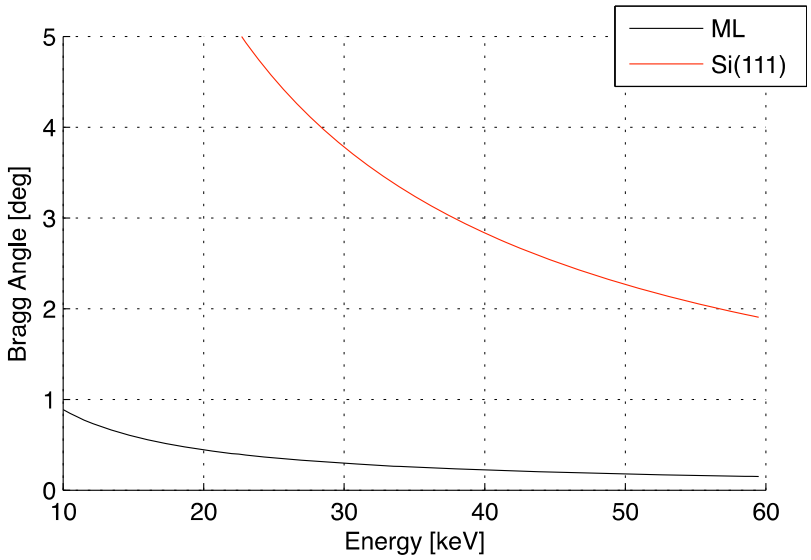

Figure 44. Bragg angle for a 4 nm multilayer monochromator, and for a Si(111) crystal pair.

Given the limited length of the multilayer mirrors, the monochromator has a limited vertical acceptance, mainly for high energies, since their corresponding Bragg angle is very grazing. This limits the vertical size of the illuminated area at the sample plane (considering it is at 35 m from the source). In order to minimize this effect, we propose installing the monochromator inside the tunnel. A comparison between two possible monochromator positions is given in Figure 42. It represents the projection onto the sample plane of the monochromator acceptance, in red and magenta for the monochromator inside (11.5m) and outside (18m) the tunnel, respectively. They are compared to the beam size (fwhm) as emitted by the source, without any aperture limitation (black line). It is possible to appreciate that a larger illuminated area can be reached for energies above 18 keV if the monochromator is installed inside the tunnel, being up to a 50% larger at 40 keV.

The incidence angles for the Si (111) crystals are much higher, and an unlimited vertical spot size can be achieved with 200 mm long crystals.

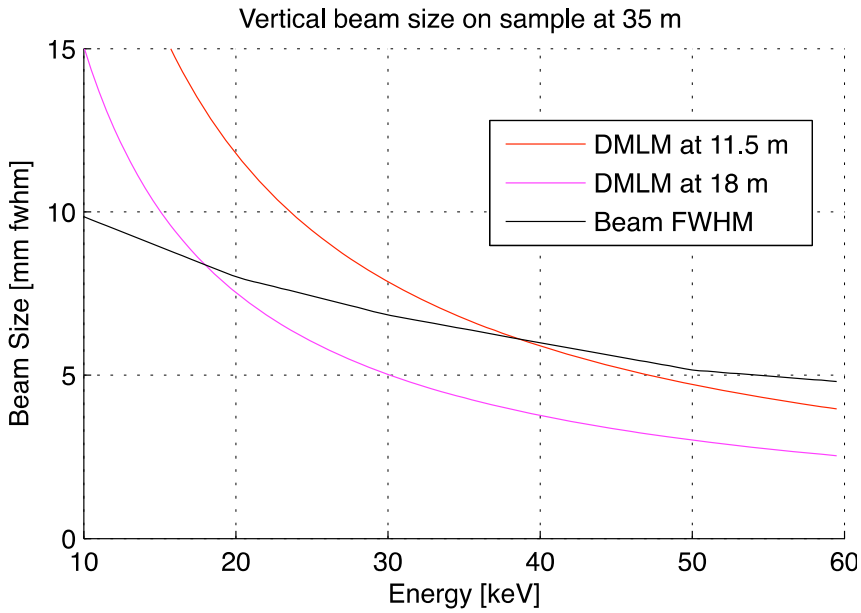

Figure 45. Vertical size of the illuminated area (Double Multilayer Monochromator = DMLM).

Examples of the beam 35 m downstream the source are given in Figure 46 for the Double Multilayer Monochromator (DMLM) at 11.5m. Note how at 20 keV the full beam is accepted, while it is partially shorten in vertical direction for 40 keV. The horizontal striations that appear on the beam are a consequence of the slope error (0.5µrad rms) considered in the simulations although they do not represent a problem for imaging purposes.

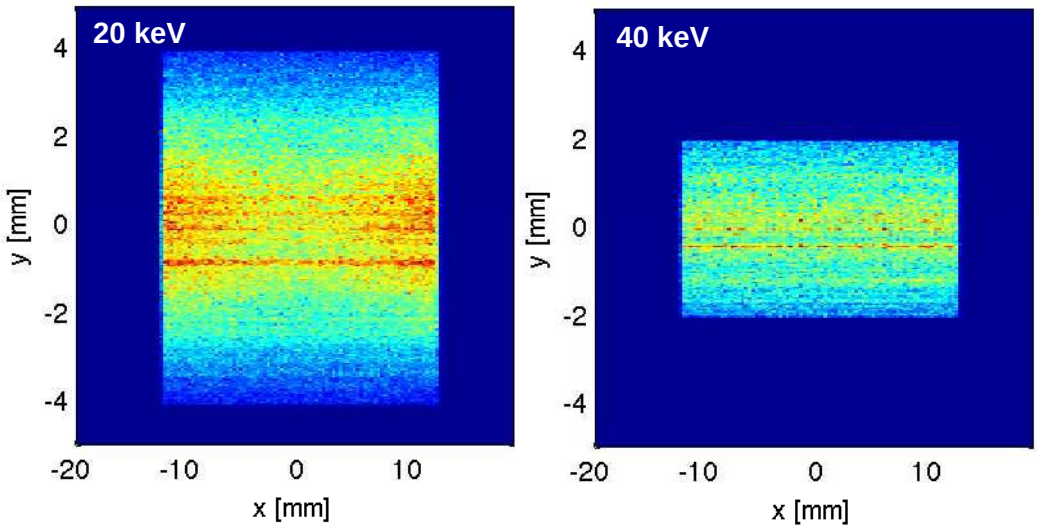

Figure 46. Sample illumination area for two different values of the energy.

The stripes are caused by the slope error of the multilayer (ML) mirrors.

Detailed FEA is required to analyze the power load on the monochromator crystals. In addition to the use of a monochromatic beam, white beam experiments are also

required at this BL. The height difference from the monochromatic beam using Si(111) or multilayer as well as from monochromatic to white beam at the sample position (35m) will be compensated at the end-station position.

5.4. Beamline layout

Since one of the main goals of the beamline is to provide a rather large illumination area at the sample position, a rather simple layout is proposed. The main optical component is a double crystal and double multilayer monochromator. In addition, some slits and filters, as well as diagnostic units and vacuum protection windows, are included. A scheme of the proposed layout is given in Figure 47.

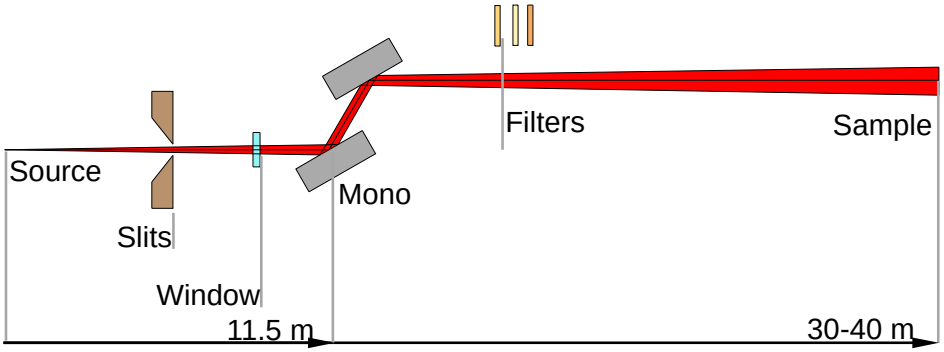

Figure 47. Schematic optical layout of the imaging beamline.

A proposed layout of the beamline according to the Alba Experimental Hall (EH) dimensions is given in Figure 48. Inside the tunnel, the monochromator is installed downstream together with some of the Front-End (FE) components. These are: a fixed mask, an X-ray Beam Position Monitor (xBPM), a photon shutter and a set of movable masks. The installation of these components takes about 3.5 m along the beam path. After these components, a diamond window separates the vacuum of the machine from the beamline. The monochromator is placed downstream the mask. It includes the trigger gauges for the fast closing valve of the front end. Finally, downstream the monochromator, there is a double bremsstrahlung shutter (BS shutter), as the last optical element considered within the tunnel. Additionally filters made of different elements (carbon –graphite-, aluminium, copper, iron) and different thicknesses will be available in this part of the tunnel.

The optical hutch does not need a large space since it hosts just a set of transmission filters, a diagnostics set, and a photon shutter, as the main components. The beam is

transported from the optics to the experimental hutch by a simple radiation shielded vacuum pipe with a second CVD diamond window at its end. This pipe has been designed to be adjustable in length so the beam is transported in vacuum to a short distance to the sample. The experimental hutch has been designed to be 10 m long and allows setting the sample between 30 and 40 m from the source.

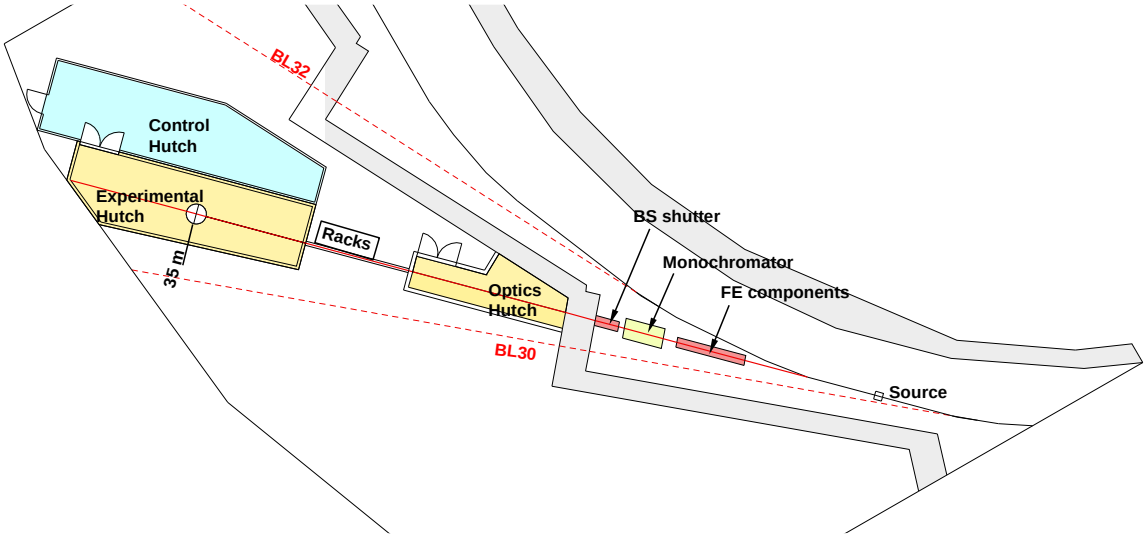

Figure 48. Layout of the Imaging beamline at the ALBA Experimental Hall.

5.5. Experimental end-station and detection systems

The experimental end-station consists in a set of components that basically allow sample positioning and imaging. These components are described in the following subsections.

5.5.1. Sample positioning system:

The positioning system is composed by different motorized stages mounted over a large optical table with wheels (2.3x1.5m) that will be displaced over a pair of rails in the beam direction. The table can also be elevated over a range of 300mm using a heavy duty motor system. This type of configuration offer additional advantages in the experimental hutch for setting large objects or in-situ devices and for selecting adequate distances between the sample and the detection system. The main components allocated over the optical table, described from bottom to up direction, are as follows:

- Long-X displacement stage: This linear stage will be mounted over the table and is a customized heavy duty stage (total load >50kg) that will move the sample in the beam direction with precisions over 1 micron. The estimated length of this component is 1.5 m which will allow varying the sample-detector distance and, as a consequence, the phase contrast signal. This stage is important for performing phase contrast and holotomography experiments.
- Short-Y translation Axis: This linear stage will also be moved in a horizontal plane, in a direction perpendicular to the long-X. The required total length of this stage is assumed to be 200-300mm. The main function of this stage is moving the sample out of the FOV for taking the flat-field images and, in principle +/-30mm of displacement would be enough. Nevertheless considering future development of the instrument, the required operational flexibility and the sample environment devices and set up we have consider x10 longer travel range in the final configuration.
- Z elevation & 3-point tip-tilt table: This elevation stage is conceived as a multipurpose system that allows simultaneously modifying the sample orientation (phi and psi angles) and the sample elevation. The sample orientation is achieved by moving independently each one of the 3 motors (reaching a range over 1º and accuracy better than 0.005º both for psi and phi angles). Sample height variation will be achieved by moving simultaneously the three motors. The total travel length of this system is 200mm.
- Rotating stage, high speed, feedtrough contacts: This is actually the main component of the tomography system. It required a high stability, a high rotation velocity (over 200 rpm, ideally up to 600rpm), high precision and low angular inaccuracies (wobble, eccentricity, flatness, etc). This stage also needs having feedthrough contacts for controlling the position of the eventual motors settled on the top of the system. The developed concept requires a customized design of air bearing rotating stage.
- X-Y micropositioners: These positioners are located in the top of the rotation table and allow for sample centering. They are minituarized components which incorporate piezomotors and total travel range of 6mm. They will be assembled in crossed directions to allow a complete sample centering.

- Sample holder system: A special magnetic sample holder system will be designed for sample attachment. The sample holder system allows easy sample replacement and ensures a perfect centering in the top of the stage.

Figure 49 shows a photograph of a system similar to the one described in this proposal. Among other components it is possible to observe the long X-axis, the "short" Y-axis, the tip-tilt Z system, the custom designed rotation stage and the micropositioners at the top.

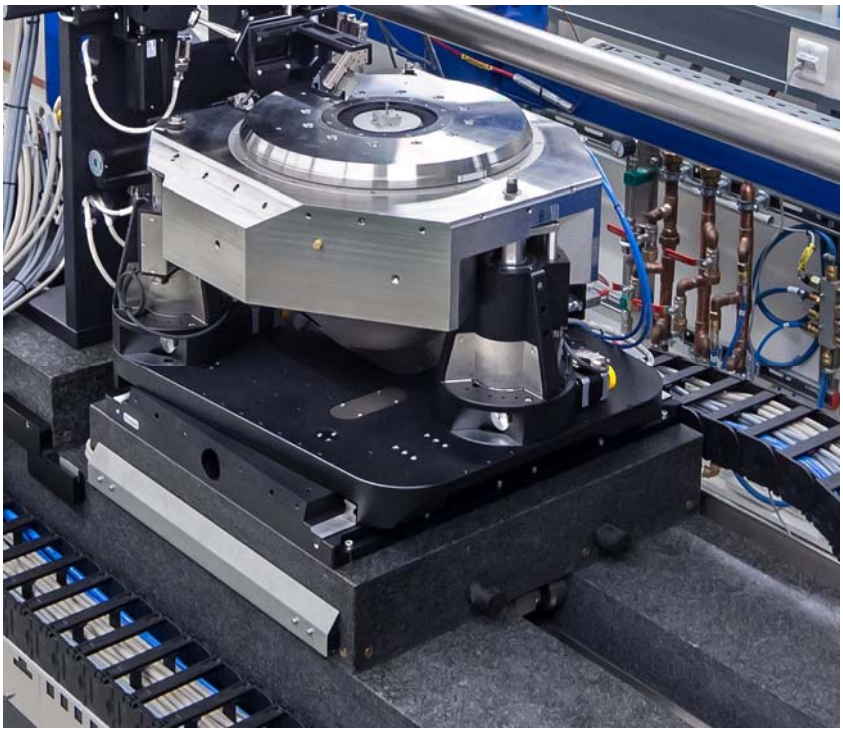

Figure 49. Zoomed photography of a system similar to the one intended to install at Alba (Courtesy of PIMicos Iberia).

Apart from the motion system described it is also important to consider in the total budget the price of the high precision motor controllers. All these components have been gently quoted by Micos Iberia. On the other hand we will not consider price for software, and this proposal assumes the software will be designed in-house by Alba software engineers.

5.5.2. Imaging systems

Two different imaging systems (microscopes) have been conceived to be installed in the beamline and will be used depending on the beam type used (monochromatic or white beam). The main differences between these two mentioned systems are associated with the location of the magnifying objectives within the optical path. In the case of monochromatic beam microscope, the objectives are settled in the X-ray beam direction while this is not possible in the case of white beam optical configuration since the objective may darken immediately under such strong radiation conditions. As a consequence white beam microscope is limited in terms of resolving power enabling a maximum of x4 magnifying lenses. Figure 50 shows a schematic drawing of both microscopes layout. Both systems will be developed by Peter Optique and will mount two different exchangeable high speed cameras. In principle, the fastest camera will be mounted in the white beam microscope and the second camera, with improved dynamic range and contrast resolution (SCMOS technology) will be considered for monochromatic experiments.

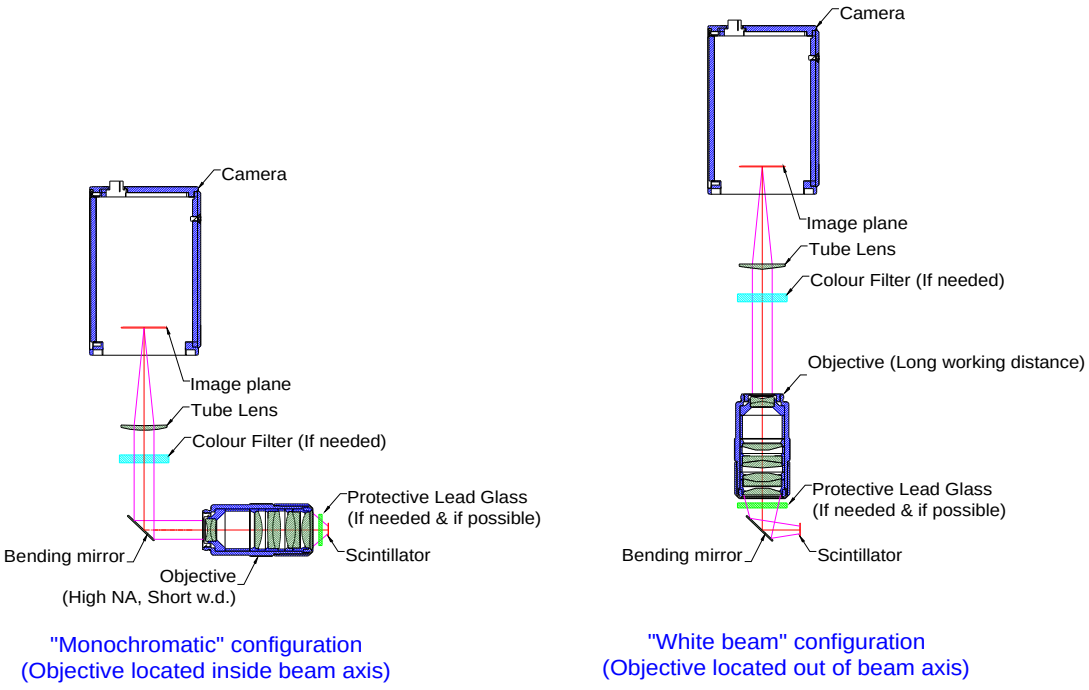

Figure 50. Schematic description of the two microscopes considered to be mounted at FaX-ToR beamline.

a) White beam microscope and PCO Dimax camera:

The concept of white beam microscope incorporates a mirror between scintillator and objective so the objective can be out of the path of the X-Ray beam. Under this design only backscattered light may brown the objective and a glass protective window can reduce further the backscattered radiation. As it is a long working-distance objective it presents a reduced numerical aperture and thus lower light collection and lower resolution. This is one of the reasons why the maximum magnification of the objective is limited to x4, although it could be possible to include a x10 objective (still under development). Approximate spatial resolutions for the x4 and x10 objectives will be in the order of 1.5 and 2.5µm.

The microscope includes a single scintillator support, a motorized focus (the motor will be installed and controlled by Alba staff), 1 objective (suitable for all objective magnifications), enlarging eyepiece for large format PCO Dimax, F-mount and mounting Brackets for PCO Edge, a housing for filter support and mechanical interface for mounting on X95 rails which allows moving the microscope in the vertical direction.

Figure 51. Left: 3D rendering of the white-beam microscope mounting a PCO. Dimax camera on top. Right: photography of a PCO. Dimax HS camera

The PCO.DIMAX HS4 camera is a CMOS monochrome camera with 12bits dynamic range incorporating a detector matrix of 2000x2000 pixels (pixel size 11 microns).

The internal memory of the camera is 36GB. The exposure time ranges 1.5 µs - 40 ms and therefore it would be possible to reach more than 7039 fps at 1 MPix resolution (1000x1000 pixel) or alternatively 5469 fps at 1.5 MPix resolution (1400x1050 pixel) and 2277 fps at 4 MPix resolution (2000x2000 pixel). Data communication included GigE, USB 3.0 and Cameralink interfaces. The fastest and therefore the recommended interface is the CameraLink and therefore a CameraLink PCI-Interface-Board mod. PCO-AD4-CL will be used. It also allows multiple trigger options. Although it has a Nikon mounting system the adaptor considered for the microscope allows an easy assembly.

b) Monochromatic microscope and PCO edge camera

The concept of the monochromatic microscope incorporates an objective in line with the X-Ray beam. As a result of the short working distance the objective has a higher numerical aperture and, thus, a better light collection and better resolution. One of the drawbacks of this design is that objectives may brown under high flux/high energy X-ray beam. To partially solve this problem, some objectives allow the mounting of a lead glass protective window. The microscope will mount 3 different objectives which allow modifying the resolution of the system. Namely the objectives will be x1.25, x4 and x10 thus yielding approximate spatial resolutions of (4.8, 1.5 and 0.6 microns).

The microscope includes a single scintillator support, a motorized focus (the motor will be installed and controlled by Alba staff), a motorised nosepiece with 3 positions for the objectives, a tiltable single scintillator support with large mount, F-mount and mounting brackets for F-mount camera, enlarging eyepiece for large format PCO Dimax, a housing for filter support and mechanical interface for mounting on X95 rails which allows moving the microscope in the vertical direction.

Figure 52. Left: 3D rendering of the monochromatic beam microscope mounting a PCO. Edge 4.2 camera on top. Right: photography of a PCO. Edge 4.2

The PCO Edge 4.2 camera is a SCMOS monochrome camera with 16bits and excellent dynamic range of 36000:1 with an extremely low noise of 0.8 e- med and quantum efficiency over 70%. It incorporates a detector matrix of 2048x2048 pixels (pixel size 6.5 microns). The maximum frame rate at full resolution is 100 fps but increases up to 420 at 1000x1000 pixels resolution. Data communication include, USB 3.0 and Cameralink interfaces. The fastest and therefore the recommended interface is the CameraLink so a CameraLink PCI-Interface-Board mod. PCO-AD4-CL will be used. Apart from the excellent image quality, one of the advantages of this camera is the small size and fast communication that allows the potential realization of high quality tomographies in short times.

5.6. Sample environment

We complementarily consider a set of devices that will allow performing in-situ tests at the beamline. As mentioned in the introduction this is a key issue to be considered since a set of attractive in-situ complementary devices, well controlled and adjusted by the beamline staff would allow to increase the number of potential users and ensures the quality of the research studies developed at the beamline.

5.6.1. Tensile, compression, fatigue test rigs

The in-situ devices are usually developed only for in-situ testing purposes. These devices are set directly on the rotary state and experience the same rotation as the

sample during the scans. A tensile/compression/fatigue device are normally developed based on a loading cell as the sensing device. The deformation can be achieved in several ways depending on the complexity of the device, e.g. by a spring, a motor, a motor coupled with a cantilever connected to an elliptical rotating cam, etc. The strain rate can be controlled by controlling the motor speed. In order to avoid the frame of the machine hiding the beam during the 180° rotation, different cylindrical X-ray transparent materials can be used (PMMA, glassy carbon, glass-ceramic materials, etc.) to transmit the load between the mobile grip and the fixed grip (normally fixed over the rotary stage). It is a common practice to record the force and the crosshead displacement on a computer and monitor it during the test. The maximum load normally ranges about 2kN which is usually sufficient for the sample dimensions that can be tested within the FOV of the tomography system. An example of a tensile/compression device is shown in Figure 53.

An important issue to be addressed in all in-situ experiments is the acquisition time. When the acquisition time is in the order of hours the test needs to be stopped during the acquisition. The sample is then relaxed during the tomographic measurement and some other effects could play an important role depending on the loading conditions and the material being tested, such as plastic deformation or creep. Fast acquisition rates (in the order or minutes or seconds) help to mitigate this problem and to obtain a more reliable experiment.

In summary, in-situ devices that apply a force to the specimen consist of a loading cell, an X-ray transparent tube, a motor, a case to hold all together with the sample grips, and the motor- and load cell- controllers and laptops/PCs normally located outside the experimental hatch.

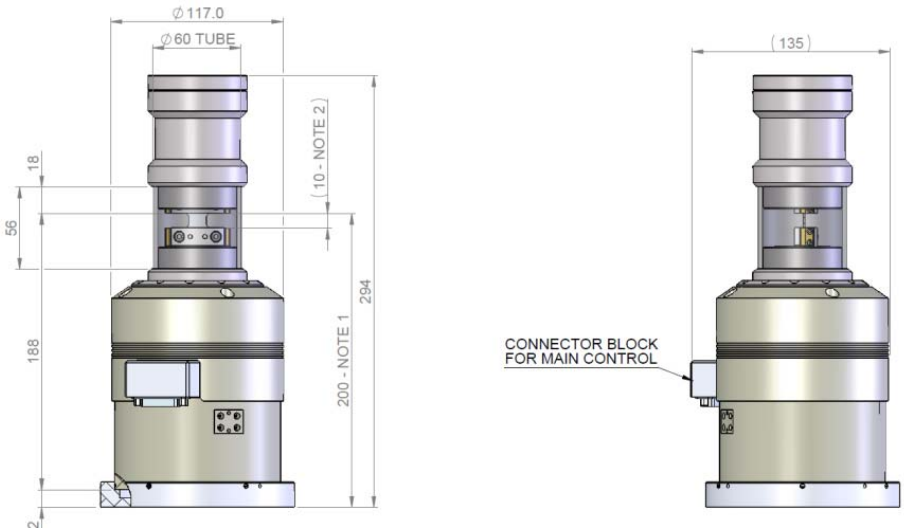

Figure 53. 3D CAD rendering of a tensile/compressive test rig compatible with microtomography experiments.

5.6.2. High temperature furnace

A radiation furnace that covers the temperature range from room temperature up to 1200 K will be designed and constructed for in situ synchrotron microtomography The furnace can also operate under a vacuum or under any inert gas atmosphere. Two 500 W halogen heating lamps with golden parabolic mirrors and the samples are located at the focus of these lamp reflectors on a rotary feedthrough that is connected to a driving rotation stage below the furnace. The X-ray beam penetrates the furnace through two X-ray-transparent vacuum-sealed windows. Further ports can be used for temperature control, sample exchanging, gas inflow and outflow and additional temperature sensors. The sample chamber is equipped with eight flanges (see Figure 54, right) for various purposes: one flange for mounting the rotation feedthrough from below, one flange for positioning and changing specimens from top, two X-ray transparent flanges and vacuum-sealed in the front and back, two flanges for gas inlet and outlet, and two flanges for mounting additional thermocouples. The X-ray-transparent windows are exchangeable and made of thin metal (e.g. aluminium), solid ceramic BN or Kapton, depending on the required temperature inside the furnace, on the X-ray energy and on the gas atmosphere or vacuum.

The samples are heated by radiation allowing for very fast heating and cooling rates. These heating and cooling rates depend mostly on the thermal absorption (emissivity) of the sample material. The energy of the bulbs is focused in a small heating spot the maximum sample temperature is to 1200 K. Owing to the small heating spot the maximal dimension of the specimen is limited to 1 cm which is in the range of the FOV of the beamline.

The precision of the temperature control and stability of the furnace is approximately 1 K. A schematic view of the inner layout of the furnace is presented in Figure 54, left. The furnace needs to be mounted on an additional stage that is located below the rotation table and allows the full system to be moved out of the beam for the required flatfield measurements. The sample inside the furnace is rotated during the measurements by a vacuum rotation feedthrough that is connected to the rotation stage below. The vacuum rotation feedthrough is installed in a flange at the bottom of the furnace and allows for a controlled atmosphere or even a vacuum to be maintained inside the sample chamber. The internal sample holder is made of refractory alumina rod since it presents a minimal thermal expansion. The tip of this rod is located at focal spot and provides an efficient temperature decoupling of the rotation stage from the furnace. Thus, only the sample itself and the refractory alumina rod that are heated up during the measurements.

The parabolic lamp chambers are made of polished aluminium (surface is golden) and separated from the sample chamber by two silica glass windows. These windows transmit the radiation, but separate the lamp atmosphere from the sample atmosphere and have independent cooling methods. The volume of the sample chamber is, then, minimized which reduces the required volume of gas and/or the evacuation time of the sample chamber. The sample chamber is water-cooled by a channel inside the housing. This allows for a large thermal gradient from the focus point of the lamps with up to 1800 K to the housing with an outer temperature of about 340 K even by working under gas atmosphere. A system similar to the one described by Grupp et al. [106] could be built by Novadep Scientific Instruments.

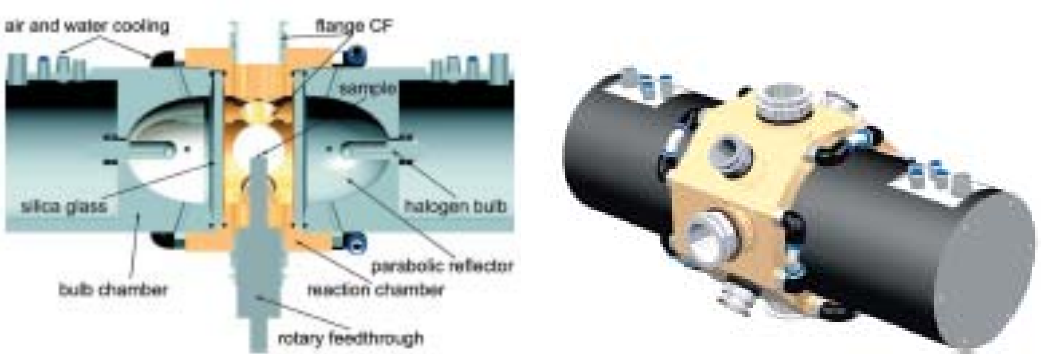

Figure 54. Cross section of the radiation furnace (right) and 3D rendering of the system (left). Different parts such as rotary feedtrough, parabolic reflectors and ports can be observed.

5.6.3. Cryogenic cell

Different cooling configurations have been considered in the approach of reaching in-situ extremely low temperatures (nearly -150ºC) during microtomography experiments. As far as it is known the most common systems compatible with X-ray tomography are based on Peltier stages. Nevertheless this possibility limits the temperature to a minimum of -20/-30ºC which might not be enough for several applications. One possible additional inconvenience is the formation of ice in the X-ray transparent windows with may cause imaging problems and/or complicated later corrections.

A double-layer cylindrical chamber system has been designed for this purpose. It basically consists in two concentrically-disposed tubes separated by a gap 5mm -vacuum- that will help to increase the insulation capacity of the system. The system is composed by an inner gold-plated kapton tube of 200 microns in thickness mounted inside a 1mm-thick PMMA tube. The gold-plated tube will reduce the radiation loses and the vacuum gap will help to reduce the system loses by convection and conduction. This will prevent the formation of ice in the external window. The formation of ice in the internal window will be avoided by circulating dry-air (nitrogen) through the chamber thus creating small positive pressure and avoiding wet air penetration. If required, a previous evacuation of the system could be performed. A pressurized liquid nitrogen reservoir is connected to the chamber by a heat exchanger system where the gas cools down. Temperature is regulated using two different electrolvalves (gas and liquid nitrogen) remotely controlled by a temperature controller providing a temperature accuracy better than 1ºC.

Sample is rotated from the bottom by using a rotary feedtrought. One of the novelties of the design is that the feedtrough rod contains a RTD Pt100 sensor in direct contact with the sample, thus providing a direct read out of the real temperature. The rod is made of insulating polymeric material to prevent heat loses. The cell can be fixed to a bottom stage through a couple of articulated arms. All the pipes and cables are flexible to allow an easy mounting. In this cell configuration (cylindrical) flatfields are acquired by moving the cell down to a region with no sample. The remote temperature control can be done by PC via RS-232 or USB.

5.6.4. High pressure cell

A high pressure cell (gas) with capacity of reaching 250bar and 250ºC is complementary described, thus completing the "collection" of set-ups included within the FaX-ToR beamline proposal. This cell is compatible with microtomography experiments. This cell is designed to be X-ray transparent (A6061-T6 aluminium tube 2mm thickness) and allows continuous gas feed during the experiments as well as pressure and temperature monitoring. The sample rotation is achived thanks to a magnetic coupling system that transmits the movement from the rotation stage. The magnetic coupling system presents zero-friction to rotation and can be rotated over 1000 rpm, thus not limiting the maximum speed for tomographic acquisition at the beamline. The inner cell dimensions limit the maximum sample diameter to 8mm. Flatfield images could can be acquired by moving down the whole tomographic table since the cell is attached to it.

The pressure sensor is connected to a high pressure electrovalve when the feeding system is a gas bottle at high pressure (200 or 300 bar). A needle valve, settled in series, allows regulating the feeding flux for a precise pressure regulation. PID parameters of the controller can be additionally adjusted. Alternatively, a booster system can be used for pumping other low pressure gasses and hydrocarbures. The high density (0.6-1.2 g/cm^3) of most of the pumped fluids at these high pressures would allow visualizing them with good contrast. As a consequence this system is ideal for the study of fluid infiltration in porous rocks and other materials at high pressures and therefore useful for geologic and petroleum extraction experiments. The heating system can be internal or either external and is regulated by a PID

controller. Both the pressure and the temperature controllers can be connected to a PC and configured remotely. Novadep Scientific offers different versions of this system. The one showed in Figure 55 is a conceptual design conceived for a different application. As a consequence, further refinements are required and the distance from the bottom to the sample position (200mm in the 3D sketch) should be reduced in our particular application.

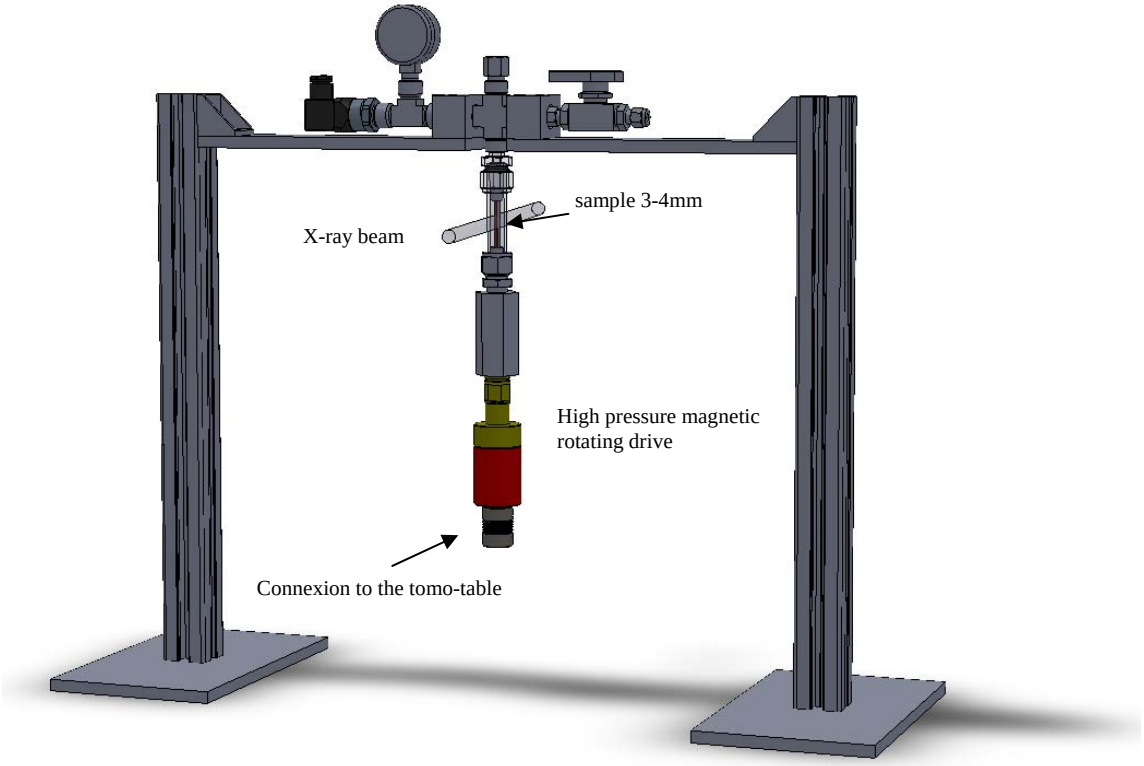

Figure 55. Conceptual design of the high-pressure set-up including the main components and the support

5.7. Computation and data storage

It is important to keep in mind that fast tomographic data acquisition presents as a collateral inconvenience the generation of large data sets (sometimes series of tens or tomographies are generated in a single experiment) that needs to be computed and stored. As an example a single campaign can easily generate more than 6TB of data. These facts are in apparent contradiction with one of the most important concerns of synchrotron beamlines, i.e. users should take home the full treated data sets before the campaign is ended.

Therefore in parallel to the beamline construction it is necessary to consider the implementation of a higher capability CPU cluster architecture for fast reconstruction of the tomographic data sets and the increase of Alba´s data storage capacity. Regarding fast tomographic reconstruction Alba currently has a medium-capacity cluster and, therefore, the update of CPU cluster as part as its general infrastructure could be partially covered by ALBA. On the other hand, regarding the data storage, ALBA has recently implemented a data storage system of 400 TB. This storage system should be increased in order to coupe with the needs of this imaging beamline. Therefore, the cost of extra data storage and CPU cluster upgrades specifically needed for this beamline will be considered.

5.8. Estimated budget

The following table summarizes the approximate costing of constructing and equipping the FaXToR beamline at ALBA

Beamline Optics	Price (k€)
UHV, mechanics, gate valves, control	205
Insertion device	797
Monochromator and mirror optics	448
Vacuum guide and CVD window	40
Front end	163
SUBTOTAL	1653
Lead Hutch	
X-ray shielding	302
SUBTOTAL	302
Experimental end-station	
Beam limiter (X-Y slits)	30
Beam Shutter II	18
Optical table	90
Long X translation Axis	120
Short Y translation Axis	37
Z elevation 3-point tip-tilt table	75
Rotating stage, high speed, trough contacts	160
X-Y micropositioners	12
Sample holder system	6
Motor controllers	45
White beam microscope	38
Monochromatic beam microscope	55
PCO DIMAX camera and accessories	74
PCO Edge camera and accessories	22
Scintillators	18
Computers, monitors	8
SUBTOTAL	808
Experimental end-station	
Tensile test rig	20
1200K furnace	38
Cryogenic	26
High pressure cell	20
SUBTOTAL	104
Computation and data storage	
CPU cluster	122
800Tb storage (8 months storage data policy; collecting 1-2 Tb/day)	626
SUBTOTAL	748
Infrastructure	
Conventional hutch (furniture & air conditioning included)	35
Supplies infrastructure	165
SUBTOTAL	200
Total	3815 k€
CONTINGENCY (10%)	382 k€
TOTAL	**4197 k€**

5.9. Future development

The beamline concept developed in this proposal aims at considering the future development of the instrument that would allow carrying out complementary experiments and new tomographic techniques. In this sense the present layout is compatible with the realization of nanotomography experiments which, in the opinion of the contributors to this proposal, is a very interesting techniques to establish in Alba (currently it is possible to carry out soft X-ray nanotomography at Mistral beamline). Nevertheless, additional components are required to carry out this and other techniques and, therefore prior to carrying out these developments it will be necessary to count with additional economical support from Alba.

REFERENCES

[1] T.F. Kelly, D.J. Larson. Atom Probe Tomography 2012. Annu. Rev. Mater. Res. 2012, 42:1-31.
[2] Z. Saghi, P.A. Midgley. Electron Tomography in the (S)TEM: From Nanoscale Morphology Analysis to 3D Atomic Imaging. Annu. Rev. Mater. Res. 2012, 42:59-79.
[3] P.D. Nellist, P. Wang. Optical Sectioning and Confocal Imaging and Analysis in the Transmission Electron Microscope. Annu. Rev. Mater. Res. 2012, 42:125-143.
[4] J.S. Brenizer. A Review of Significant Advances in Neutron Imaging from Conception to the Present. Physics Procedia, 2013, 43:10-20.
[5] W. Ludwig, A. King, P. Reischig, M. Herbig, E.M. Lauridsen, S. Schmidt, H. Proudhon, S. Forest, P. Cloetens, S. Rolland du Roscoat, J.Y. Buffière, T.J. Marrow, H.F. Poulsen. New opportunities for 3D materials science of polycrystalline materials at the micrometre lengthscale by combined use of X-ray diffraction and X-ray imaging, Mater. Sci. Eng. A, 2009, 524(1–2): 69-76.
[6] A. Zankel, J. Wagner, P. Poelt. Serial sectioning methods for 3D investigations in materials science, Micron 2014, 62:66-78.
[7] M.D. Uchic. Chapter: "Serial Sectioning Methods for Generating 3D Characterization Data of Grain- and Precipitate-Scale Microstructures", in Computational Methods for Microstructure-Property Relationships, 2011, pp. 31-52.
[8] I.M. Robertson, C.A. Schuh, J.S. Vetrano, N.D. Browning, D.P. Field, D.J. Jensen, M.K. Miller, I. Baker, D.C. Dunand, R. Dunin-Borkowski, B. Kabius, T. Kelly, S. Lozano-Perez, A. Misra, G.S. Rohrer, A.D. Rollett, M.L. Taheri, G.B. Thompson, M. Uchic, X.-L. Wang, G. Was. Towards an integrated materials characterization toolbox. J. Mater. Res., 2011, 26:1341-1383.
[9] E. Maire, P.J. Whiters. Quantitative X-ray tomography. Int. Mater. Rev. 2014, 59:1-43.
[10] J. Baruchel, J.-Y. Buffiere, E. Maire, P. Merle, G. Peix. X-ray Tomography in Material Science. HERMES Science Publications, 2000, ISBN 2-7462-0115-1.
[11] J. Banhart. Advanced Tomographic Methods in Materials Research and Engineering. Oxford University Press 2008, ISBN 978-0-19-921324-5.
[12] S.R. Stock. MicroComputed Tomography. Methodology and Applications. CRC Press, 2009, ISBN 978-1-4200-5876-5.
[13] A. Pyzalla, B. Camin, T. Buslaps, M. Di Michiel, H. Kaminski, A. Kottar, A. Pernack and W. Reimers. Simultaneous tomography and diffraction analysis of creep damage, Science, 2005, 308(5718):92–95.
[14] F. Sket, K. Dzieciol, A. Borbély, A.R. Kaysser-Pyzalla, K. Maile, R. Scheck. Microtomographic investigation of damage in E911 steel after long term creep. Mater. Sci. Eng. A, 2010, 528(1): 103-111.
[15] A. Vagnon, O. Lame, D. Bouvard, M. Di Michiel, D. Bellet, G. Kapelski. Deformation of steel powder compacts during sintering: correlation between macroscopic measurement and in situ microtomography analysis. Acta Mater., 2006, 54(2):513–522.
[16] C. Puncreobutr, P. D. Lee, R. W. Hamilton and A. B. Phillion. Quantitative 3D characterization of solidification structure and defect evolution in Al alloys. JOM, 2012, 64(1):89–95.
[17] F. Sket, M. Rodríguez-Hortalá, J. M. Molina-Aldareguía, J. Llorca, E. Maire, G. Requena. In situ tomographic investigation of damage development in ±45º carbon fibre reinforced laminates. Mater. Sci. Tech. Ser. 2014, in press.
[18] O. Ludwig, M. Dimichiel, L. Salvo, M. Suery, P. Falus. In-situ three-dimensional microstructural investigation of solidification of an Al-Cu alloy by ultrafast X-ray microtomography. Metall. Mater. Trans. A, 2005, 36A(6):1515–1523.
[19] N. Limodin, L. Salvo, M. Suery, M. DiMichiel. In situ investigation by X-ray tomography of the overall and local microstructural changes occurring during partial remelting of an Al-15.8 wt.% Cu alloy. Acta Mater., 2007, 55(9):3177–3191.
[20] D. Tolnai, G. Requena, P. Cloetens, J. Lendvai and H. P. Degischer. Sub-micrometre holotomographic characterisation of the effects of solution heat treatment on an AlMg7.3Si3.5 alloy. Mater. Sci. Eng. A Struct. Mater., 2012, 550:214–221.
[21] D. Bauer, S. Youssef, M. Fleury, S. Bekri, E. Rosenberg, O. Vizika. Improving the estimations of petrophysical transport behavior of carbonate rocks using a dual pore network approach combined with computed microtomography. Transp. Porous Med., 2012, 94:505–524.
[22] A. P. Jivkov, C. Hollis, F. Etiese, S. A. McDonald, P. J. Withers. A novel architecture for pore network modelling with applications to permeability of porous media. J. Hydrology, 2013, 486:246–258.

[23] B.K. Bay. Methods and applications of digital volume correlation. J. Strain Anal. Eng. Des., 2008, 43 (8):745–760.
[24] F. Forsberg, R. Mooser, M. Arnold, E. Hack, P. Wyss. 3D micro-scale deformations of wood in bending: Synchrotron radiation mu CT data analyzed with digital volume correlation. J. Struct. Biol., 2008, 164(3):255–262.
[25] S. F. Nielsen, H. F. Poulsen, F. Beckmann, C. Thorning, J. A. Wert. Measurements of plastic displacement gradient components in three dimensions using marker particles and synchrotron X-ray absorption microtomography. Acta Mater., 2003, 51(8):2407–2415.
[26] E. Ando, S. A. Hall, G. Viggiani, J. Desrues, P. Besuelle. Grain-scale experimental investigation of localised deformation in sand: a discrete particle tracking approach. Acta Geotechnica, 2012, 7(1):1–13.
[27] http://www.psi.ch/sls/tomcat/tomcat. Last accessed 11/10/2014.
[28] P. Babin, G. Della Valle, H. Chiron, P. Cloetens, J. Hoszowska, P. Pernot, A. L. Reguerre, L. Salvo, R. Dendievel. Fast X-ray tomography analysis of bubble growth and foam setting during breadmaking. J. Cereal Sci., 2006, 43(3):393–397.
[29] R. Mokso, F. Marone, D. Haberthuer, J. C. Schittny, G. Mikuljan, A. Isenegger, M. Stampanoni. Following dynamic processes by X-ray tomographic microscopy with subsecond temporal resolution, in '10th International Conference on X-Ray Microscopy', (eds. I. McNulty, et al.), 2011, pp 38–41. Melville, NY, American Institute of Physics.
[30] http://www.esrf.eu/UsersAndScience/Experiments/Imaging/ID19. Last accessed 11/10/2014.
[31] B.A. Dowd, G.H. Campbell, R.B. Marr, V.K. Nagarkar, S.V. Tipnis, L. Axe, D.P. Siddons. Developments in synchrotron X-ray computed tomography at the National Synchrotron Light Source. Developments in X-ray tomography II. Proc. SPIE, 1999,3772: 224–236.
[32] M. Rivers, Y. Wang. Recent developments in microtomography at GeoSoilEnviroCARS. Developments in X-ray tomography V. Proc. SPIE, 2006,6318: J3180.
[33] N.S. Ramesh, D.H. Rasmussen, G.A. Campbell. The heterogeneous nucleation of microcellular foams assisted by survival of microvoids in polymers containing low glass transition particles. Part I: Mathematical modeling and numerical simulations. Polym. Eng. Sci., 1994, 34:1685-1697.
[34] R.D. Patel. Bubble growth in viscous newtonian fluid. Chem. Eng. Sci., 1980, 35:2352-2356.
[35] M. Amon, C.D. Denson. A study of the dynamics of foam growth analysis of the growth of closely spaced spherical bubbles. Polym. Eng. Sci., 1984,24:1026-1034.
[36] N. Limodin, L. Salvo, E. Boller, M. Suéry, M. Felberbaum, et al. In situ and real-time 3-D microtomography investigation of dendritic solidification in an Al–10 wt.% Cu alloy. Acta Mater., 2009,57 (7): 2300-2310.
[37] S. Terzi, J.A. Taylor, Y.H. Cho, L. Salvo, M. Suéry, et al. In situ study of nucleation and growth of the irregular α-Al/β-Al5FeSi eutectic by 3-D synchrotron X-ray microtomography. Acta Mater. 2010,58(16): 5370-5380.
[38] D. Tolnai, P. Townsend, G. Requena, L. Salvo, J. Lendvai, H.P. Degischer. In situ synchrotron tomographic investigation of the solidification of an AlMg4.7Si8 alloy. Acta Mater., 2012, 60(6-7):2568-2577.
[39] M. Suéry, J. Adrien, C. Landron, S. Terzi, E. Maire, et al. Fast in-situ X-ray micro tomography characterisation of microstructural evolution and strain-induced damage in alloys at various temperatures. Int. J. Mater. Res., 2010, 101 (9): 1080-1088.
[40] H. Toda, E. Maire, S. Yamauchi, H. Tsuruta, T. Hiramatsu, M. Kobayashi. In situ observation of ductile fracture using X-ray tomography technique. Acta Mater., 2011, 59(5): 1995-2008.
[41] J.Y. Buffiere, E. Maire, J. Adrien, J.P. Masse, E. Boller. In Situ Experiments with X ray Tomography: An Attractive Tool for Experimental Mechanics. Exp. Mech. 2010, 50:289–305.
[42] P. Lhuissier, M. Scheel, M. Di Michiel, L. Salvo, E. Maire, M. Suery. Euromat 2011, Montpellier.
[43] N. Vanderesse, E. Maire, M. Darrieulat, F. Montheillet, M. Moreaud, D. Jeulin. Three-dimensional microtomographic study of Widmanstätten microstructures in an alpha/beta titanium alloy. Scr. Mater., 2008, 58(6):512-515.
[44] G. Requena, P. Cloetens, W. Altendorfer, C. Poletti, D. Tolnai, et al. Sub-micrometer synchrotron tomography of multiphase metals using Kirkpatrick–Baez optics. Scr. Mater., 2009, 61(7):760-763.
[45] G. Requena, G. Garcés, M. Rodríguez, T. Pirling, P. Cloetens. 3D architecture and load partition in eutectic Al-Si alloys. Adv. Eng. Mater., 2009, 11(12):1007-1014.

[46] H. Toda, T. Nishimura, K. Uesugi, Y. Suzuki, M. Kobayashi. Influence of high-temperature solution treatments on mechanical properties of an Al–Si–Cu aluminum alloy. Acta Mater., 2010, 58(6): 2014-2025.
[47] Y. Liu, F. Meirer F, Wang J, Requena G, Williams P, et al. 3D Elemental sensitive imaging using transmission X-ray microscopy. Anal. Bioanal. Chem. , 2012, 404(5):1297-1301.
[48] D. Tolnai, G. Requena, P. Cloetens, J. Lendvai, H.P. Degischer. Sub-micrometer holotomographic characterization of the effects of solution heat treatment on an AlMg7.3Si3.5 alloy. Mat. Sci. Eng. A., 2012, 30, 214-221.
[49] F. Ostermann. Anwendungstechnologie Aluminium. Berlin: Springer, 2007.
[50] R. Mendoza, J. Alkemper, P.W. Voorhees. The morphological evolution of dendritic microstructures during coarsening. Metall. Mater. Trans. A., 2003, 34:481-489.
[51] A. Mortensen. On the influence of coarsening on microsegregation. Metall. Trans. A., 1989, 20(2): 247-253.
[52] R.E. Reed-Hill, R. Abbaschian. Physical Metallurgy, third ed. PWS-Kent, Boston, 1992.
[53] D.R. Baker, F. Brun, C. O'Shaughnessy, L. Mancini, J.L. Fife, M. Rivers. A four-dimensional X-ray tomographic microscopy study of bubble growth in basaltic foam. Nature Commun., 2012, 3:1135.
[54] J.C. Eichelberger, C.R. Carrigan, H.R. Westrich, R.H. Price. Non-explosive silicic volcanism. Nature, 1986, 323:598–602.
[55] M. Voltolini, D. Zandomeneghi, L. Mancini, M. Polacci. Texture analysis of volcanic rock samples: Quantitative study of crystals and vesicles shape preferred orientation from X-ray microtomography data. J. Volcanol. Geoth. Res., 2011, 201(1-2):83-95.
[56] R.J. Carey, M. Manga, W. Degruyter, H. Gonnermann, D. Swanson, B. Houghton, T. Orr, M. Patrick. Convection in a volcanic conduit recorded by bubbles Geology, 2013, 41:395–398.
[57] J.M. Watkins, M. Manga, D.J. DePaolo. Bubble geobarometry: A record of pressure changes, degassing and regassing and Mono Craters: California Geology, 2012, 40:699–702.
[58] J.L. Fife, M. Rappaz, M. Pistone, T. Celcer, G. Mikuljan, S. Stampanoni. Development of a laser-based heating system for in-situ synchrotron-based x-ray tomographic microscopy. J. Synchrotron Radiation, 2012, 19:352-358.
[59] M. Pistone. Physical properties of crystal-and bubble-bearing magmas. PhD diss, 2012, ETH 20698, 1- 442.
[60] K. Watanabe, T. Yano, K. Takeshita, K. Minami, E. Ochi. X-ray CT imaging of vitrified glasses containing simulant radioactive wastes: structure and chemical reactions of glass beads and wastes in the cold cap. Glass Technology - European Journal of Glass Science and Technology, 2012, 53:273-278.
[61] E.W. Llewellin, M. Manga. Bubble suspension rheology and implications for conduit flow. J. Volcanol. Geotherm. Res., 2005, 143:205-217.
[62] J.M. Aguilera. Microstructure and food product engineering. Food Technology, 2000, 54(11):56-65.
[63] J.M. Aguilera. Why food microstructure. J. Food Eng., 2005, 67(1-2):3-11.
[64] F. Mendoza, P. Verbove, H.K. Mebatsion, G. Kerckhofs, M. Wevers, B. Nicolaï. Three-dimensional pore space quantification of apple tissue using X-ray computed microtomography. Planta, 2007, 226:559–570.
[65] H.K. Mebatsion, P. Verboven, A. Melese Endalew, J. Billen, Q.T. Ho, B.M. Nicolaï. A novel method for 3-D microstructure modeling of pome fruit tissue using synchrotron radiation tomography images. J. Food Eng., 2009, 93:141–148.
[66] P.M. Falcone, A. Baiano, F. Zanini, L. Mancini, G. Tromba, D. Dreossi, F. Montanari, N. Scuor, M.A. Del Nobile. Three-dimensional Quantitative Analysis of Bread Crumb by X-ray Microtomography. J. Food Sci., 2005, 70:E265-E274.
[67] N. Lassoued, P. Babin, G. Della Valle, M.F. Devaux, A.-L. Realguerre. Granulometry of bread crumb grain: Contributions of 2D and 3D image analysis at different scale. Food Res. Int., 2007, 40:1087–1097.
[68] P. Pittia, G. Sacchetti, L. Mancini, M. Voltolini, F. Brun, G. Tromba, N. Sodini, F. Zanini. Evaluation of microstructural properties of coffee beans by synchrotron X-ray microtomography: a methodological approach. J. Food Sci., 2011, 76(2):E222-E231.
[69] Y. Wang, X. Liu, K.S. Im, W.K. Lee, J. Wang, K. Fezzaa, D.L.S. Hung, J.R. Winkelman. Ultrafast X-ray study of dense-liquid-jet flow dynamics using structure-tracking velocimetry. Nat. Phys. 2008, 4:305–309.

[70] A. Rack, F. Garcia-Moreno, C. Schmitt, O. Betz, A. Cecilia, A. Ershov, T. Rack, J. Banhart, S. Zabler. On the possibilities of hard X-ray imaging with high spatio-temporal resolution using polychromatic synchrotron radiation. J. X-Ray Sci. Technol. 2010, 18:429–444.
[71] F. Garcia-Moreno, A. Rack, L. Helfen, T. Baumbach, S. Zabler, N. Babcsán, J. Banhart, T. Martin, C. Ponchut, M. di Michiel. Fast processes in liquid metal foams investigated by high-speed synchrotron X-ray micro-radioscopy. Appl. Phys. Lett. 2008, 92:134104–134106.
[72] A. Rack, F. Garcia-Moreno, T. Baumbach, J. Banhart. Synchrotron-based radioscopy employing spatio-temporal micro-resolution for studying fast phenomena in liquid metal foams. J. Synchrotron Rad. 2009, 16:432–434.
[73] H. Stanzick, J. Banhart, T. Helfen, T. Baumbach. In-situ monitoring of metal foam evolution and decay. In Foams and Emulsions; Zitha, P., Banhart, J., Verbist, G., Eds.; MIT-Verlag: Bremen, Germany, 2000; pp.290–296.
[74] J. Banhart, H. Stanzick, L. Helfen, T. Baumbach, K. Nijhof. Real-time X-ray investigation of Aluminium Foam Sandwich production. Adv. Eng. Mater. 2001, 3:407–411.
[75] H. Stanzick, M. Wichmann, J. Weise, L. Helfen, T. Baumbach, J. Banhart. Process control in aluminium foam production using real-time x-ray radioscopy. Adv. Eng. Mater. 2002, 4:814–823.
[76] F. Garcia-Moreno, M. Mukherjee, C. Jimenez, A. Rack, J. Banhart. Metal foaming investigated by X-ray radioscopy. Metals 2012, 2(1):10–21.
[77] V. Gergely, T.W. Clyne. Drainage in standing liquid metal foams: modelling and experimental observations. Acta Mater. 2004, 52:3047–3058.
[78] A. Isaac, F. Sket, W. Reimers, B. Camin, G. Sauthoff, A.R. Pyzalla. In situ 3D quantification of the evolution of creep cavity size, shape, and spatial orientation using synchrotron X-ray tomography. Mater. Sci. Eng. A, 2008, 478:108-119.
[79] G. Requena, G. Garcés, M. Rodríguez, T. Pirling, P. Cloetens. 3D Architecture and Load Partition in Eutectic Al-Si Alloys. Adv. Eng. Mater., 2009, 11(12): 1007-1014.
[80] Z. Asghar, G. Requena, E. Boller. 3D Interpenetrating Hybrid Network of rigid phases in an AlSi10Cu5NiFe Piston Alloy, Pract Metallogr., 2010, 47(9):471-486.
[81] Z. Asghar, G. Requena, F. Kubel. The role of Ni and Fe aluminides on the elevated temperature strength of an AlSi12 alloy. Mater. Sci. Eng A, 2010, 527:5691-5698 (2010).
[82] P. Cloetens, W. Ludwig, J. Baruchel, D. Van Dyck, J. Van Landuyt, J. P. Guigay, and M. Schlenker. Holotomography: Quantitative phase tomography with micrometer resolution using hard synchrotron radiation x-rays. Appl. Phys. Lett., 1999, 75(19):2912–2914.
[83] P.J. Withers. X-ray nanotomography. Materials Today, 2007, 10(12):26-
[84] R. Mokso, P. Cloetens, E. Maire, W. Ludwig, and J.-Y. Buffière. Nanoscale zoom tomography with hard x rays using Kirkpatrick-Baez optics. Appl. Phys. Lett., 2007, 90(14), 144104-144104-3.
[85] O. Betz, U. Wegst, D. Weide, M. Heethoff, L. Helfen, W.K. Lee, P. Cloetens. Imaging applications of synchrotron X-ray phase-contrast microtomography in biological morphology and biomaterials science. I. General aspects of the technique and its advantages in the analysis of millimetre-sized arthropod structure. J. Microsc. 2007, 227:51-71.
[86] P. Lamata, R. Casero, V. Carapella, S.A. Niederer, M.J. Bishop, J.E. Schneider, P. Kohl, V. Grau. Images as drivers of progress in cardiac computational modelling. Prog. Biophys. Mol. Biol., 2014, in press.
[87] http://en.wikipedia.org/wiki/Virtual_Physiological_Human.
[88] O.V. Aslanidi, T. Nikolaidou, J. Zhao, B.H. Smaill, S.H. Gilbert, A.V. Holden, T. Lowe, P.J. Withers, R.S. Stephenson, J.C. Jarvis, J.C. Hancox, M.R. Boyett, H. Zhang. Application of micro-computed tomography with iodine staining to cardiac imaging, segmentation, and computational model development. IEEE Trans Med Imaging. 2013, 32:8-17.
[89] Q, Gonzalez Tendero, R. Cardenes, C. Zhang, A. Bonnin, E. Demicheva, E. Gratacos, F. Crispi, B. Bijnens. Detailed assessment of cardiac anatomy, myofiber structure and vasculature of rodent hearts using X-ray phase-contrast synchrotron radiation-based micro-CT. Cardiovascular research 2004, 103(suppl 1):S142-S142.
[90] M.A. Beltran, D.M. Paganin, K.K. Siu, A. Fouras, S.B. Hooper, D.H. Reser, M.J. Kitchen. Interface-specific x-ray phase retrieval tomography of complex biological organs. Phys Med Biol. 2011, 56(23):7353-69.
[91] G. Schulz, C. Waschkies, F. Pfeiffer, I. Zanette, T. Weitkamp, C. David, B. Müller. Multimodal imaging of human cerebellum - merging X-ray phase microtomography, magnetic resonance microscopy and histology. Sci Rep. 2012, 2:826.

[92] O.J. Arthurs, S. Thayyil, O.E. Olsen, S. Addison, A. Wade, R. Jones, W. Norman, R.J. Scott, N.J. Robertson, A.M. Taylor, L.S. Chitty, N.J. Sebire, C.M. Owens. Diagnostic accuracy of post-mortem MRI for thoracic abnormalities in fetuses and children. Eur Radiol. 2014, in press.
[93] A.M. Taylor, N.J. Sebire, M.T. Ashworth, S. Schievano, R.J. Scott, A. Wade, L.S. Chitty, N. Robertson, S. Thayyil. Magnetic Resonance Imaging Autopsy Study Collaborative Group. Postmortem cardiovascular magnetic resonance imaging in fetuses and children: a masked comparison study with conventional autopsy. Circulation, 2014, 129(19):1937-44.
[94] S.B. Hooper, M.J. Kitchen, M.L. Siew, R.A. Lewis, A. Fouras, A.B. te Pas, K.K. Siu, N. Yagi, K. Uesugi, M.J. Wallace. Imaging lung aeration and lung liquid clearance at birth using phase contrast X-ray imaging. Clin. Exp. Pharmacol. Physiol., 2009, 36(1):117-25.
[95] H. Gomes Rodrigues, P. Marangoni, R. Šumbera, P. Tafforeau, W. Wendelen, L. Viriot. Continuous dental replacement in a hyper-chisel tooth digging rodent. Proc. Natl. Acad. Sci., 2011, 108:17355-17359.
[96] P. Tafforeau, R. Boistel, E. Boller, A. Bravin, M. Brunet, Y. Chaimanee, P. Cloetens, M. Feist, J. Hoszowska, J.-J. Jaeger, R.F. Kay, V. Lazzari, L. Marivauw, A. Nel, C. Nemoz, X. Thibault, P. Vignaud, S. Zabler. Applications of X-ray synchrotron microtomography for non-destructive 3D studies of paleontological specimens. Applied Physics A, 2006, 83195–202.
[97] P.C.J. Donoghue, S. Bengtson, X.-p Dong, N.J. Gostling, T. Huldtgren, J.A. Cunningham, C. Yin, Z. Yue, F. Peng, M. Stampanoni. Synchrotron X-ray tomographic microscopy of fossil embryos. Nature, 2006, 442: 680–683.
[98] Z. Gai, P.C.J. Donoghue, M. Zhu, P. Janvier, M. Stampanoni. Fossil jawless fish from China foreshadows early jawed vertebrate anatomy. Nature (London, United Kingdom), 2011, 476:324–327.
[99] M. Dierick, V. Cnudde, B. Masschaele, J. Vlassenbroeck, L. Van Hoorebeke, P. Jacobs. Micro-CT of fossils preserved in amber. Nuclear Instruments and Methods in Physics Research Section A: Accelerators, Spectrometers, Detectors and Associated Equipment, 2007, 580(1):641–643.
[100] D. Penney, M. Dierick, V. Cnudde, B. Masschaele, J. Vlassenbroeck, L. Van Hoorebeke, P. Jacobs. First fossil micropholcommatidae (Araneae), imaged in eocene Paris amber using X-ray computed tomography. Zootaxa, 2007, 1623:47–53.
[101] J. Bosselaers, M. Dierick, V. Cnudde, B. Masschaele, L. Van Hoorebeke, P. Jacobs. High-resolution X-ray computed tomography of an extant new Donuea (Araneae: Liocranidae) species in Madagascan copal. Zootaxa, 2010, 2427:25–35.
[102] M. Perreau, P. Tafforeau. Virtual dissection using phase-contrast X-ray synchrotron microtomography: reducing the gap between fossils and extant species. Systematic Entomology, 2011, 36(3):573–580.
[103] H. Henderickx, P. Tafforeau, C. Soriano. Phase-contrast synchrotron microtomography reveals the morphology of a partially visible new Pseudogarypus in Baltic amber (Pseudoscorpiones: Pseudogarypidae). Palaeontologia Electronica, 2012, 15(2).
[104] V. Cnudde, M.N. Boone, High-resolution X-ray computed tomography in geosciences: A review of the current technology and applications. Earth-Sci. Rev., 2013, 123:1–17
[105] R.P. Speijer, D. Van Loo, B. Masschaele, J. Vlassenbroeck, V. Cnudde, P. Jacobs. Quantifying foraminiferal growth with high-resolution X-ray computed tomography: new opportunities in foraminiferal ontogeny, phylogeny, and paleoceanographic applications. Geosphere, 2008, 4(4):760–763.
[106] R. Grupp, F. Henkel, M. Noethe, J. Banhart, B. Kieback, A. Haibel. A 1800 K furnace designed for in situ synchrotron microtomography. J. Synchrotron Rad., 2009,16:524–527.

ANNEX 1. Letters of support from Spanish companies and relevant institutions

TOLSA, S.A.

P. E. Las Mercedes - C/ Campezo, 1
Edificio 4 - 2ª Planta - 28022 Madrid. Spain
T 34 913 220 100 - F 34 913 220 101

www.tolsa.com

Madrid, October 10th 2014

Dear Sir/Madam,

Our company, Tolsa group has extracted clay minerals and researched, developed and manufactured products for domestic and industrial consumption for more than half a century. TOLSA is the world leader in the production of sepiolite, and has over 50 different applications in many industrial sectors, and through continuous development offer innovative solutions to customer needs In this respect, the research work at TOLSA is developed together with other research groups from the world´s most prestigious universities and research centres.

We have been made aware of the proposal of development of a synchrotron X-ray imaging system for carrying out radioscopy and fast tomography experiments at the Spanish Synchrotron facility, ALBA. This powerful technique is already making an important impact in many areas of research, such as materials, minerals, geology and polymer science, all of which are important in our industrial field.

Therefore, we wish to express our interest in, and support to, the success of the FaXTor project, as it will provide an important characterization technique to research groups from diverse areas in Spain

Yours sincerely

Julio Santaren

Group Technological Innovation Manager

Ref.: 0121-14S

Inscrita en el Registro Mercantil de Madrid. Tomo: 1.297 General: 765 Sección: 3ª Folio: 211 Hoja: 4.891 Inscripción: 1ª NIF: A-28077709 IVA ESA: 28077709

REPSOL

Cellular Materials Laboratory (CellMat) -
Condensed Matter Physics Department - University of Valladolid
Campus Miguel Delibes - Paseo de Belén, nº7. 47011 Valladolid Spain)

A/A.: Miguel Ángel Rodríguez Pérez

Repsol, S.A. hereby confirms its general interest in the project titled FaXToR proposal which will be presented to the SAC in October 2014.

For several years Repsol maintain a close interaction with academic research groups through Research Projects and Contracts for the study of the capability of our polymers to be structured in the shape of cellular materials. We are aware that the access to advanced characterization technique is a key issue and, in this respect, the FaXTor proposal for the development of a beamline dedicated to fast X-ray imaging at the Alba Synchrotron in Barcelona is of great interest.

The availability of a X-ray tomography beamline will undoubtedly be valuable for the academic and industrial research programmes in Spain.

No contractual consent shall be deemed to have been given by REPSOL, S.A., nor shall any form of binding obligation on the parties be deemed to have been created, to have arisen, or be explicitly or implicitly assumed as a result of execution of this letter until such time as they should decide to set down in writing any terms they may have agreed, both of them signing the documents required in order to formalise any possible contract relationship.

REPSOL S.A.

By: _____

REPSOL

Name: Juan Miguel Moreno

Title: D. Technology Chemicals

Date: 13.10.2014

Andalusian Foundation for
Aerospace Development

Center for Advanced
Aerospace Technologies

To whom it may concern

As responsible for the Department of Materials and Processes of Advanced Aerospace Technology Center (CATEC) I would like to express the support of the Center to build a fast tomography imaging beamline at ALBA. We believe the FaxToR proposal encourage the construction of a fundamental beamline at ALBA with a technique of great potential to resolve important fundamental and applied aspects in materials science. In this respect, a fast synchrotron X-ray imaging facility will be very useful for the growth of the scientific and industrial activity in Spain.

Yours sincerely,

Dr. Fernando A. Lasagni
flasagni@catec.aero
Materials & Processes Department
Center for Advanced Aerospace Technologies (CATEC)
Parque Tecnológico y Aeronáutico de Andalucia
C/Wilbur y Orville Wright, 17-19-21, 41309 La Rinconada - Sevilla
Phone: +34 954 179 002
Fax: +34 954 115 193
http://www.catec.aero/

Geleen, Netherlands, October 20th 2014

Dear all,

Sabic as a global manufacturing leader for polymeric materials and material science innovations strongly supports the development of new materials as one of the main pillars for product competitiveness. Our R&D departments have collaborated for several years with Universities and Research Centers in the study of fundamental and structural aspects of polymer science and polymer products. In this respect, the availability of powerful characterization tools has proven essential in many projects.

In relation with the previous, I have been made aware trough Dr. Eusebio Solórzano from the University of Valladolid, of the objectives and plans of work in their FaXToR proposal which is centered on building a Synchrotron X-ray imaging system for carrying out fast tomography experiments at Alba Synchtrotron facility.

I would like to express my support to this project since I consider this technique very powerful to resolve fundamental and applied aspects in polymeric materials science, an area where SABIC is particularly interested on.

Best Regards,

Dr. Martin van Es

20 oct '14 Geleen

Chief Scientist
Material Development
Technology & Innovation
Sabic Innovation Center Geleen, Netherlands

MINISTERIO
DE ECONOMÍA
Y COMPETITIVIDAD

Instituto Geológico
y Minero de España

Madrid, 26th September 2014

To whom it may concern,

This letter is to express our interest and support for the initiative of constructing a **High-energy imaging beamline** at the Spanish Synchrotron ALBA in Cerdanyola del Vallès.

The access to such a versatile and powerful technique in Spain will be beneficial to both academic and industrial researchers alike, and will be particularly interesting for the study, among others, of sedimentary rocks and their reservoir properties such as texture and porosity. This technique can provide remarkable 3D information of pore abundance and pore interconnection, and evaluate their volume and distribution. It will also allow discriminate between different mineral phases, such as calcite and dolomite, at a higher resolution than other techniques.

A high-energy tomography beamline in Spain is of significant interest to the geosciences community in general, and particularly to those researches working in the study of characterization and heterogeneity of sedimentary reservoirs for hydrocarbons, aquifers, or for storage of CO_2.

In conclusion, we consider that access to this beamline will be very useful for the scientific activities carried out in our Department of Research in Geological Resources, and is eagerly awaited by some of us who are already using this technique for our research.

Sincerely,

Idoia Rosales
Científico Titular
Instituto Geológico y Minero de España
La Calera 1, 28760 Tres Cantos, Madrid

MINISTERIO DE ECONOMÍA Y COMPETITIVIDAD
Instituto Geológico y Minero de España

CORREO ELECTRÓNICO
igme@igme.es

RÍOS ROSAS, 23
28003-MADRID
TEL.: 91 349 5700
FAX: 91 442 6216

Universidad de Extremadura
2014-June-19
Sören Jensen

To: The Scientific Advisory Committee for
the ALBA Phase-III Beamline upgrade

Letter of support for project "High-energy imaging beamline"

Tomography has over the last decades become increasingly applied to palaeontological studies. Among its obvious advantages is that it is a non-destructive technique, and that it enables the visualization of fossils in modes of preservation that hitherto were essentially impossible to study. Well known examples include studies of exceptionally preserved tiny arthropods in nodules that have been rendered in exquisite detail. Tomography has also been used for the study of trace fossils. Here an obvious advantage is the possibility to reconstruct three-dimensionally complex burrow systems within rock samples. Again, these are fossils that are essentially impossible to examine by conventional methods, or they require serial grinding, which is a destructive and highly time consuming technique.

My particular interest in using tomography in palaeontological studies is in the examination of late Ediacaran and Cambrian trace fossils from central Spain. These provide some of the earliest evidence for complex animals, making it important to understand in detail the types of burrowing activities involved. Although the traces differ in texture from the enclosing rock they are generally difficult to study because of lack of prominent bedding planes as well as the presence of a mild cleavage. Tomography studies would therefore greatly help in the reconstruction of the three-dimensional morphology of these early burrows. Especially with respect to the study of trace fossils sample size is of importance. The substantial dimensions of the slices that can be studied with the proposed beam-line upgrade is therefore essential to the type of studies I am interested in conducting.

It is my conviction that the proposed upgrade would generate wide interest and usage of the ALBA fascilities by palaeontologists based in Spanish and in other countries.

Yours sincerely,

Sören Jensen Ph.D.
Profesor Contratado Doctor (Associate Professor)
Área de Paleontología
Facultad de Ciencias
Universidad de Extremadura
06006 Badajoz.
Spain
soren@unex.es

VNiVERSiDAD
D SALAMANCA
DEPARTAMENTO DE GEOLOGÍA
Facultad de Ciencias

Salamanca, 26th-September-2014

To whom it may concern.

This letter is to express our interest and support for the initiative to construct a High-energy imaging beamline at the Spanish Synchrotron ALBA in Cerdanyola del Vallès.

The access to such a versatile and powerful technique in Spain will be beneficial to both academic and industrial researchers alike, and will be particularly interesting for the study of subvolcanic processes. A high-energy tomography beamline in Spain is of significant interest nowadays to the geosciences community in general, and particularly to modern petrologists and volcanologists, for advancing in great detail on a.o. (i) the knowledge of volatiles and bubbles evolution from source to surface; (ii) quantifying and assessing different gases behaviours at depth; (iii) a better understanding of kinetics and equilibrium assemblages in anatectic rocks and melts.

We consider that access to this beamline will be very useful for the scientific activities carried out in our Petrology-Volcanology group of the Department of Geology, and is eagerly awaited by some of us who are already using this technique for our research.

Dr. Antonio M. Álvarez Valero
Departamento de Geología
Universidad de Salamanca
Facultad de Ciencias, Plaza de la Merced
37008 Salamanca, Spain
+34 923294498
aav@usal.es